SPATIAL COHERENCE IN A SHALLOW WATER WAVEGUIDE

A Dissertation
Presented to
The Academic Faculty

by

Jie Yang

In Partial Fulfillment
of the Requirements for the Degree
Doctoral of Philosophy in the
George W. Woodruff School of Mechanical Engineering

Georgia Institute of Technology
May 2007

SPATIAL COHERENCE IN A SHALLOW WATER WAVEGUIDE

Approved by:

Dr. Ji-Xun Zhou, Co-advisor
School of Mechanical Engineering
Georgia Institute of Technology

Dr. Emanuele Di Lorenzo
School of Earth and Atmospheric Sciences
Georgia Institute of Technology

Dr. Peter H. Rogers, Co-advisor
School of Mechanical Engineering
Georgia Institute of Technology

Dr. Mark A. Richards
School of Electrical and Computer Engineering
Georgia Institute of Technology

Dr. Jianmin Qu
School of Mechanical Engineering
Georgia Institute of Technology

Dr. Peter H. Dahl
Applied Physics Laboratory
University of Washington, Seattle

Date Approved: February 12, 2007

To my parents and my husband

for their love and support

ACKNOWLEDGEMENTS

Throughout this thesis work, I have received help and support from many people. It is a great opportunity for me to express my gratitude to all of them.

First of all, I want to give my sincere thanks to my advisors, Dr. Ji-Xun Zhou and Dr. Peter H. Rogers, for their guidance, support, and encouragement in the past years. They have set perfect examples for me of what takes to be great scientists with their scientific attitude, curiosity, creativity and dedication. They have also given me invaluable advice on my teaching and presenting skills from which I will benefit through my career.

I would like to thank all my thesis committee members: Dr. Jianmin Qu, Dr. Emanuele Di Lorenzo, Dr. Mark A. Richards, and Dr. Peter H. Dahl for their time to serve on my committee and moreover, their valuable inputs to this thesis. Dr. James F. Lynch (WHOI) has provided insightful suggestions on our collaborative internal wave paper in 2004 which is a key part of this dissertation. Dr. F. Levent Degertekin also gave me valuable information on ultrasonic transducer performance which is vital to the tank experiment.

I would like to express my special thanks to Jim Martin and Dr. Francois Guillot who have provided consistent help especially with my experiments for so many years. Their knowledge, suggestions, and engineering skills have not only improved my research but helped me to be a better experimentalist. I am also in debt to Dave Trivett, Dave Gifford, Michael Gray, Jayme Caspall, John Doane, and Gregg Larson for their kind help with my experimental work and facilities.

I would also like to thank my friends in our acoustic group: Laurent Brouqueyre, Charlotte Kotas, Anne-Marie Albanese Lerner, Lin Wan, and Etienne Dufour for their help over the years. Most of them are still working on their way to a Ph.D and I wish them the best of luck. I also thank for the company and support from my friends: Zhiyuan Zhan, Weiyun Huang, Guangfan Zhang, Yingchuan Zhang, Ning Chen, Ke Wang, Yuhua Ding, Jingshu Wu and Dan Wan.

Finally and most importantly, I want to express my deepest gratitude to my family. I want to thank my parents and my elder sister for their unconditional love and support for so many years. Their encouragement and faith in me have accompanied me all the way to the completion of this work. I want to give special thanks to my husband, Zhiliang Fan, for his love, support, encouragement, optimism, and patience.

TABLE OF CONTENTS

LIST OF TABLES

LIST OF FIGURES

LIST OF SYMBOLS AND ABBREVIATIONS

ASIAEX	Asian Seas International Experiment
ECS	East China Sea
IW	Internal Waves
HF	High Frequency
LF	Low Frequency
SNR	Signal-to-Noise-Ratio
TL	Transmission Loss
RMS	Root-Mean-Square
LPF	Low-Pass Filter
LSE	Least
M2	Semidiurnal tides
RAM	Range-dependent Acoustic Model
PE	Parabolic Equation
SSP	Sound Speed Profile
CTD	Conductivity-Tempertaure-Depth
GM spectrum	Garret-Munk spectrum
BV frequency	Brunt-Vaisälä or buoyancy frequency
PM spectrum	Pierson-Moskowitz spectrum
JONSWAP	Joint North Sea Wave Project
LFM	Linear Frequency Modulated

SUMMARY

In shallow water environments, sound propagation experiences multiple interactions with the surface/bottom interfaces, with hydrodynamic disturbances such as internal waves, and with tides and fronts. It is thus very difficult to make satisfactory predictions of sound propagation in shallow water. Given that many of the ocean characteristics can be modeled as stochastic processes, the statistical measure, spatial coherence, is consequently an important quantity. Spatial coherence provides valuable information for array performance predictions. However, for the case of long-range, low frequency propagation, studies of spatial coherence influenced by various environmental parameters are limited insofar as having the appropriate environmental data with which to model and interpret the results.

The comprehensive Asian Seas International Experiment 2001 (ASIAEX01) examined acoustic propagation and scattering in shallow water. Environmental oceanographic data were taken simultaneously with the acoustic data. ASIAEX01 provided a unique data set which enabled separate study of the characteristics of the oceanographic features and their influence on long range sound propagation. In this thesis, the environmental descriptors considered include sediment sound speed and attenuation, background internal waves, episodic non-linear internal waves, and air-sea interface conditions. Using this environmental data, the acoustic data are analyzed to show the characteristics of spatial coherence in a shallow water waveguide. It is shown that spatial coherence can be used as an inversion parameter to extract geoacoustic information for the seabed. Environmental phenomena including internal waves and

wind-generated surface waves are also studied. The spatial and temporal variations in the sound field induced by them are presented. In addition, a tank experiment is presented which simulates propagation in a shallow water waveguide over a short range. Based on the data model comparison results, the model proposed here is effective in addressing the major environmental effects on sound propagation in shallow water.

CHAPTER 1

INTRODUCTION

1.1 Complexity of a Shallow Water Waveguide

Shallow water acoustics, a challenging branch of underwater acoustics, is "an interdisciplinary blend of physics, signal processing, physical oceanography, marine geophysics, and even marine biology" (Kuperman and Lynch, 2004). The ocean is usually described as horizontally stratified, which allows us to model it as a waveguide bounded by the ocean surface and bottom.

Shallow water environments are typically found in the continental shelf region. The continental shelf is the zone adjacent to a continent. It is quite flat over several tens of kilometers with water depth less than 200m. It is connected to the deep ocean by the shelf break which has a sharp increase in slope (Katsnelson et al., 2001). The shelf region is crucial to human activities such as shipping, fishing, oil well drilling, underwater communication etc. Sound propagation in this region experiences interactions with the lossy bottom, hydrodynamic disturbances such as currents, internal waves and fronts, and rough surfaces. It has to compete with various noise sources due to human activities, marine mammals and other marine organisms, wind, and precipitation. It is thus very difficult to make satisfactory predictions of sound propagation in shallow water.

Many ocean characteristics such as wind-generated surface waves, subbottom inhomogeneities, and internal gravity waves can be modeled as random processes. All are not well measured and understood. They can cause spatial and temporal fluctuations in

temperature and salinity which, in turn, will change the sound speed distribution. Although the variations are typically less than one percent, they may induce significant changes in the sound field. Therefore it's meaningful to study the statistical properties of the waveguide which include randomness from both the interfaces and volume.

As a statistical measure, spatial coherence, which is the joint second moment of the acoustic field, is a useful quantity for studying the characteristics of sound propagation in a shallow water waveguide (Smith, 1976). As will be seen later from the definition of the cross-correlation function, the information about the waveguide is preserved in the received waveforms and hence in the cross-correlation function. Therefore, the cross-correlation function can be used as an inversion technique to determine environmental properties (Yang et al., 2004[1]) or to study the influence of the waveguide on sound propagation as well.

Moreover, measurement of the spatial correlation is a useful tool for predicting performance of large acoustic arrays. The array gain (AG), a widely used array performance indicator, can be measured using the array and element signal-to-noise ratios. It can also be represented in terms of the spatial coherence of signal and noise between any two elements of the array (Urick 1967).

1.1.1 Sediments

In shallow water, seabed plays an essential role in sound propagation. From Snell's law $\cos\theta/c(z) = const$ where θ is the ray angle with respect to the horizontal and $c(z)$ is the local sound speed. Snell's law implies that sound rays will always bend towards lower sound speed. For the summer shallow water case, the rays will bend towards the bottom before reflecting. Rays with bigger angle of incidence have higher

losses at each interaction and also bounce between the boundaries which results in greater attenuation per distance traveled.

Many sediment properties are regarded as being of importance to wave propagation in shallow water: bottom type, thickness of the bottom and subbottom layers, compressional and shear wave velocities and their corresponding attenuations (as functions of depth), sediment porosity, grain size distribution, and permeability. Among these, compressional wave velocity and attenuation are the most important factors (Stoll et al, 1994).

There are three existing sediment models: (1) Hamilton (1980); (2) Biot-Stoll (Biot, 1956[1,2], 1962; Stoll, 1985); (3) BYT (Yamamoto and Turgut, 1988). All agree that sediment compressional wave speed has a positive gradient in depth and can be written in the form $C_b(z) = K * z^{0.015}$ (Hamilton, 1980), where K is a constant and z is the depth into the sediment.

Sediment intrinsic attenuation is very difficult to measure at sea because the measured value may be the result of a combination of several mechanisms (Hamilton, 1976). It can be the intrinsic attenuation through materials, losses by multiple reflections, or scattering by inhomogeneities. This attenuation is usually referred to as "effective attenuation".

Concerning "effective" compressional wave attenuation, the Hamilton model differs from the other two as to whether attenuation has linear frequency dependence. The Hamilton model proposed an empirical relation based on geoacoustic data at various locations: $\alpha = \kappa f^n$. Here α is attenuation in dB/m, κ is attenuation coefficient in dB/m-kHz, and f is frequency in kHz. The controversy lies in whether the attenuation has a

linear frequency dependence, i.e., $n = 1$. Hamilton (1980) concluded that this dependence is approximately first-power in silt clays (mud) from a few Hz to 1 MHz.

Based on the porous nature of the sediments, Biot and Stoll (Biot, 1956[1,2] & 1962; Stoll, 1979 & 1985) theorize that relative motion of the pore fluid and the sediment frame should lead to viscous damping of the sound wave. Their model predicts a nonlinear frequency dependence of sound attenuation in water-saturated rocks, sands, and silts.

As supporting evidence of the Biot-Stoll model, Ingenito (1973) found the frequency/attenuation dependence to be: $\alpha = 0.498 f^{1.75}$ while Zhou (1985) obtained $\alpha = 0.37 f^{1.84}$. Nowadays, more data fall in the category of nonlinear frequency dependence. In Figure 1.1, Zhou *et al.* (2005) shows frequency dependence of attenuation from 16 different locations around the world in the frequency range 50 Hz to 2 kHz. The attenuations in Figure 1.1 are inversion results from various acoustic data and methods. With first- and second-power dependence plotted on the figure, it is quite obvious that the dependence is close to the second-power.

1.1.2 Internal Waves

In the last two decades, many researchers have begun to study the fluctuations of the water column and its influence on sound propagation. The original work of Zhou and his coworkers (1991) showed that internal solitary waves could be responsible for the anomalous frequency response of shallow water sound propagation observed in the Yellow Sea in the summer. Internal waves are usually generated by tidal movement over topography, such as a shelf break, and they can be long-period linear IWs or intermittent high frequency wave packets called solitary waves. As Zhou et al (1991) found out, the transmission loss becomes strongly time dependent, anisotropic and sometimes exhibits

an abnormally large attenuation over some frequency range due to resonant coupling between sound and solitary internal waves. It has also been observed that internal waves can cause variations in signal travel time, pulse spreading, and changes in field coherence (Traykovski, 1996; Duda et al., 1999; Headrick and Lynch, 2000). These effects not only depend on the strength of the internal waves but also their propagation direction (Katsnelson et al., 2001).

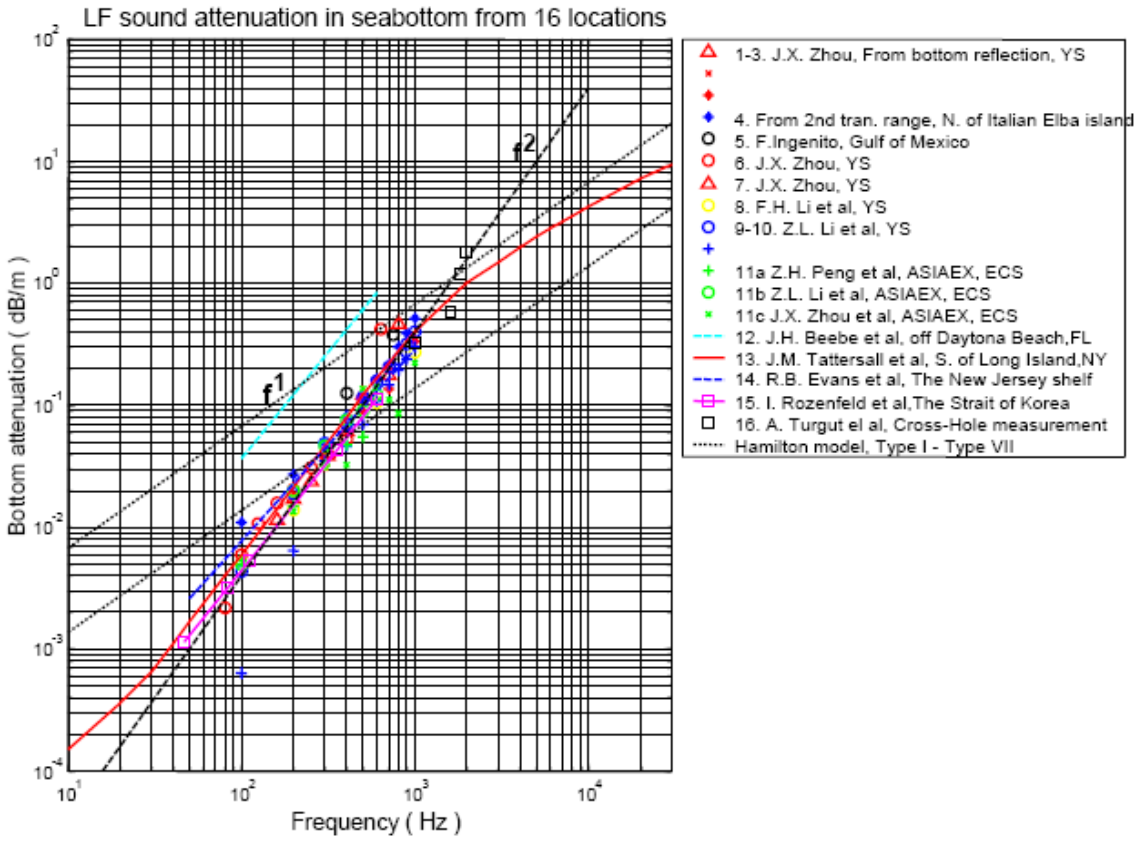

Figure 1.1 Frequency dependence of sediment effective attenuation (Zhou *et al.*, 2005).

Studies (Lynch et al., 1996; Tang et al, 1997; T. Yang et al., 1999; and Flatté et al, 2000) applied a modified deep-water Garret-Munk internal wave spectrum (Garret and Munk, 1972, 1975) in shallow water. The GM spectrum is wideband and usually found

from the temperature time series. It can be used to generate the sound speed fluctuations due to the movement of the internal waves as a random process. This sound speed fluctuation distribution, in terms of space and time, is added to the mean sound speed field. In general, the semidiurnal tidal frequency (M_2) dominates the spectrum, even though the high frequency nonlinear wave trains like the solitons are locally very energetic. Therefore, this can be regarded as a "weak" scattering process. Tielbürger et al (1997) and Finette et al (2000) have built a model that separate the long-period background internal waves from the episodic solitons. The background internal wave spectrum is from the time period without evident solitary wave activities. The sound speed field now contains three components: mean field, fluctuation due to the background internal waves, and the solitons. The sound speed field is used as input to a range-dependent acoustic model and the results compared with experimental data. A detailed description of how the modeling is accomplished can be found in session 6.3.1.

1.1.3 Wind-Generated Surface Gravity Waves

Another important factor in sound propagation is the process at the air-sea interface such as wind-generated surface gravity waves. Studies investigating the interactions of sound waves and uneven sea surfaces have been carried out since the early 50's. Modeling incorporates the surface effects as a scattering process. Two theoretical methods have been proposed: the perturbation method (Rayleigh 1945) and the Kirchhoff approximation (Eckart, 1953) for low and high frequency respectively. Neither model gives an adequate account of the scattered sound field since the ocean surface roughness has a wide range of scales. Therefore, composite roughness scattering models have been proposed by many researchers (Kur'yanov, 1963; Bachmann, 1973; Galybin, 1976;

McDaniel et al, 1982). The surface model now has two components: one is low frequency surface gravity waves and the other is capillary waves in the high frequency range. (Detailed discussion on surface models can be found in session 7.3.1.)

For long-range sound propagation, the interaction between sound and the surface waves induces an extra attenuation in the sound field (Kuperman et al, 1977; Weston et al, 1989). In shallow water, this attenuation may depend on other properties of the waveguide as well, such as the seabed properties, sound speed profile, etc. Recent literature proposed numerical approaches to include surface waves as a range dependent acoustic model (Dozier, 1984; Collins, 1993; Norton et al, 1995 & 1996; Rosenberg, 1999). As an input to the model, the surface waveheight distribution, over a certain range, is computed by the surface wave spectrum (Thorsos, 1990; Funk et al, 1992; Rouseff et al, 1995; Dahl, 2004[2]). Specifically, the surface wave spectrum is converted to waveheight variations using inverse spatial Fourier transform. In Chapter 7, the procedure of including the surface waves will be addressed.

1.2 Definition of Spatial Coherence in Shallow Water Acoustics

Spatial coherence is defined as the cross-correlation function between two hydrophones at two arbitrary locations:

$$\Gamma(z_s, z, d_L, d_V, r; \tau) = \frac{< P(z_s, z, r; t) P^*(z_s, z + d_V, r + d_L; t + \tau) >}{\sqrt{< P(z_s, z, r; t)^2 >< P(z_s, z + d_V, r + d_L; t)^2 >}} \qquad (1.1)$$

In this equation, P is the acoustic pressure at one hydrophone at time t, z_s is the source depth, z and r are the depth and range of one receiver, <·> indicates ensemble average, and d_v and d_L are vertical and horizontal separation between the two receivers. The acoustic signals at two hydrophones are usually pressure time series. Therefore, the

denominators of eq. (1.1) are the time averaged root-mean-square pressures while τ in the numerator indicates the time lag between the two time series. By setting $d_v = 0$ or $d_L = 0$, horizontal and vertical coherence can be easily separated. Furthermore, by setting both of them equal to zero, the result is simply proportional to the averaged sound intensity at that point. Expressed in decibels, it is the statistical estimate of transmission loss (Smith, 1976). Note, the ensemble average of a random process is defined as $\langle x \rangle = \int_{-\infty}^{\infty} x p_x dx$, where x is the random variable, p_x is its probability density function and $<x>$ is the resultant mean value of x.

In this thesis, spatial coherence will need to be quantified for both experimental and theoretical. In general, the experimental coherence is calculated as the zero-delay cross-correlation coefficient between two hydrophones (Urick, 1970). The cross-correlation function is defined as:

$$R_{xy}(\tau) = \left\langle x(t)\, y^*(t-\tau) \right\rangle \tag{1.2}$$

where, R_{xy} stands for the cross-correlation function, τ is time delay. t, x and y are time series received at the two hydrophones. The coherence results used in later chapters is by setting τ = 0 in eq.(1.2) (Urick, 1970). The calculation of experimental coherence doesn't involve direct ensemble averages except for the case when there were multiple signals at the same location. The ensemble averaging of (1.2) comes from frequency averaging (1/3 octave band filtering), depth averaging (averaging of adjacent channels), range averaging, and numerous interactions with the medium (Smith, 1976). In the model, eq. (1.1) is followed and τ is set to zero. For predictions of stochastic process such as internal waves, the acoustic pressure in eq. (1.1) is calculated a certain number of times using realizations

of environmental parameters induced by the internal waves. An average is taken over all the realizations.

1.3 Objectives

In this dissertation, the objective is to systematically study the acoustical effects of environmental parameters on spatial coherence in a shallow water waveguide. Specifically we mean that range, R, divided by depth, D, is such that R/D >> 1, and D/λ (λ is acoustic wavelength) is not too large, such that a modal description is more appropriate than one involving rays. Specifically, this thesis will focus on:

- Analyzing the characteristics of vertical coherence using *in situ* wideband SUS charge signals;
- Studying the characteristics of environmental phenomena including the internal waves and the wind-generated surface waves in a shallow ocean;
- Investigating the acoustical effects from the environmental factors, including seabed, internal waves and sea surface waves, on vertical coherence via range dependent acoustic models as a propagation and inversion methods;
- Studying sound propagation in a simulated Pekeris waveguide in a water tank and use the interference pattern as an inversion parameter.

The completion of this thesis work will help understand the environmental effects on vertical coherence of long range sound propagation, especially under the influence of internal waves and surface waves.

1.4 Thesis Outline

This thesis is organized as follows:

In Chapter 2, a detailed description of at sea and tank experiments will be given.

In Chapter 3, we will introduce two propagation theories: normal modes and the parabolic equation method. Both will be used in this research.

In Chapter 4, we will analyze acoustic data taken from the at-sea experiment and explore the characteristics of spatial coherence in a shallow ocean.

In Chapter 5 to 7, we will show the data/model comparison due to the three important environmental parameters: sea bottom, water column, and surface gravity waves.

In Chapter 8, results from a tank experiment will be shown and compared with model results.

In Chapter 9, we will present a summary of this thesis work and suggest future work.

CHAPTER 2

EXPERIMENTS: ASIAEX'01 AND MODEL EXPERIMENT

2.1 In Situ Experiment in the East China Sea: ASIAEX'01

2.1.1 ASIAEX'01

The Asian Seas International Acoustics EXperiment (ASIAEX) was a multinational scientific project conducted in the East China Sea (ECS) and South China Sea (SCS). There are 19 institutions involved in the experiment including Georgia Institute of Technology ME acoustics group. The ECS part of the ASIAEX, which will be concentrated on here, was conducted from May 27 to June 9, 2001. One of the main goals of the ASIAEX ECS component was to contribute to a better understanding of acoustic propagation and scattering (reverberation) in shallow water. It involved acoustical, oceanographic and geological field measurements.

Figure 2.1 is the ASIAEX site locator map and the rectangle indicates the experimental site. More detailed information can be found in Figure 2.2 with a GPS mapping of the experimental site and bathymetry coutours. The blue dots indicate the positions of the wideband explosive sources (TNT 38g) deployed during the experiment. The receiving ship was at the center of the circle M throughout the experiment while the transmitting ship followed M-E, E-E circular, and F-H paths (red lines). The circular region is on the shelf break with a radius of 30 km and the depth variation over 60 km (between F and G) is about 22 meters. Bathymetry data taken over 130 km range is

shown in Figure 2.3. Note that most of the measurements were taken on the continental shelf, the shallow region.

Acoustic signals were recorded using a 32-element vertical hydrophone array suspended from the receiving ship at point M by Institute of Acustics, the Chinese Academy of Sciences. Figure 2.4 shows a sketch of the array configuration. In addition, Figure 2.4 also contains depth information for a 17-element thermistor array deployed by Georgia Tech. The thermistors sampled temperature every 30 seconds over 63 hours.

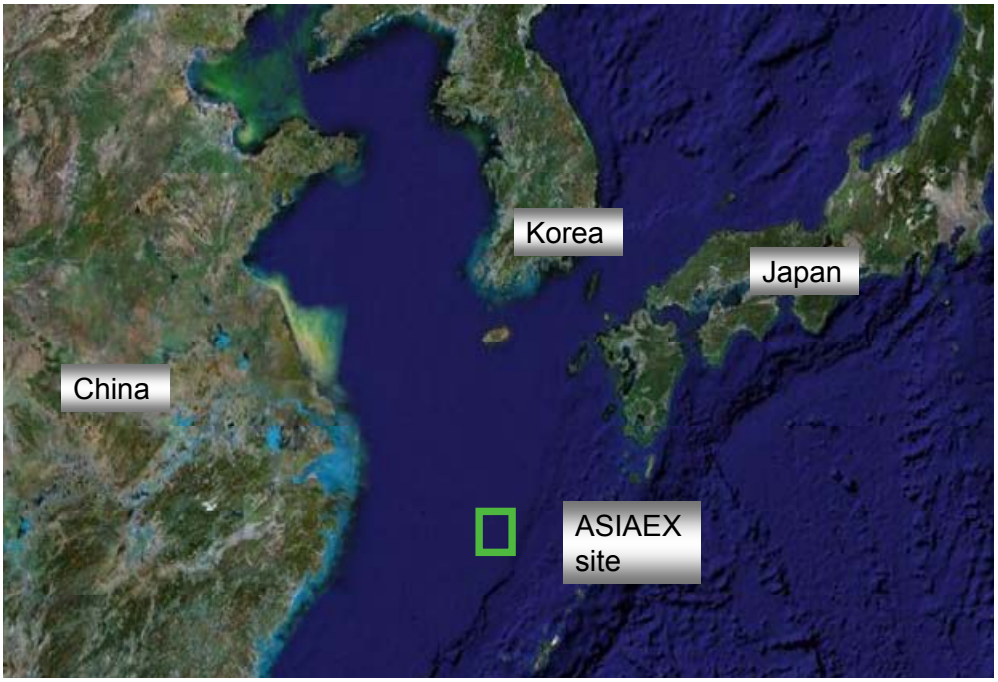

Figure 2.1 Satellite picture of the *in situ* experimental site.

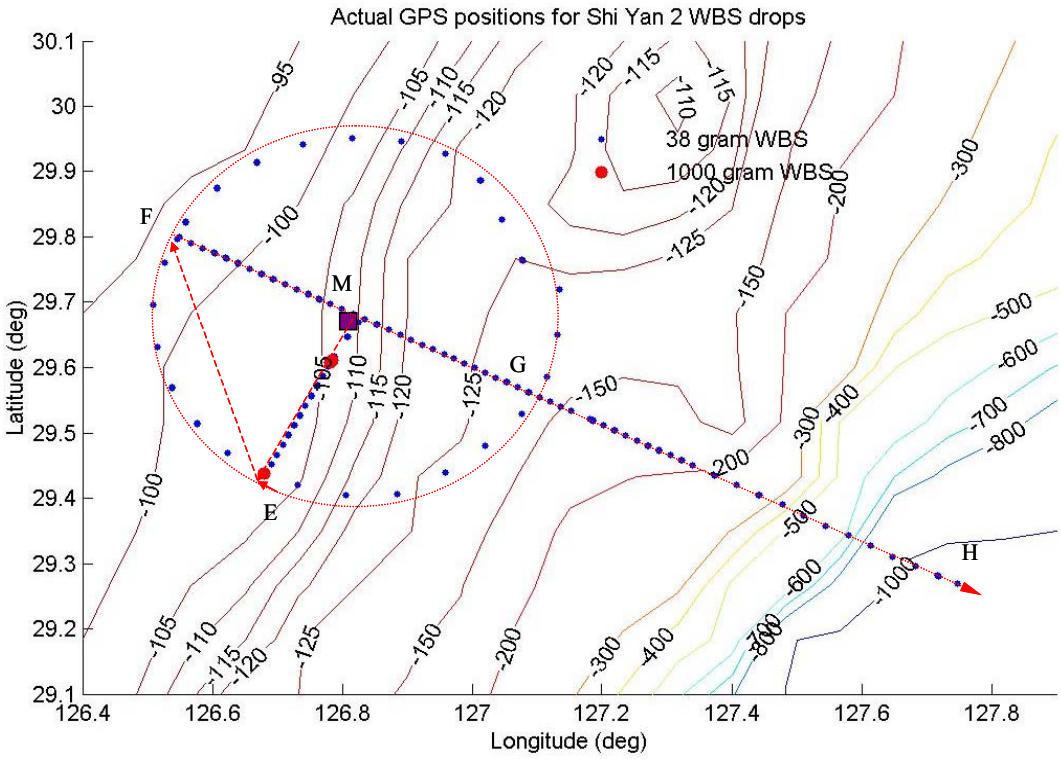

Figure 2.2 GPS mapping of the experimental site with bathymetry contours. Blue dots are positions of wideband signals deployed.

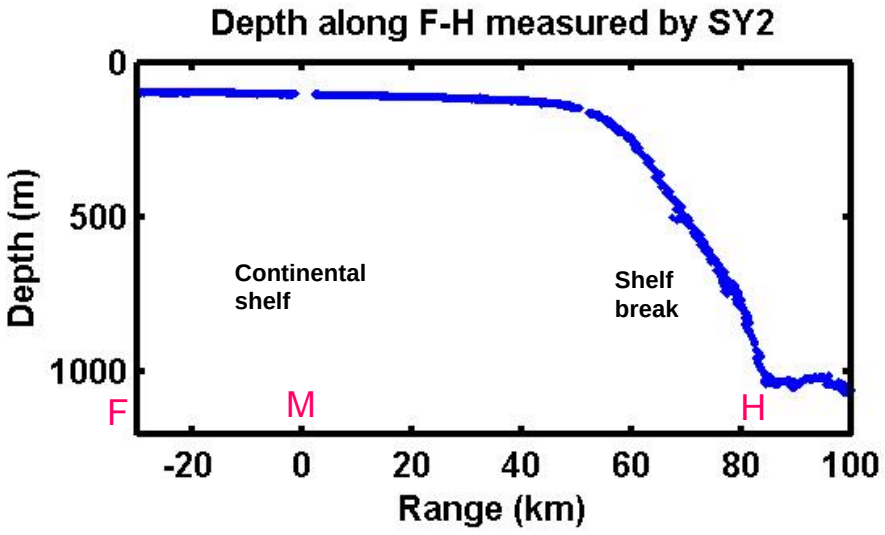

Figure 2.3 Bathymetry plot along F to H.

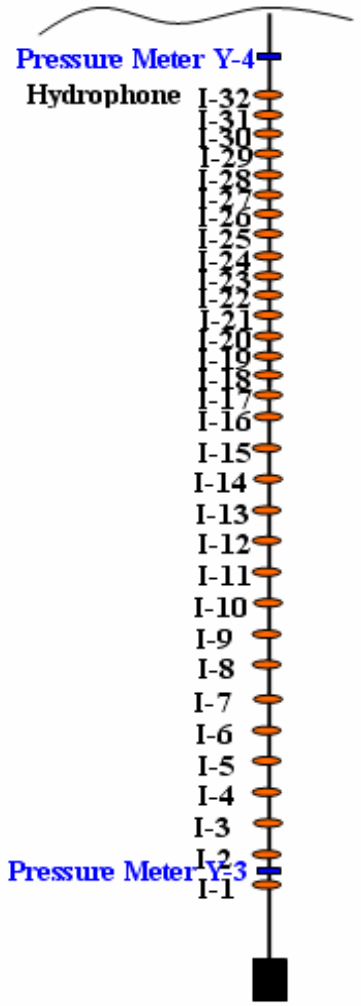

Hydrophone Number	Space (m)	Actual Depth* (m)	Thermistor depth (m)
Y-4	□	4.5± 0.4	19.95
I-32	0.3	4.6	23.10
I-31	1.73	6.3	26.25
I-30	1.80	8.1	29.40
I-29	2.08	10.2	32.55
I-28	1.48	11.7	35.70
I-27	1.66	13.4	38.85
I-26	1.67	15.0	42.00
I-25	1.79	16.8	45.15
I-24	1.80	18.6	48.30
I-23	1.77	20.4	51.45
I-22	1.58	22.0	54.60
I-21	1.72	23.7	57.75
I-20	1.68	25.4	60.90
I-19	1.70	27.1	65.10
I-18	1.69	28.8	71.40
I-17	1.75	30.5	79.80
I-16	2	32.5	
I-15	4.0	36.5	
I-14	4.00	40.5	
I-13	4.00	44.5	
I-12	4.00	48.5	
I-11**	1.25	52.5	
I-10	4.00	56.5	
I-9	4.00	60.5	
I-8	4.00	64.5	
I-7	4.00	68.5	
I-6	4.00	72.5	
I-5	4.00	76.5	
I-4	4.00	80.5	
I-3	2.00	82.5	
I-2	4.00	86.5	
Y-3	3.10	89.6	
I-1	0.90	90.5	

Figure 2.4 Depth information for the vertical hydrophone and thermistor arrays.

2.1.2 Oceanographic and Geoacoustic Information of the ECS

ASIAEX's primary goal was to study the influence of shallow water boundaries including effects of roughness and inhomogeneities on sound propagation and also to establish a geoacoustic description of the ECS seabed (Dahl et al., 2004[1]).

Surface roughness was characterized from the measurements of the RMS surface wave height and wind speed recorded between May 29 and June 7, 2001 close to the mooring location M (detailed description can be found in Chapter 7). In Figure 2.5, the

top figure is the time series for RMS surface wave height; while the bottom figure shows the time history of wind speed. Comparison of the two curves indicates high correlation between wind speed and wave height. The increase in the RMS waveheight is directly related to the increase in wind speed but with several hours delay. Surface wave spectra were also measured using a directional wave buoy (Dahl, 2004[2]) which will be discussed in detail in Chapter 7.

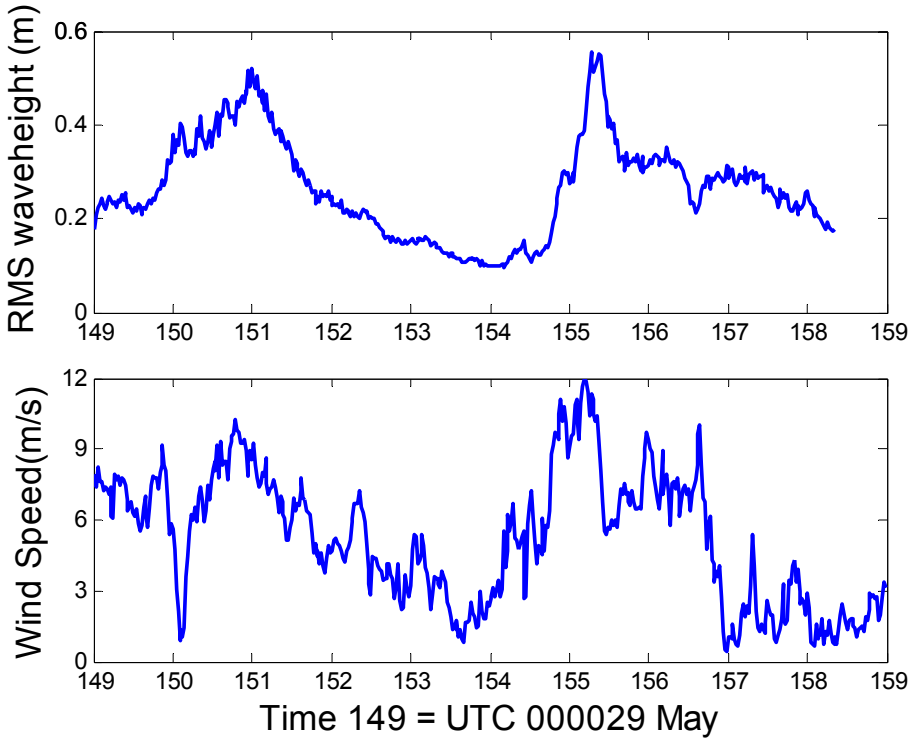

Figure 2.5 RMS waveheight and wind speed record from May 29th to June 6th, 2001.

The Georgia Tech 17-element thermistor chain provided high quality data for studying the characteristics of the internal waves in the ECS (J. Yang et al., 2004). Temperature data from the 17-element thermistor chain exhibited clear internal wave features. Large amplitude oscillations, up to 35m peak-to-peak, are noted due to the semi-

diurnal internal tides with period 12.42 hours (see Figure 2.6). The temperature time series are also plotted for each thermistor labeled by their depths on the left in Figure 2.7. High frequency oscillations are readily seen, occurring at almost the same time each day. Many other researchers (Cairns '67; Halpern '71; Rubenstein '99) have also reported this phenomenon. This high frequency motion which lasts about 2-3 hours every day is clearly a response to tidal forcing. The strongest period of activity is around 15:40-18:40, June 3rd. Temperature data in this period is enlarged in Figure 2.8 to give a better view of the narrow bandwidth internal wave trains around 6 cph riding on top of the semi-diurnal internal waves. The internal tides and the high frequency oscillations are corresponding to the linear and non-linear internal waves which will be investigated in Chapter 6.

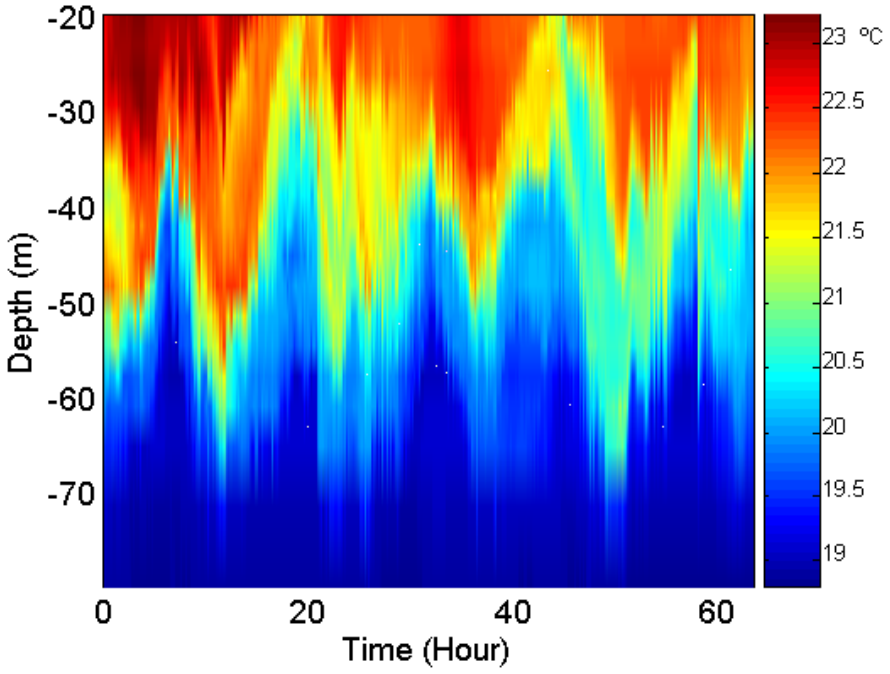

Figure 2.6 63-hour temperature color plot from 08:40, June 3rd to 00:00, June 6th. The location is 126°54.32'E and 29°24.01'N.

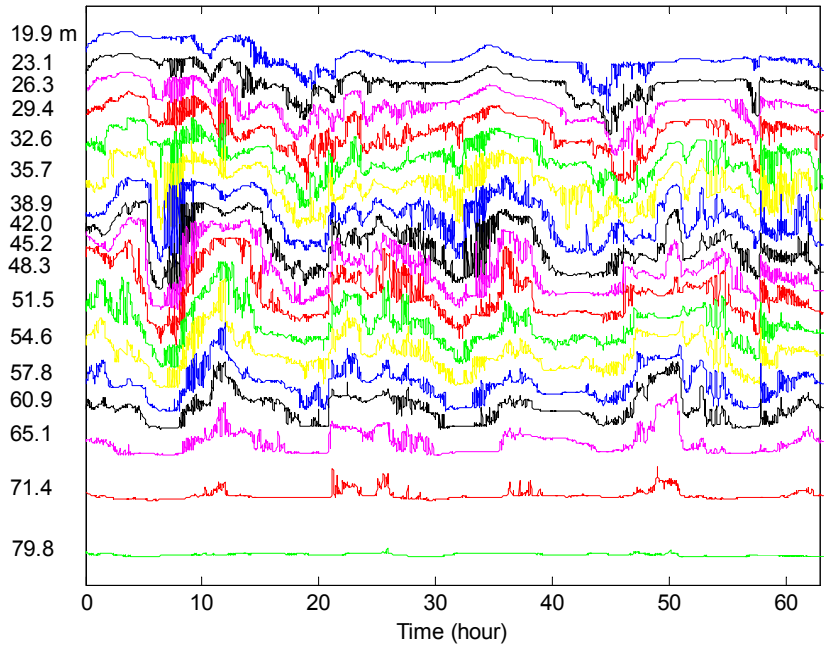

Figure 2.7 63-hour temperature time series from 08:40, June 3rd to 00:00, June 6th.

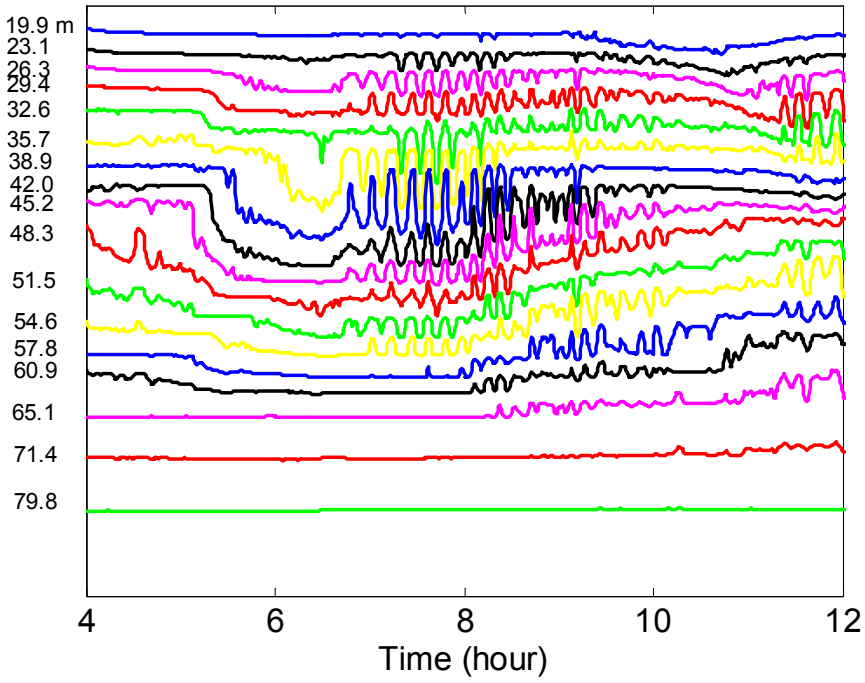

Figure 2.8 8-hour enlarged temperature plot during the period of the strongest high frequency IW oscillations from 12:40 to 22:40, June 3rd.

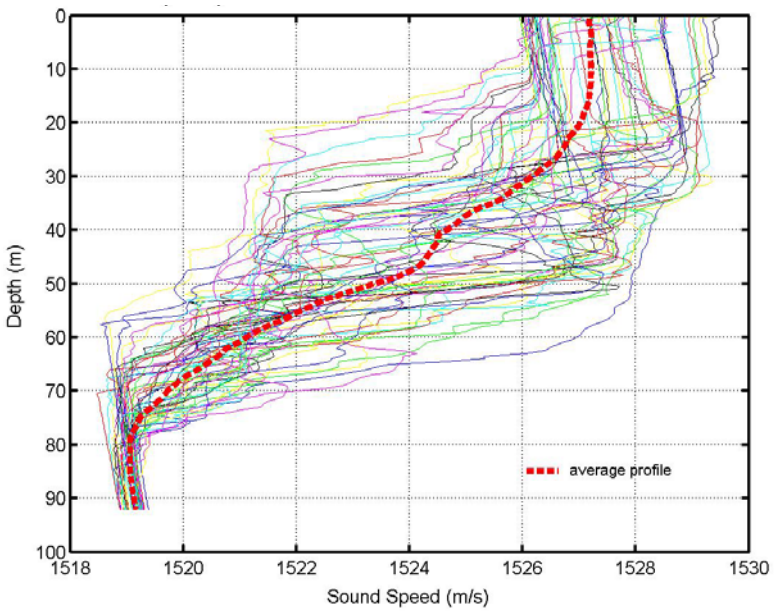

Figure 2.9 54 CTD derived sound speed profiles recorded in the ECS.
The doted line in red is the average profile. Water depth: 104m.

In addition to the thermistor data, a collection of 54 intermittent CTD profiles were recorded as well (Figure 2.9). A CTD is an instrument that measures Conductivity-Temperature-Depth from which sound speed can be calculated. The speed of sound in water, as a function of temperature, salinity, and depth, can be written as (Jensen et al, 2000):

$$c(z) = 1449.2 + 4.6T - 0.055T^2 + 0.00029T^3 + (1.34 - 0.01T)(S - 35) + 0.016z \quad (2.1)$$

Properties of the seabed at the ECS site were extensively studied using several techniques including gravity and piston cores, subbottom profiling using a water gun, long range sediment tomography, and *in situ* measurements of conductivity. The information we are interested in is the sediment sound speed and attenuation which mainly depend on the bottom type and grain size. The compressional sound speed distribution over the 30 km circular region is shown in Figure 2.10. Sound speed of the

sediment changes from 1600 m/s from the west (point F) to 1660 m/s to the east (point G) due to coarser sediments. These variations in sediment type, grain size, and sound speed may result in anisotropic sound propagation.

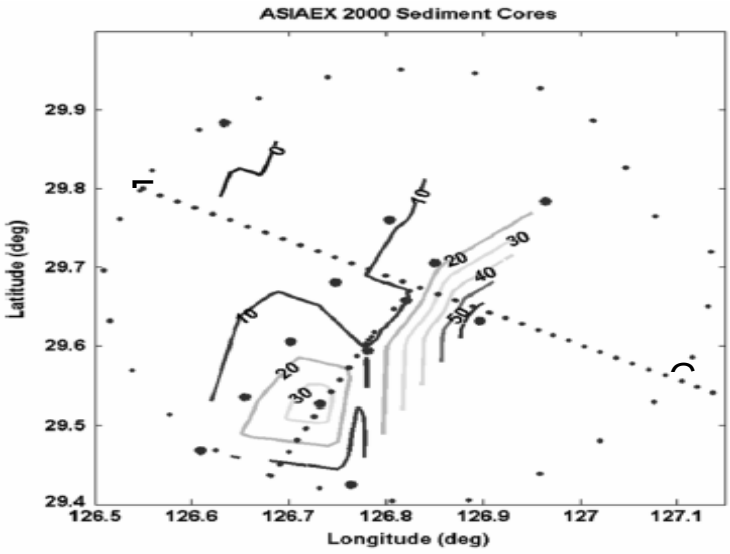

Figure 2.10 Sediment compressional sound speed distributions compared with 1600 m/s.

2.2 Model Experiment

2.2.1 Introduction

2.2.1.1 Motivation and Previous Work

Model experiments can supplement to at-sea experiments and provide an important way to verify acoustic propagation and scattering models. Such experiments offer:

1) low cost
2) better understanding of the physical mechanisms
3) well-controlled experimental environments(decoupling the parameters)

4) possibility of improving acoustic modeling

Previous work using model experiments dates back to the sixties (Clay, 1964). The focus of the research, including later work in the seventies (Ferris, 1972; Ingenito, 1973; Gazanhes et al., 1978[1]; Tindle et al., 1978; Gazanhes et al., 1981) was on validating conclusions of the wave theory. Wave theory predicts that there is a set of discrete normal modes and each has a different propagating velocity and attenuation coefficient. The modes were separated using a spatial mode filtering method based on the orthogonality property of the modes. (The derivation of the acoustic field in terms of normal modes is given in Chapter 3.)

In general, lower order modes have higher group velocities and smaller attenuation coefficients. Thus, after sufficient propagation distance, lower order modes will dominate and may be separated in time from each other due to the difference in group speeds. The modal attenuation of each propagating mode contains information about sediment properties and hence can be used as the basis of an inversion technique. It is difficult to study mode propagation in situ for several reasons: one, the limitation of number of vertical elements; two, the cost of sampling the acoustic field at different ranges simultaneously; three, the nature of the ocean environment which is changing temporally and spatially.

Here, tank experiments will be used to study mode propagation, invert bottom properties using the modal attenuation coefficient and to study vertical and longitudinal coherence in a deterministic environment.

2.2.1.2 Experimental Considerations to a Pekeris Waveguide Problem

The frequency range of interest for this tank experiment is between 100k ~ 300 kHz. The selection of the frequency range is twofold. Due to a finite-size tank, it is preferred to increase the frequency as high as possible to study a representative propagation problem. On the other hand, the acoustic wavelength decreases with increasing frequency so a tiny change on the propagation path such as unevenness of the surface or micro bubbles, may cause substantial discrepancy in the results. The scaling factor, defined as the ratio between frequencies of tank to those at-sea experiments, is chosen to be 1000, i.e. the selected frequency range will allow us to study propagation range up to 3.5km (tank dimension: 3.5x0.85m). The non-dimensional parameter R/D is 70 and D/λ is in the range of 3 to 6, which indicates a modal propagation problem at a short range.

A simple, two homogeneous layer propagation problem will be studied here, which is referred to as a Pekeris waveguide problem (Pekeris, 1948). A uniform "seabed", a hard neoprene rubber sheet with 0.5in thickness, is chosen for several reasons. It shows relatively close properties to the three key properties of a real sea bottom which are density, sound speed and attenuation. The detailed measurement of rubber properties is presented in Sec. 2.3.

2.2.2 Experimental Setup

The scale experiment is done in a water tank shown in Figure 2.11 which has a size of 3.5x0.85m. A 3-D positioning system, made by VELMEX Inc., is fastened from the top of the tank. The VELMEX VP9000 is a stepping motor controller, capable of running up to four motors (Figure 2.12). A computer program, setting stepsizes and

motor speeds, communicates with the controller through a RS-232 interface. Motor positions, setup parameters, and menus are viewed on the front panel display.

A Panametric immersion ultrasonic transducer is used as the source (Figure 2.13, left) which is 0.5in in diameter and has a resonance frequency of 1 MHz. We have to use a microprobe hydrophone as a receiver considering that the wavelength is on the order of centimeter. The microprobe is manufactured by the Baylor University, School of Medicine and is intended for blood flow velocimetry. The actual element of the probe is 0.8 mm in diameter and has a resonance frequency of 20MHz (Figure 2.13, right).

Figure 2.11 Water tank with a 3-D positioning system.

Figure 2.12 VELMEX VP9000 stepping motor controller.

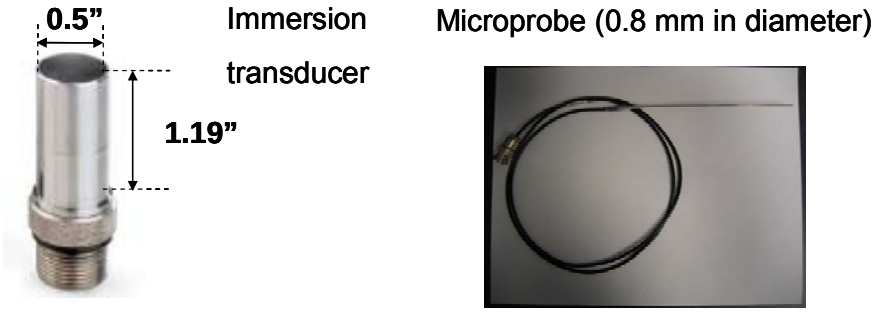

Figure 2.13 The ultrasonic source (left) and microprobe (right) for the tank experiment.

The electronic systems at both transmitting and receiving ends are shown in Figure 2.14. The transmitting system includes three elements: function generator, anti-aliasing filter, and power amplifier while the receiving system consists of preamplifier, digital oscilloscope, and a PC.

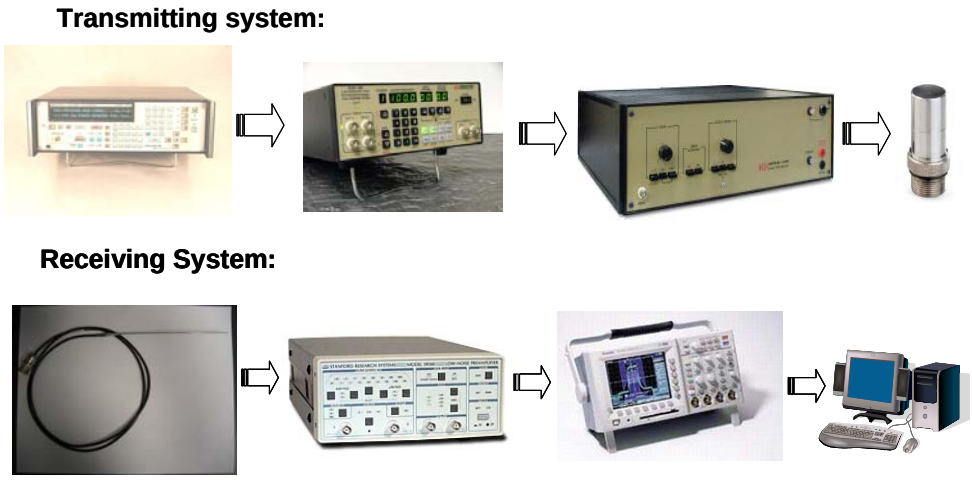

Figure 2.14 Electronic systems for the tank experiment.

Specifically, the function generator is a 6.25 MHz, 12-bit Polynomial Waveform Synthesizer from Analogic-Data Precision, model 2020. Waveform from the function generator goes through the anti-aliasing filter, a Krohn-Hite 3988. KH3988 is a dual channel low-pass/high-pass filter with 8 poles and attenuation slope 48 dB/octave. The power amplifier is a Krohn-Hite Model 7500 with a frequency range from DC to 1 MHz.

In the receiving system, the acoustic signals are detected by the microprobe and band-pass filtered and amplified by the preamplifier. The preamplifier is an SR560 from Stanford Research Systems. The SR560 contains two first-order RC filters. The signals are digitized by the oscilloscope and directly saved to a PC though GPIB interface. The oscilloscope is a Tektronics TDS3054 which has a 9-bit vertical resolution and a sampling rate up to 5 GHz.

2.2.3 Rubber Property Measurements

The key ingredient in the experiment is the “seabed”. We used a hard neoprene rubber sheet, of thickness 0.5in, to cover the bottom of the whole tank. The choice of this rubber was based on published values for sound speed and attenuation (Selfridge, 1985).

These values, however, are not very definite or accurate. It was essential to measure the sound speed and attenuation of the hard neoprene in the frequency band of interest.

2.2.3.1 Measurement of Speed of Sound in Hard Neoprene

The procedure for measuring the rubber properties is as follows. Two ultrasonic transducers are used, one as a source and the other as a receiver. The experimental setup is shown in Figure 2.15. A short pulse is transmitted between the transducers in water. The arrival time of the received signal are recorded for a separation D_1 (Figure 2.15) and then for D_2. The difference in the arrival times corresponds to the time interval for sound to travel a distance of D_1-D_2 at the speed of water of the time. Specifically,

$$c_w = (D_1 - D_2)/(t_1 - t_2) \tag{2.2}$$

After finding the sound speed of the water, the procedure (Figure 2.15) is repeated with 1.207" wide rubber in between the transducers. Again, the arrival times are recorded. The difference between the arrival times with and without rubber corresponding to the difference in sound speeds between rubber and water:

$$\delta t = \frac{rubber\ width}{c_w} - \frac{rubber\ width}{c_{rubber}}$$

$$\Rightarrow \quad c_{rubber} = rubber\ width \Big/ \left(\frac{rubber\ width}{c_w} - \delta t \right) \tag{2.3}$$

Following the procedures mentioned above, the speed of sound in water and rubber are calculated and plotted in Figures 2.16 to 2.17 respectively. The speed of sound in water calculated yields an average value of 1490.5m/s. Figure 2.17 shows the rubber sound speeds measured at D_1 and D_2 and their averaged results as a function of frequency. Both sound speeds show little dependence on frequency.

The error bar showing on the speed of sound measured in water is due to the time resolution of the arrival time which is 0.02μs. This caused an average of 0.97m/s standard deviation in the speed of sound in water and hence, 1.5m/s standard deviation in the speed of sound in rubber.

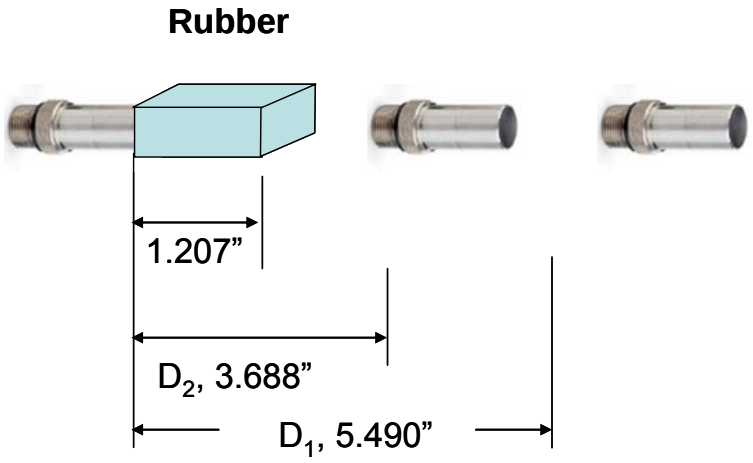

Figure 2.15 Test of sound speed in rubber.

2.2.3.2 Measurement of Attenuation Coefficient in Rubber

For the attenuation in rubber, we will use a similar experimental setup as Figure 2.15 except that data will be recorded at one distance. A pair of ultrasonic transducers is used, both ½in in diameter and have resonance frequency at 1MHz. This pair of sources is placed at distance 13.95cm. To measure acoustic signals, it is usually preferable to stay in the far field since the near field fluctuates a lot. For this circular piston transducer/source, its far field distance, which is also called the Rayleigh distance, can be easily calculated as:

$$R = surface\ area\ of\ the\ source\ element / wavelength = \pi a^2 / \lambda$$

The frequency range that is of interest here is between 100 to 500 kHz. The maximum Rayleigh distance occurs at the highest frequency which is 4.22cm.

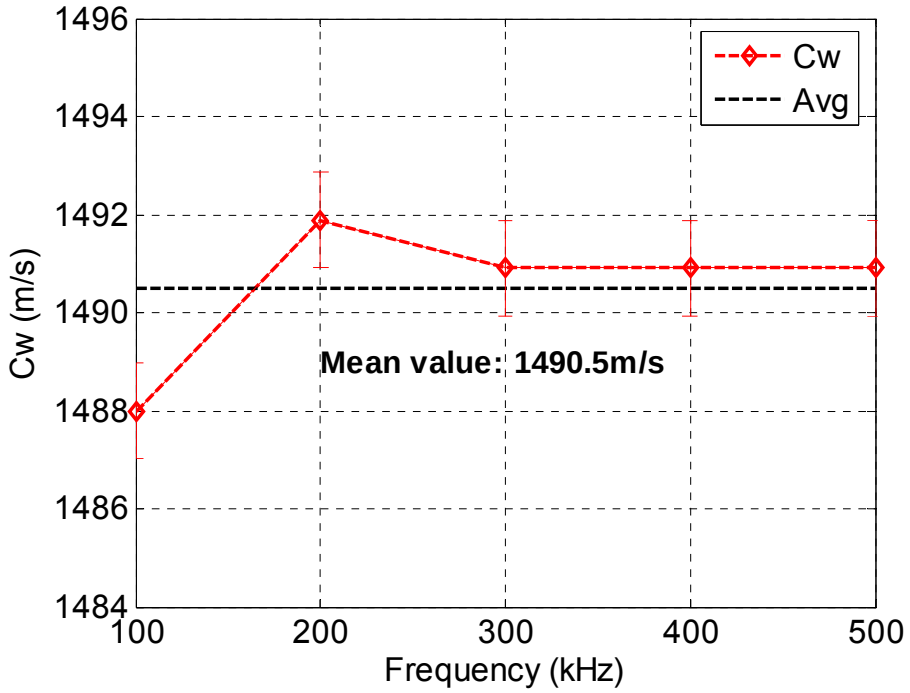

Figure 2.16 Measurements of sound speed in water between 100 and 500 kHz.

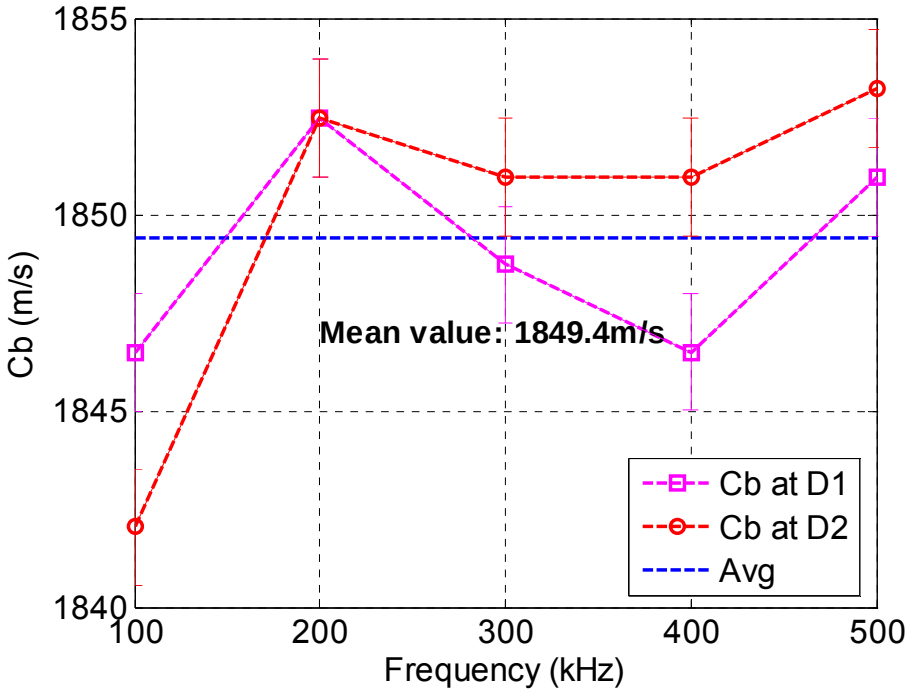

Figure 2.17 Measurements of sound speed in rubber between 100 and 500 kHz.

The procedure is to send out 2ms circular signal which has a wide bandwidth from 50k ~ 800 kHz. A 2ms-long signal is recorded with and without the rubber. Then, pulse compression technique will be used to study the system response at each frequency. The procedure is exactly the same as the data processing for the tank experiment of Appendix B.

The first arrivals, with and without the rubber in between the transducers, are recorded. An example is shown in Figure 2.18. The left of figure 2.18 is the comparison of the first arrivals with and without rubber in between the transducers at 400 kHz. (The direct arrival with rubber (red) was multiplied by 30 in order to be seen on the figure.) A 23μs window is used to gate later arrivals. The spectra of the two first arrivals are shown on the right of Figure 2.18. The rubber attenuation is found by the difference of the two spectrums in a frequency range. This frequency range is specified as 3dB down from the spectrum peak for the rubber. The process is repeated by sending out 100 Gaussian pulses at different center frequencies (100k ~ 500 kHz).

The final result of rubber attenuation is plotted in Figure 2.19 over frequency range 100~700 kHz. Note that the unit of the attenuation in Figure 2.19 is dB/cm (normalized by the thickness of the rubber). Figure 2.19 contains the overlay of attenuation using all 100 Gaussian pulses and the blue line is the curve obtained by averaging the results at each frequency.

The attenuation results show more deviation from the mean in the lower frequency range, i.e. between 100 ~ 280 kHz; while in the higher frequency range, they conform to the mean quite well. This is due to the limitation of the system and pulse compression technique. The attenuation measurement is not trivial in the frequency range

of interest here (reference from Francois). The results above 300 kHz here are more reliable and the main reason for that is the signal-to-noise ratio (SNR). In the lower frequency range, the SNR is low since the system is driven well below the resonance; on the other hand, as fixing the bandwidth to be 30% of the center frequency, the Gaussian pulses ended up using is not "short" in time. Therefore, a limited number of cycles are allowed to be sent at the low frequencies, which is not helping with the SNR.

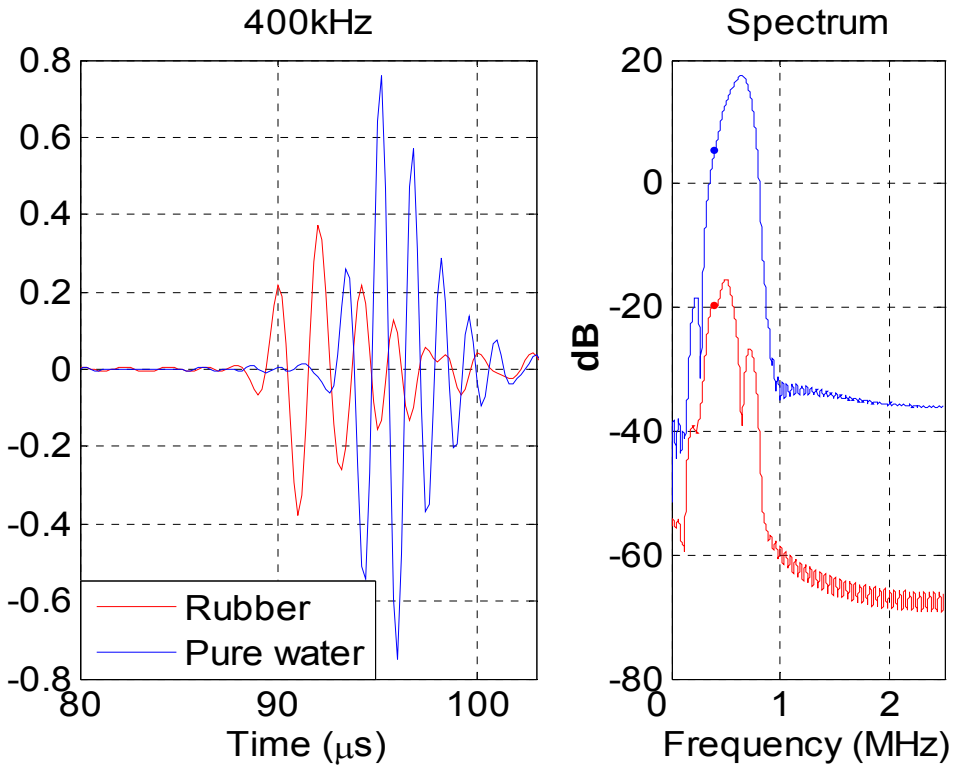

Figure 2.18 Rubber attenuation measurement at 400 kHz. The data for the rubber (left) has been multiplied by 30. Dots: spectrum level at selected frequency.

As a compulsory parameter for the experiment and modeling, the attenuation coefficients have to be found in the frequency range 100~300 kHz. The Institute of Acoustics, the Chinese Academy of Sciences (IOA) helped us measure the rubber attenuation using an acoustic tube in the frequency range 50~70 kHz in water. Figure

2.20 includes their measurements (magenta circles) along with ours and power law curve fitting scheme is used:

$$\alpha = K f^{n} \tag{2.4}$$

Here, α stands for attenuation, K is called attenuation coefficient in dB/m*kHz, f is frequency in kHz, and n is the power dependence. Two curve fitting results are shown on the figure: the black curve is from only using the pulse compression results for frequency higher than 280 kHz; the blue curve is from both the same high frequency pulse compression results and low frequency results from IOA (magenta circles). The two curve fitting results are fairly close to each other and the total curve fitting results for later use:

$$\alpha = 0.0459 \times f^{0.861} \tag{2.5}$$

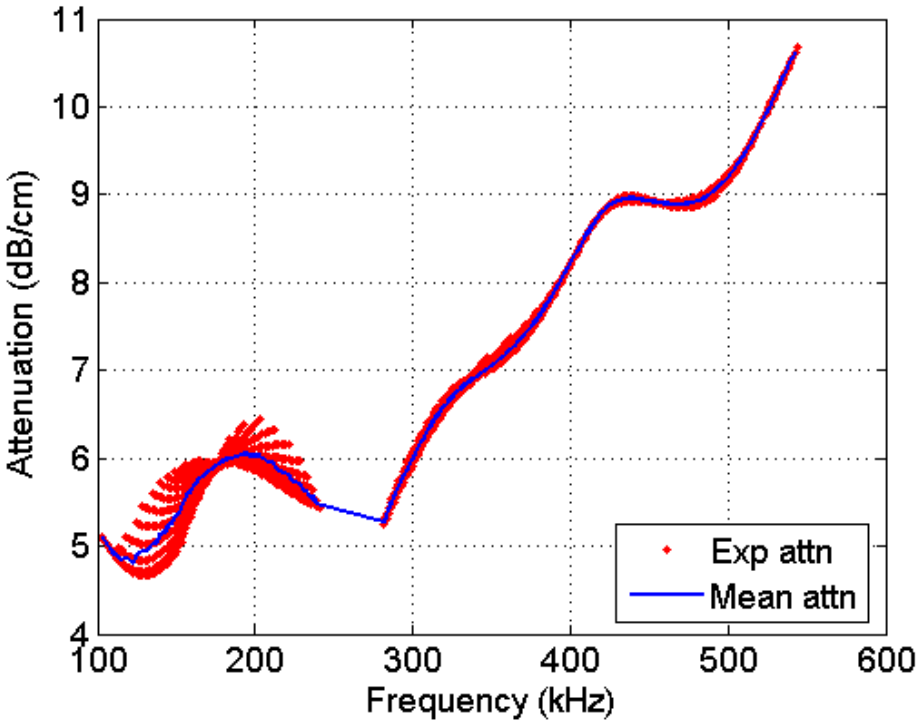

Figure 2.19 Attenuation in rubber as a function of frequency.

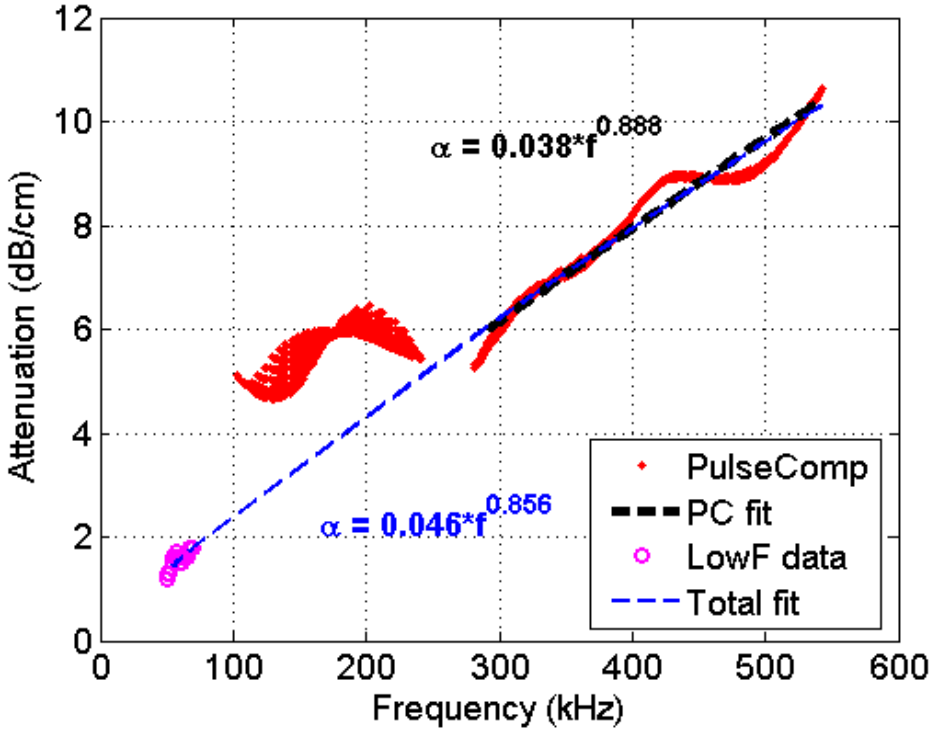

Figure 2.20 Curve fitting result of rubber attenuation using power law.

CHAPTER 3

PROPAGATION MODELS

Two most widely used propagation models in shallow water acoustics are normal mode method and the parabolic equation method. Both start from the Helmholtz or the wave equation and provide acoustic field information in different forms. The former presents acoustic pressure in terms of normal modes or eigenfunctions; while the latter calculates pressure directly. It depends on the nature of the problem to decide which approach to use. Concerning the computational efficiency, the parabolic equation method, which calculates the acoustic field using the Fast Fourier transform, is better than the normal mode method. Both methods can handle range dependent cases and the normal mode method is more convenient to study mode coupling due to changing environment. In this thesis, both theories are used and therefore, brief derivations are presented in 3.1 and 3.2 respectively.

3.1 Normal Mode Method

Normal mode theory can be found in standard textbooks (Jensen et al., 2000). What we present here is an abbreviated derivation based on the method of separation of variables. The Helmholtz equation in cylindrical coordinates is given by:

$$\frac{1}{r}\frac{\partial}{\partial r}\left(r\frac{\partial p}{\partial r}\right)+\rho(z)\frac{\partial}{\partial z}\left(\frac{1}{\rho(z)}\frac{\partial p}{\partial z}\right)+\frac{\omega^2}{c^2(z)}p=-\frac{\delta(r)\delta(z-z_s)}{2\pi r} \tag{3.1}$$

Here, p, ρ, c, z_s represent acoustic pressure, density, sound speed, and depth of source. The right hand side of eq. (3.1) corresponds to a source function at range r and depth z_s.

To solve the wave equation, we first apply separation of variables $p(r,z)=\Phi(r)\Psi(z)$ to the unforced case, i.e. replacing the right-hand-side of eq.(3.1) by zero:

$$\frac{1}{\Phi}\left[\frac{1}{r}\frac{d}{dr}\left(r\frac{d\Phi}{dr}\right)\right]+\frac{1}{\Psi}\left[\rho(z)\frac{d}{dz}\left(\frac{1}{\rho(z)}\frac{d\Psi}{dz}\right)+\frac{\omega^2}{c^2(z)}\Psi\right]=0 \tag{3.2}$$

Assigning $-k_{rm}^2$ and k_{rm}^2 (constants) to each term of eq. (3.2), we obtain the modal equation:

$$\rho(z)\frac{d}{dz}\left[\frac{1}{\rho(z)}\frac{d\Psi_m(z)}{dz}\right]+\left[\frac{\omega^2}{c^2(z)}-k_{rm}{}^2\right]\Psi_m(z)=0 \tag{3.3}$$

This is a classical Sturm-Liouville problem with eigenvalue k_{rm} and eigenfunction $\Psi_m(z)$. The boundary conditions are:

(1) pressure release surface: $\Psi(z=0)=0$;

(2) continuity of pressure and normal velocity at the bottom interface (subscript "b" denotes bottom):

$$\Psi(z=H) = \Psi_b(z=H)$$
$$\left.\frac{1}{\rho}\frac{d\Psi(z)}{dz}\right|_{z=H} = \left.\frac{1}{\rho_b}\frac{d\Psi_b(z)}{dz}\right|_{z=H}$$

We can re-write pressure in terms of normal modes:

$$p(r,z) = \sum_{m=1}^{\infty}\Phi_m(r)\Psi_m(z) \tag{3.4}$$

and the Helmholtz equation (3.1) is now:

$$\sum_{m=1}^{\infty}\left[\frac{1}{r}\frac{d}{dr}\left(r\frac{d\Phi_m(r)}{dr}\right)\right]\Psi_m(z)+\Phi_m(r)\left[\rho(z)\frac{d}{dz}\left(\frac{1}{\rho(z)}\frac{d\Psi_m(z)}{dz}\right)+\frac{\omega^2}{c^2(z)}\Psi_m(z)\right] = -\frac{\delta(r)\delta(z-z_s)}{2\pi r} \tag{3.5}$$

Using modal equation (3.3), equation (3.5) can be rewritten as:

$$\sum_{m=1}^{\infty}\left[\frac{1}{r}\frac{d}{dr}\left(r\frac{d\Phi_m(r)}{dr}\right)\right]\Psi_m(z)+k_{rm}^2\Phi_m(r)\Psi_m(z)=-\frac{\delta(r)\delta(z-z_s)}{2\pi r} \tag{3.6}$$

Using the orthogonality property $\int_0^H \Psi_m(z)\Psi_n(z)/\rho(z)dz=\delta_{mn}$ and eq. (3.3), we find:

$$\frac{1}{r}\frac{d}{dr}\left(r\frac{d\Phi_m(r)}{dr}\right)+k_{rm}^2\Phi_m(r)=-\frac{\delta(r)\Phi_m(z_s)}{2\pi r\rho(z_s)} \tag{3.7}$$

The solution to eq. (3.7) is then found to be:

$$\Phi_m(r)=\frac{i}{4\rho(z_s)}\Psi_m(z_s)H_0^{(1)}(k_{rm}r) \tag{3.8}$$

$H_0^{(1)}(k_{rm}r)$, satisfying the homogeneous equation of (3.7), is the zeroth order first kind Hankel function and represents waves propagating outward. Combining eq. (3.4), the final form for the pressure can be written as:

$$p(r,z)=\frac{i}{4\rho(z_S)}\sum_{m=1}^{M}\Psi_m(z_s)\Psi_m(z)H_0^{(1)}(k_{rm}r) \tag{3.9}$$

Pressure can further be simplified by changing the Hankel function to its asymptotic form if sufficiently far from the source ($k_{rm}r>>1$):

$$H_0^{(1)}\approx\sqrt{\frac{2}{\pi k_{rm}r}}\exp(-i\frac{\pi}{4})\exp(ik_{rm}r) \tag{3.10}$$

$$p(r,z)=\frac{i}{\rho(z_S)}\sqrt{\frac{1}{8\pi r}}\exp(-i\pi/4)\sum_{m=1}^{M}\Psi_m(z_s)\Psi_m(z)\frac{\exp(ik_{rm}r)}{\sqrt{k_{rm}}} \tag{3.11}$$

In principle, a real seabed has certain bottom loss. Therefore, the eigenvalue k_{rm} calculated is a complex number with the imaginary part representing attenuation:

$$k_{rm}=k_{rm,r}+i\alpha_m \tag{3.12}$$

The real part k_{rm} is the horizontal wave number while the imaginary part α_m is referred to as the modal attenuation coefficient. This modal attenuation coefficient α_m increases with

mode number which results in faster attenuation of higher order modes, i.e. mode stripping. With eq. (3.12), the acoustic pressure (3.11) can be re-written as:

$$p(r,z) = \frac{i}{\rho(z_S)}\sqrt{\frac{1}{8\pi r}}\exp(-i\pi/4)\sum_{m=1}^{M}\Psi_m(z_s)\Psi_m(z)\frac{\exp(ik_{rm,r}r)}{\sqrt{k_{rm,r}}}e^{-\alpha_m r} \tag{3.13}$$

To simulate acoustic propagation, the phase and group velocities are also crucial. They can be readily derived from the eigenvalues and eigenfunctions. The modal phase speed can be written as: $C_{pm} = \omega / k_{rm,r}$ which results in a different phase speed for each mode. The phase speed also changes with frequency which is referred to as *dispersion*. The modal group velocity, by definition, is: $C_{gm} = d\omega / dk_{rm,r}$ and can be calculated using the eigenfunctions (Koch et al 1983; Chapman et al 1983):

$$\frac{dk_{rm,r}}{d\omega} = \frac{\omega}{k_{rm,r}}\int_0^H \frac{\Psi_m{}^2(z)}{\rho(z)c^2(z)}dz \Big/ \int_0^H \frac{\Psi_m{}^2(z)}{\rho(z)}dz \tag{3.14}$$

Based on the normal mode theory, the un-normalized vertical cross-correlation coefficient can be written as:

$$\begin{aligned}\Gamma &= \left\langle P(r,z)P^*(r,z+d_v)\right\rangle \\ &= \frac{1}{8\pi r\rho(z_s)} < \sum_{m=n}\left|\Psi_m(z_s)\right|^2\Psi_m(z)\Psi_m{}^*(z+d_V)\frac{e^{-2\alpha_m r}}{k_{rm}} + \\ &\sum_{m\neq n}\Psi_m(z_s)\Psi_m(z)\Psi_n^*(z_s)\Psi_n^*(z+d_V)\frac{e^{i[(k_{rm}-k_{rn})r]}e^{-(\alpha_m+\alpha_n)r}}{\sqrt{k_{rm}k_{rn}}} >\end{aligned} \tag{3.15}$$

In this equation, k_{rm} represent the real part of the original definition of $k_{rm,r}$ in eq. (3.12) for short. In addition, d_V is the vertical separation between two hydrophones. The first term estimates the coherent component of the cross-correlation coefficient while the second term represents the interference between all modes.

For deterministic process, the cross-correlation between two hydrophones is to follow eq.(3.15) without the ensemble average. As randomness from the sea surface and internal waves comes in (Chapter 6 and 7), the cross-correlation coefficient is the averaged results of many realizations.

As an example, Figure 3.1 displays a few selected mode shapes using the sound speed profile on the left. This sound speed profile was recorded in the ECS in 2001 using CTD. The water depth is 104m. At 300 Hz, a total of 22 propagating modes have been generated in this case. In this particular example, no randomness is included. The main purpose of showing Figure 3.1 is the mode shapes as a function of depth. For a typical downward refracting sound speed profile, the lower order modes have high amplitudes below the thermocline which is to say, above or within the thermocline, it is mostly high modes. This the main cause that decorrelates the acoustic signal. In addition, if the source depth is below the thermocline, it will excite stronger low modes than the source depth above or within the thermocline. Therefore, positioning the source below the thermocline will help the signal coherence.

To study sound propagation, transmission loss is a very important parameter. Transmission loss is defined as the logarithmic ratio between the acoustic pressure or intensity and a reference point (1m from the source):

$$TL = -20\log\frac{|p(r,z)|}{|p_0(r=1)|} = -10\log\frac{|I(r,z)|}{|I_0(r=1)|} \tag{3.16}$$

Using (3.13), transmission loss, also referred to as coherent transmission loss, can be written as:

$$TL \cong -20\log\left|\sum_m \Psi_m(z_s)\Psi_m(z)e^{ik_{rm}r}\Big/\sqrt{k_{rm}r}\right| \tag{3.17}$$

The incoherent transmission loss is more like an "averaged" result and defined as:

$$TL \cong -20\log\sqrt{\sum_m \left|\Psi_m(z_s)\Psi_m(z)e^{ik_{rm}r}\Big/\sqrt{k_{rm}r}\right|^2} \tag{3.18}$$

Figure 3.2 shows the comparison between coherent and incoherent transmission loss curves under the same condition as Figure 3.1. Here source and receiver depth are both at 50 meters.

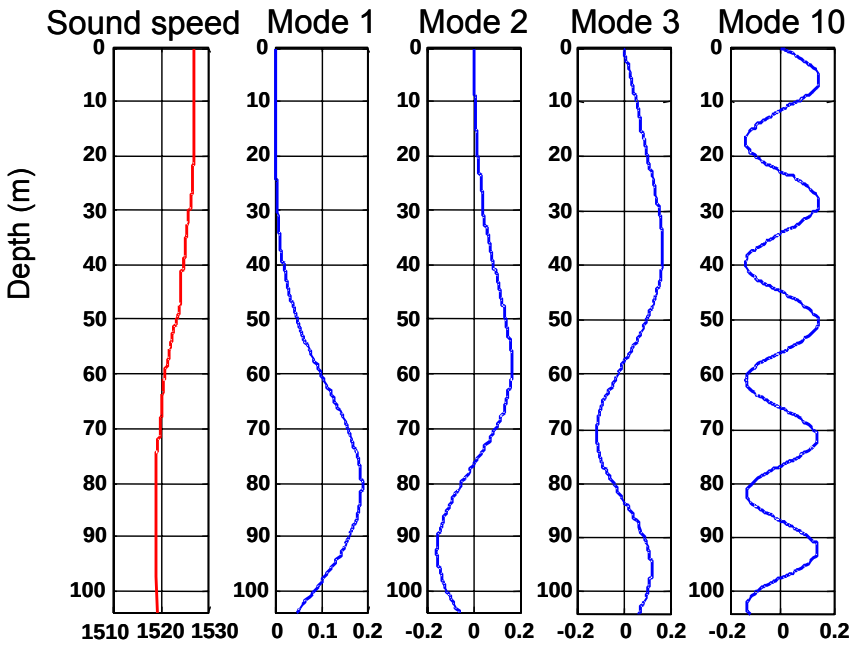

Figure 3.1 Sample normal mode shapes calculated using CTD data (left).

3.2 Parabolic Equation Method

The parabolic equation method, introduced by Hardin and Tappert(1973) into ocean acoustics, has become the most popular wave-theory technique for solving range-dependent propagation problems due to its flexibility and computational efficiency.

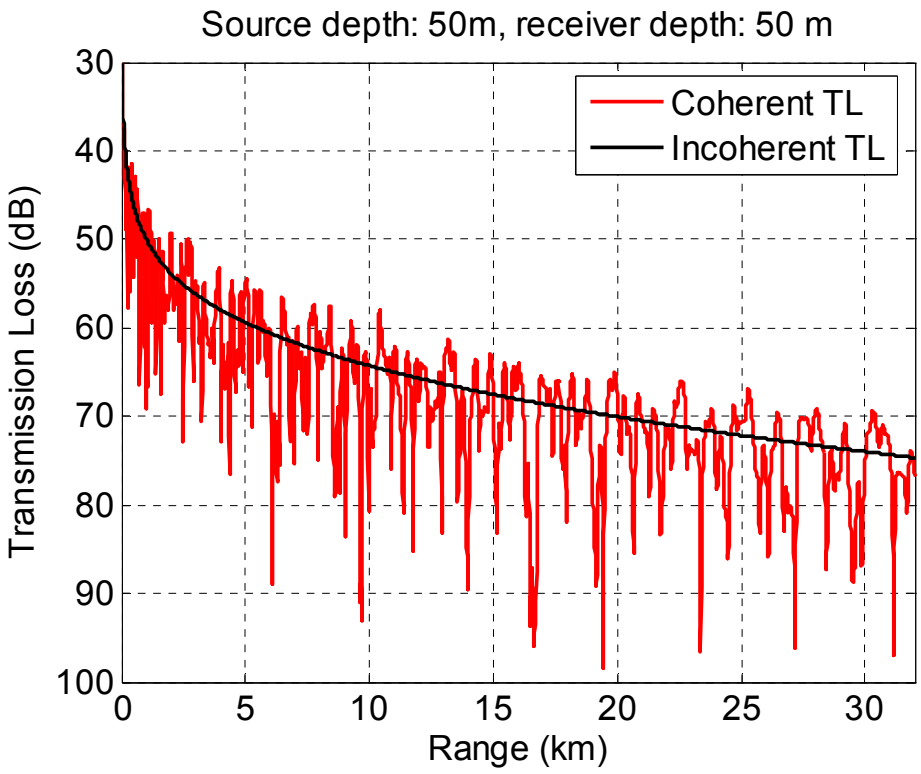

Figure 3.2 Transmission losses at 300Hz.

Starting from the Helmholtz equation (3.1), we obtain:

$$\frac{\partial^2 p(r,z)}{\partial r^2}+\frac{1}{r}\frac{\partial p(r,z)}{\partial r}+\rho\frac{\partial}{\partial z}\left(\rho\frac{\partial p(r,z)}{\partial z}\right)+k_0^2 n^2 p(r,z)=0 \qquad (3.19)$$

Here, $k_0=\frac{\omega}{c_0}$ is the reference wavenumber and $n(r,z)=\frac{c_0}{c(r,z)}$ is the index of refraction.

Tappert (1977) assumed the pressure can be written as: $p(r,z)=\Psi(r,z)H_0^{(1)}(k_{rm}r)$ and substitute p in eq. (3.19):

$$\frac{\partial^2\psi}{\partial r^2}+\left(\frac{2}{H_0^{(1)}(k_0 r)}\frac{\partial H_0^{(1)}(k_0 r)}{\partial r}+\frac{1}{r}\right)\frac{\partial\psi}{\partial r}+\frac{\partial^2\psi}{\partial z^2}+k_0{}^2\left(n^2-1\right)\psi=0 \qquad (3.20)$$

Employing the farfield assumption $k_0 r >> 1$ and the paraxial approximation $\frac{\partial^2 \psi}{\partial r^2} << 2ik_0 \frac{\partial \psi}{\partial r}$ to eq. (3.20), we arrive at the standard parabolic equation:

$$2ik_0 \frac{\partial \psi}{\partial r} + \frac{\partial^2 \psi}{\partial z^2} + k_0^2 \left(n^2 - 1\right)\psi = 0 \tag{3.21}$$

Take spatial FFT, eq. (3.21) can be written as:

$$2ik_0 \frac{\partial \psi}{\partial r} - k_z^2 \psi + k_0^2 \left(n^2 - 1\right)\psi = 0 \tag{3.22}$$

Eq.(3.22) can be rearranged as: $\frac{\partial \psi}{\partial r} = -\frac{k_0^2\left(n^2 - 1\right) - k_z^2}{2ik_0}\psi$ which has a simple solution:

$$\psi\left(r, k_z\right) = \psi\left(r_0, k_z\right) \exp\left(-\frac{k_0^2\left(n^2 - 1\right) - k_z^2}{2ik_0}\left(r - r_0\right)\right) \tag{3.23}$$

The final solution (3.23) to the parabolic equation needs to be transformed from the wavenumber domain back to the z domain. Denoting $r - r_0$ by Δr, the inverse transform of (3.23) is:

$$\psi\left(r, z\right) = \exp\left[\frac{ik_0\left[n^2\left(r_0, z\right) - 1\right]}{2}\Delta r \right] \int_{-\infty}^{+\infty} \psi\left(r_0, k_z\right) \exp\left[-\frac{ik_z^2}{2k_0}\Delta r \right] e^{ik_z z}\, dk_z$$

or:

$$\psi\left(r, z\right) = \exp\left[\frac{ik_0\left[n^2\left(r_0, z\right) - 1\right]}{2}\Delta r \right] \Im^{-1}\left\{ \exp\left[-\frac{i\Delta r}{2k_0} k_z^2 \right] \Im\left\{\psi\left(r_0, z\right)\right\}\right\} \tag{3.24}$$

Here, the symbols $\Im$ and $\Im^{-1}$ represent the Fourier and its inverse transform. This is called the split-step Fourier results and it enables one to go from any range r1 to r2 by stepping along.

The program used in this thesis to solve parabolic equation is called Range-dependent Acoustic Model (RAM by Collins, 1993). RAM is the most efficient PE algorithm that has been developed (Collins et al, 1996). It solves the following equation:

$$\left[\frac{\partial^2}{\partial r^2}+\rho\frac{\partial}{\partial z}\left(\frac{1}{\rho}\frac{\partial}{\partial z}\right)+k_0{}^2\left(n^2-1\right)\right]\psi=0 \tag{3.25}$$

Eq. (3.25) is the same as eq. (3.19) except that the second term is neglected due to farfield approximation. The goal is to factor the operator, the bracketed term in (3.25), into two components:

$$\left[\frac{\partial}{\partial r}+ik_0\left(1+Y\right)^{1/2}\right]\left[\frac{\partial}{\partial r}-ik_0\left(1+Y\right)^{1/2}\right]p=0 \tag{3.26}$$

where $Y=\left(\rho\frac{\partial}{\partial z}\frac{1}{\rho}\frac{\partial}{\partial z}+k^2-k_0^2\right)\Big/k_0^2$. Assuming out-going wave, the second component is chosen which gives solution to (3.26) as:

$$p\left(r+\Delta r,z\right)=\exp\left[ik_0\Delta r\left(1+Y\right)^{1/2}\right]p\left(r,z\right) \tag{3.27}$$

The solution can be approximated using Padé series:

$$p\left(r+\Delta r,z\right)=\exp\left(ik_0\Delta r\right)\left(1+\sum_{j=1}^{n}\frac{\gamma_{j,n}Y}{1+\beta_{j,n}Y}\right)p\left(r,z\right) \tag{3.28}$$

where n is the number of terms in the expansion and

$$\gamma_{j,n}=\frac{2}{2n+1}\sin^2\left(\frac{j\pi}{2n+1}\right),\qquad \beta_{j,n}=\cos^2\left(\frac{j\pi}{2n+1}\right) \tag{3.29}$$

Figure 3.3 is the color plot of the sound field over 30 kilometers calculated by RAM including the slightly changing water depth effect. RAM can take environmental parameter changes at arbitrary range which is convenient for many problems. The RAM program is versatile to solve several kinds of acoustic problems such as waveguide with

fluid or elastic bottom, surface and bottom roughness, and changes of the medium due to internal waves. The program reads an input file which defines the bathymetry change along a certain range, sediment parameters, and most important, the sound speed profile. For example, the calculation of acoustic effects due to internal waves is done through the input of a set of changing sound speed profiles along the range. The statistical characteristics of internal waves are preserved in the varying sound speed field. The surface waves can be included in the same program in a similar manner. The surface waveheight distribution is calculated as a random process and then used as the top boundary conditions in the model. For both internal and surface waves, the computation of the field will be repeated many times using different sound speed field or surface roughness realization to achieve the ensemble average in eq. (3.15).

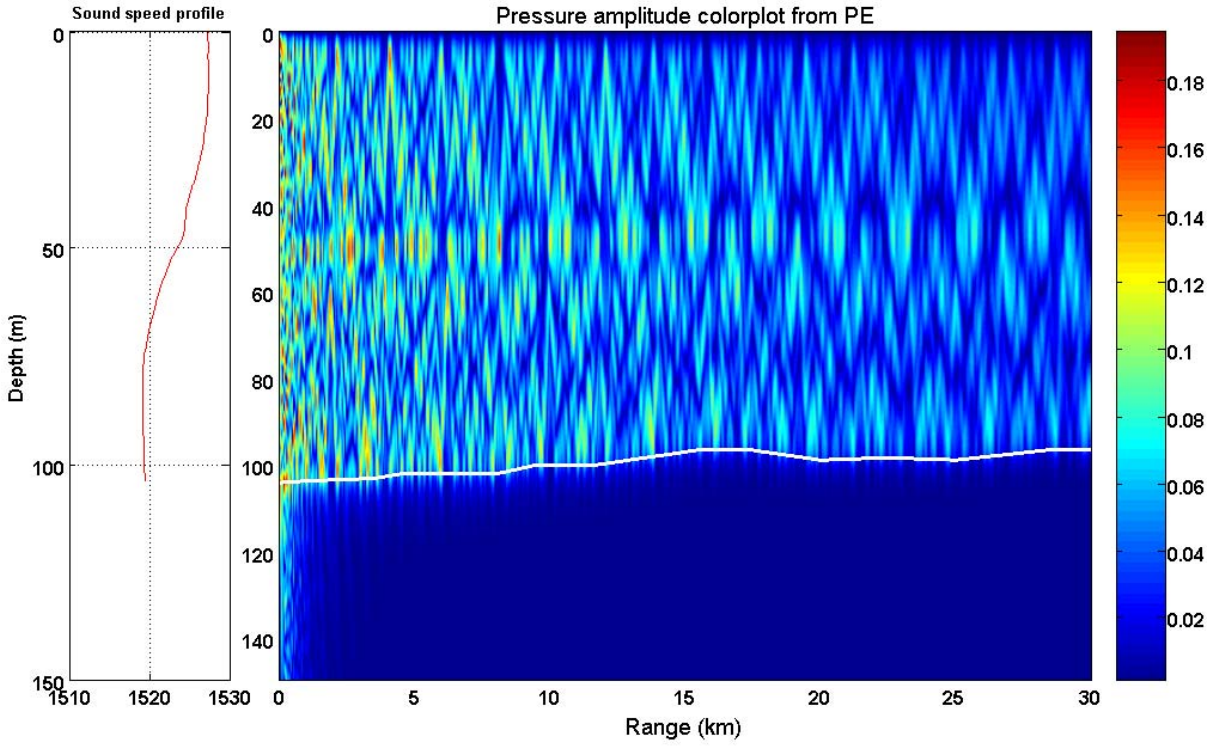

Figure 3.3 Pressure field color plot using the SSP from ASIAEX.
White line indicates varying water depth.

CHAPTER 4

CHARACTERISTICS OF VERTICAL COHERENCE

IN SHALLOW WATER

4.1 Acoustic Measurements in ASIAEX'01

The acoustic data we will concentrate on are wideband explosive signals (38 gram TNT). The locations of the signals and acoustic track followed can be found in figure 2.2. The SUS charge signals were deployed at a nominal depth of 50m (there were a few signals deployed at 25m which will be noted when used). Figure 4.1 is an example of a 38g SUS charge signal recorded at a distance of 30 km. The received waveform is shown on the left which is the combination of the actual signal, a bubble pulse created by the explosion, dispersion, multiple reflections/scattering, and noise.

For long range sound propagation, the frequency range of interest is usually below 2 kHz. In terms of normal mode theory, sound propagation is different at each frequency due to the total number of propagating modes, group and phase velocities and the attenuation. Therefore, we filter the original wide-band signal over 1/3 octave bands. Figure 4.2 (a) and (b) show the filtered waveforms from two channels at center frequency 100Hz using the signal shown in Figure 4.1. The original impulse-like waveform, which is about 0.05s in duration, is now spread out to about 0.3s due to dispersion. Dispersion is an effect where both phase and group velocities vary with frequency and mode number. Dependence on the latter is usually referred to as modal dispersion. In principle, lower order modes have higher group velocities which can be used to separate them in time at a

sufficient distance. As an example, the top two figures of Figure 4.2 both show two distinct packets which correspond to mode 1 and 2.

The cross-correlation function between the two channels is presented in Figure 4.2(c) and (d). From the complete cross-correlation function (c), it is apparent that the amplitude of a cross-correlation function depends on how the wave packets line up with each other. As mentioned in Chapter 1, we are interested in the cross-correlation coefficient, the cross-correlation function at zero delay, i.e. t = 0 in Figure 4.2(d).

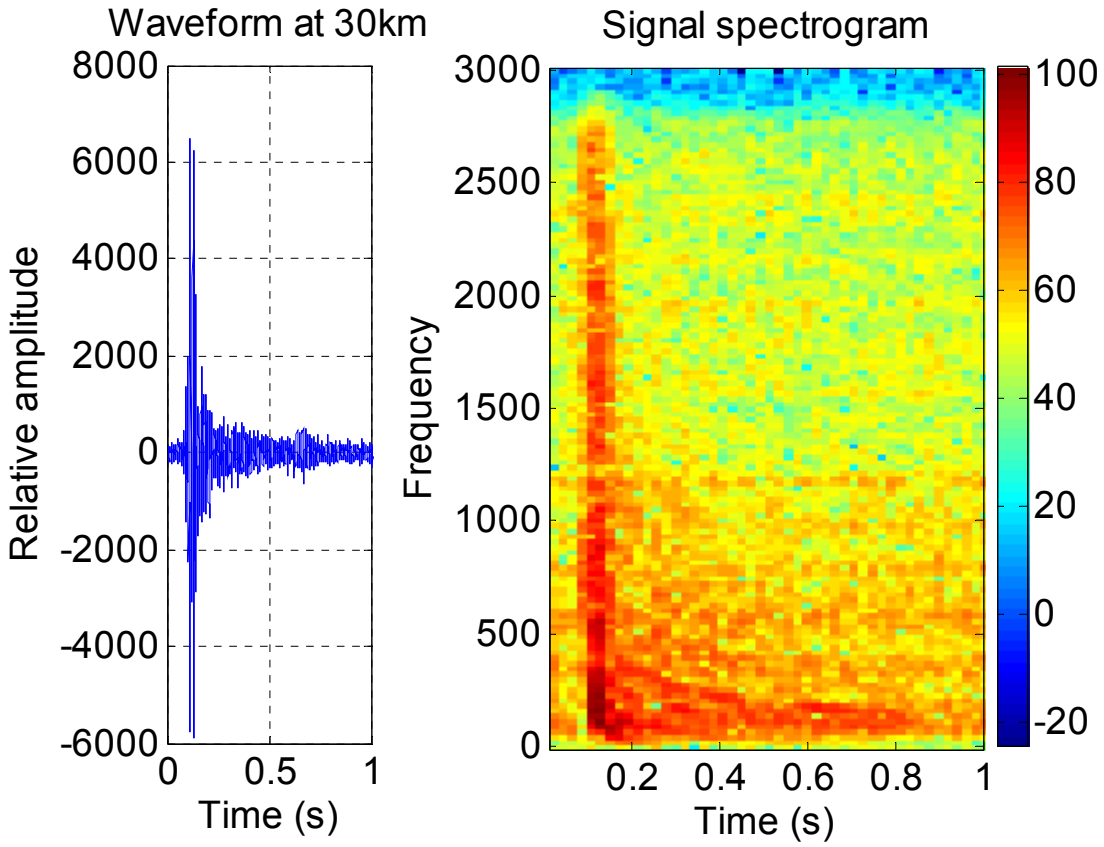

Figure 4.1 Sample SUS charge signal and its spectrogram received at 30km.

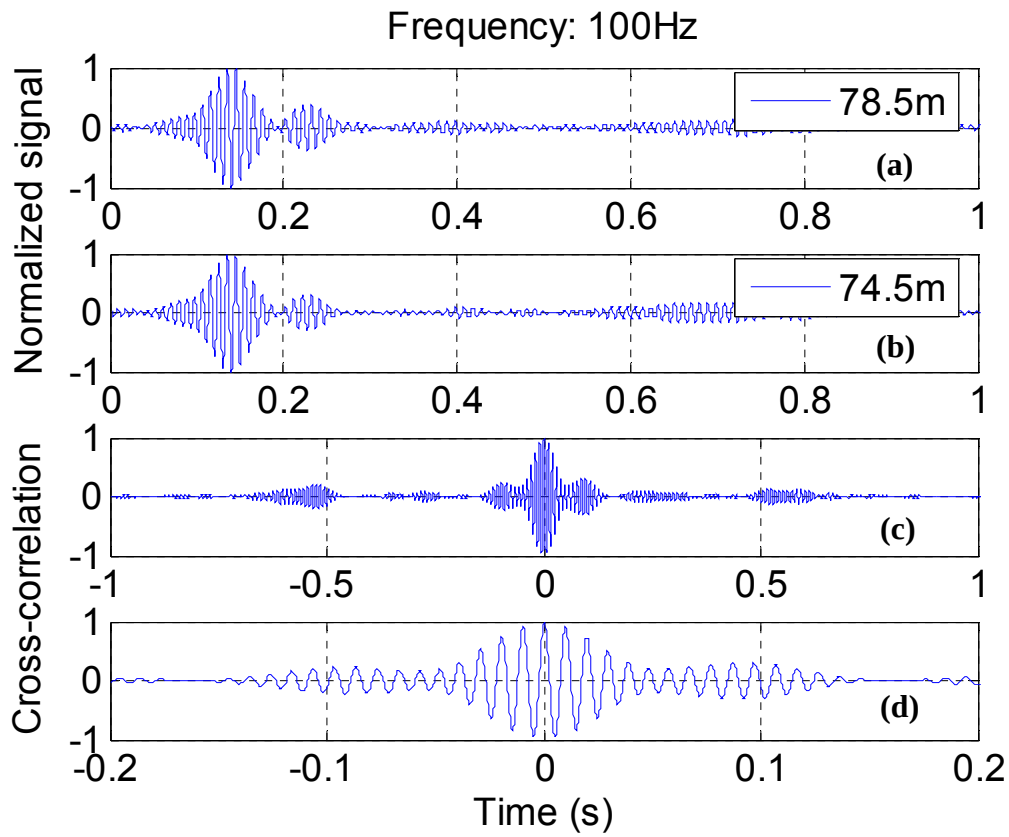

Figure 4.2 (a), (b): 1/3-ocatve filtered signal of two channels;
(c), (d): their complete and zoomed-in cross-correlation function.

4.2 Characteristics of Vertical Coherence Observed in the ECS

4.2.1 Characteristics of Vertical Coherence of Sound Propagation

Vertical coherence is a function of frequency, spacing between the hydrophones, and propagating range eq. (3.15) as well as all the environmental factors that influence sound propagation. For the calculation of vertical coherence, a time window of 1.4 seconds is applied to the SUS charge signals.

Figure 4.3 shows the coupled effect of frequency (expressed in terms of wavenumber $k=2\pi/\lambda$) and spacing on vertical coherence (some literature refers to this as *kd*-plot or D/λ plot). At these ranges, the vertical coherence level is high if spacing is

smaller than one wavelength, and it falls off to zero as the spacing becomes about twice or three times the wavelength. This information is useful in designing a hydrophone array to do an experiment at sea. In addition, the uncertainties increase as the vertical coherence decreases with the ratio of D/λ. Alternatively, if we fix the spacing (Figure 4.4), the coherence level decreases with increasing frequency (increasing ratio of spacing and wavelength). In discussing Figure 4.4, we need to mention the important phenomenon that coherence increases with range, which is due to mode stripping. In the derivation of normal mode theory, we mentioned that each mode has a different attenuation coefficient which is inversely proportional to its mode number. After long range propagation, it is usually the lower order modes that dominate the acoustic field. With fewer number modes, the summation of phase differences of all modes, eq. (3.15), shows less fluctuation and hence, has higher coherence. Once more, the uncertainties are observed to increase with decreasing coherence.

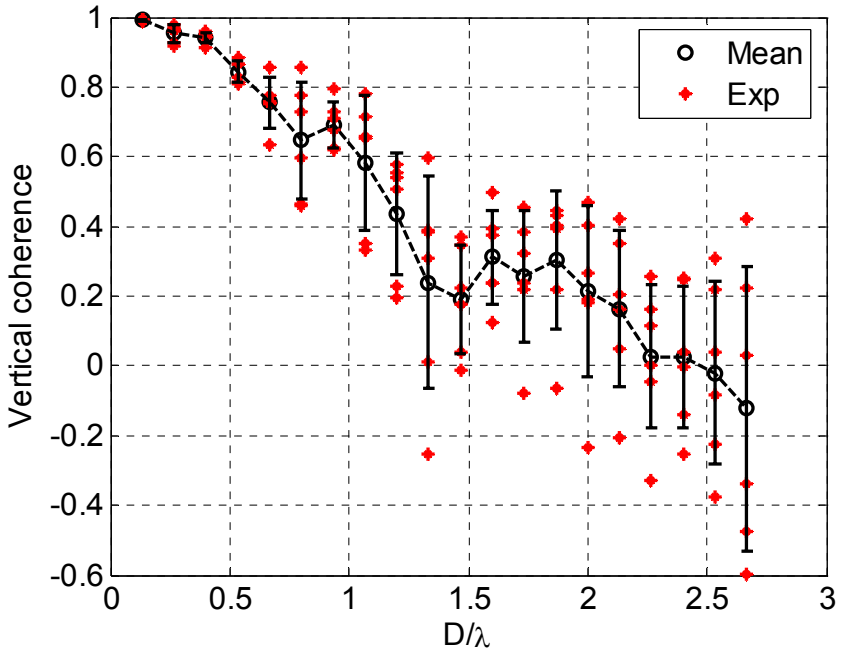

Figure 4.3 Vertical coherence kd- or D/λ-plot with uncertainties.

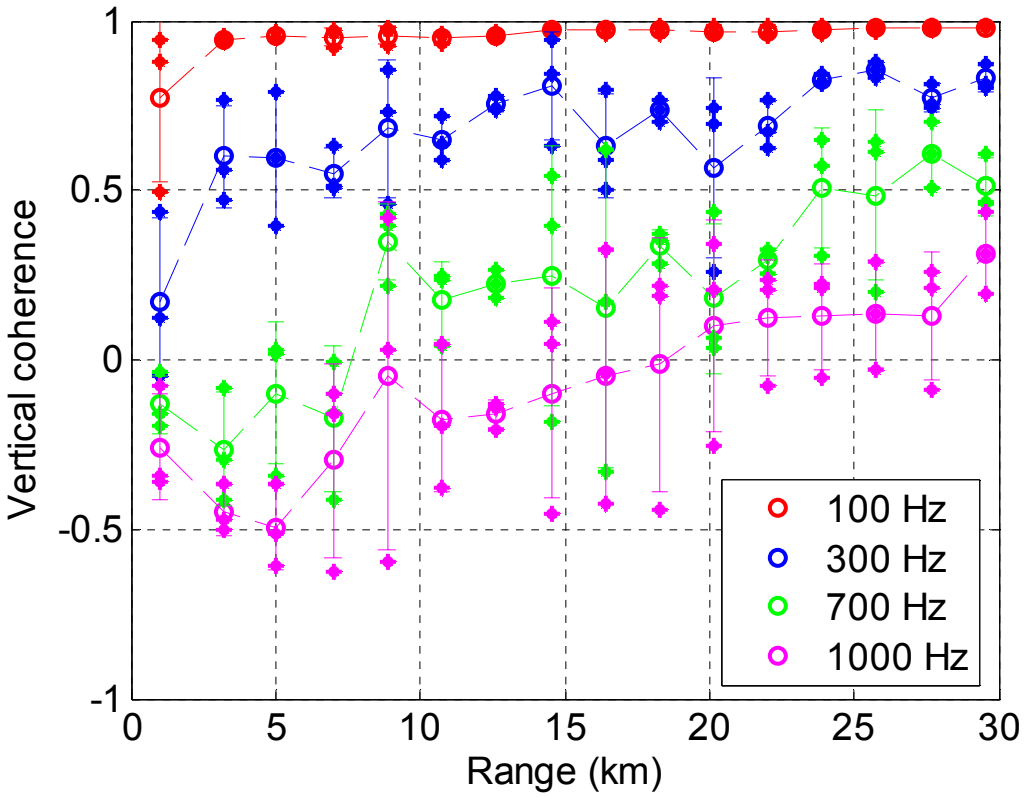

Figure 4.4 Vertical coherence versus range and frequency.

Results shown on Figures 4.3 and 4.4 are from measurements in the ME direction during which no apparent stochastic features such as internal waves were recorded. The sea state was fairly calm and the wind speed is only 3m/s. The results are showing mainly the deterministic effects of the waveguide on sound propagation.

4.2.2 Anisotropic Properties of Vertical Coherence

As mentioned in the section 2.1.2, there were azimuthal variations in sediment properties in ASIAEX. In addition, the internal waves are usually considered anisotropic, because they are affected by bathymetry, although a 3-D model has yet to be created. These factors can cause both temporal and spatial variations in the acoustic field.

We use the results from the wideband explosive sources deployed on the 30km circular track to show the azimuthal pattern of vertical coherence. It's unfortunate that some of the sources were deployed at a depth of 50m while others were at 25m resulting in totally different sound fields. However, by comparing the results of sources at the same depth, some conclusions can still be made.

At low frequency (below 500Hz), the vertical coherence is quite uniform for all angles (Figure 4.5) for both source depths. Anisotropic features start to show up above 500 Hz as in Figure 4.6. From both figures, it's obvious that signals deployed at 25m have significantly lower coherence level compared with the 50m case. This is because 25m is on the edge of the upper thermocline which excites mostly higher order modes for a downward refracting sound speed profile (Figure 3.1). Higher order modes introduce more fluctuations into the field and decorrelate the received signal.

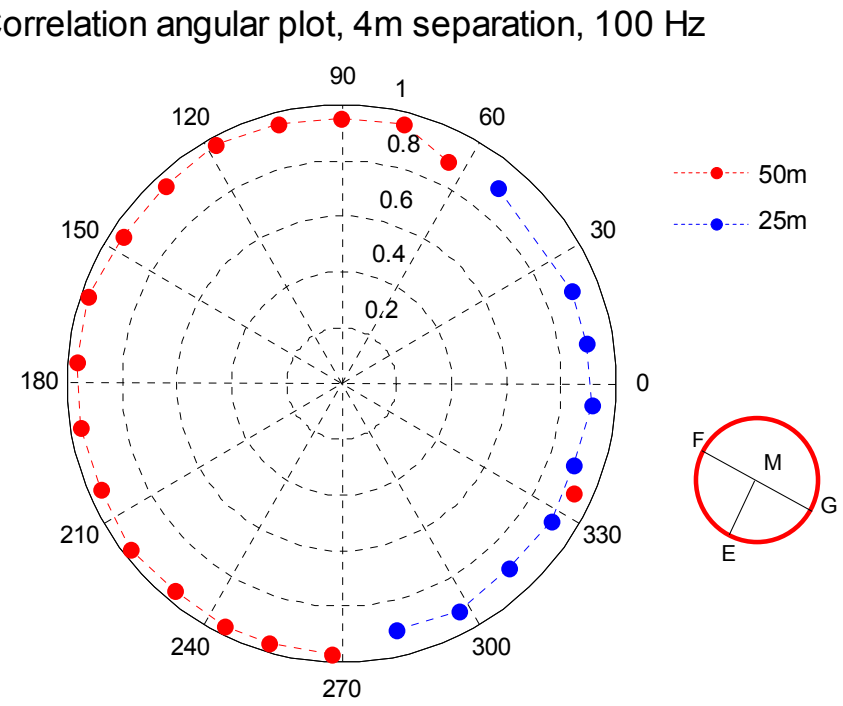

Figure 4.5 Cross-correlation angular plot on 30 km radius at 100 Hz.

In addition to the signals on the circular track, we can also look at the comparisons between three propagation directions M→E, F→M, and M→G. For the same pair of hydrophones, it's clear that Figure 4.7 shows higher signal coherence in the F→M direction relative to the other two directions especially when frequency becomes higher. In Figures 4.8 and 4.9, an unexpected, interesting phenomenon occurs. Here we have a smaller spacing between the two hydrophones (1.7m vs 4m) which are close to the upper boundary of the thermocline. At 1000Hz, the coherence level in the F→M direction drops significantly after 20km propagation while the two curves for the other directions look quite normal. This phenomenon exists for frequencies above 600Hz.

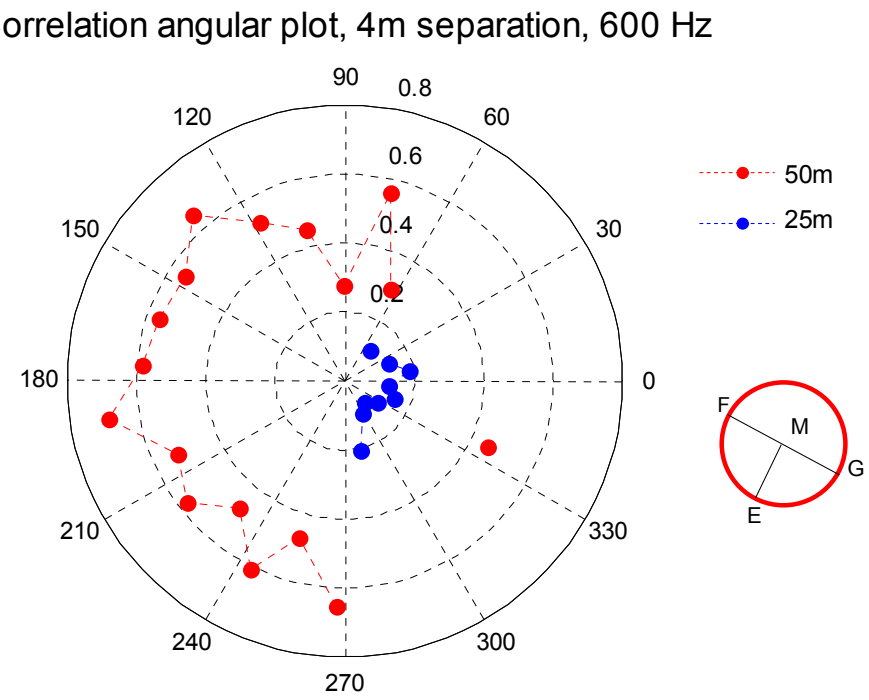

Figure 4.6 Cross-correlation angular plot on 30 km radius at 600 Hz.

There are two possible explanations for Figure 4.7: one is spatial variation in sediment properties, and the other is strong internal wave activity. From the coring

analysis, we observed an increase in bottom sound speed from F→G. In terms of normal modes, a faster bottom can support more propagating modes which will decorrelate the signal. This is saying that we should have better coherence level in the F→M direction than M→G. However, coring analysis has not indicate any drastic change in the sediment properties in FM which may cause the coherence to behave like figures 4.7~4.9. The other possible explanation is the internal waves since internal waves are usually assumed to propagate toward the shore that is, from M→F (Cairns, 1967). In addition, intensive internal tides and high frequency oscillations were observed during the measurement in the F→M direction (Figures 2.6 and 2.8). These oscillations may cause strong mode coupling in the sound waves. This hypothesis is to be tested using range dependent acoustic model which includes both the internal tides and the high frequency oscillations.

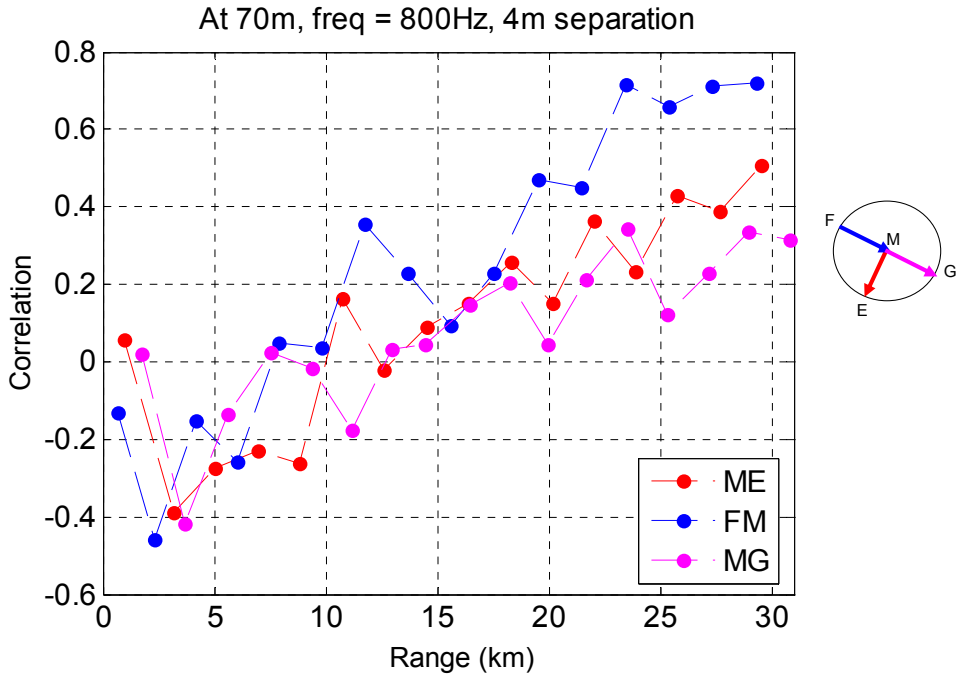

Figure 4.7 Cross-correlation comparisons of three propagation directions at 800 Hz.

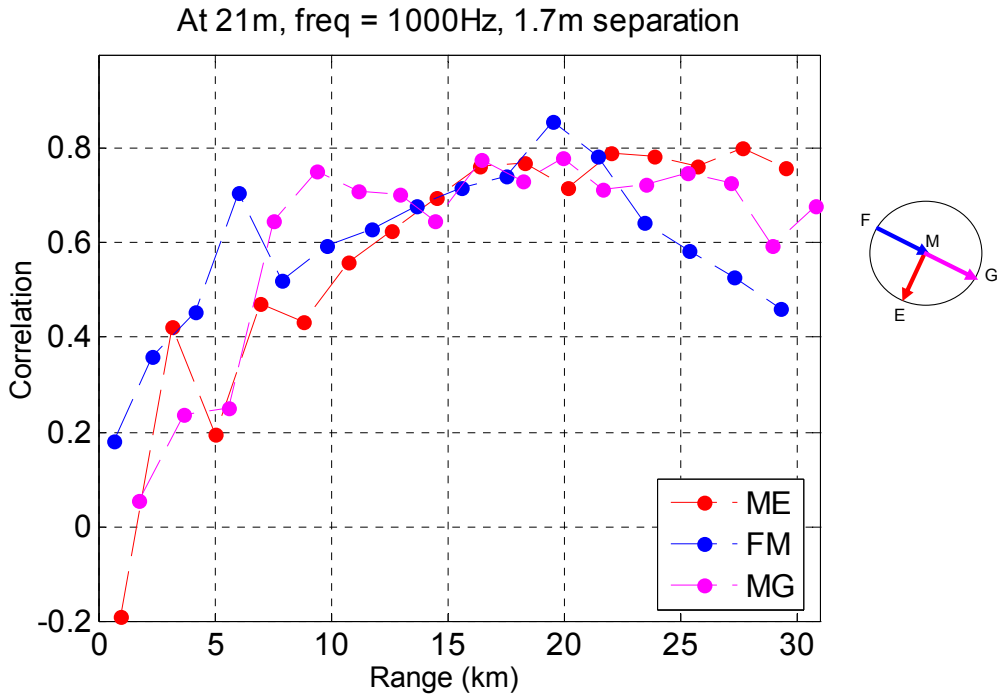

Figure 4.8 Cross-correlation comparisons of three propagation directions at 1000 Hz.

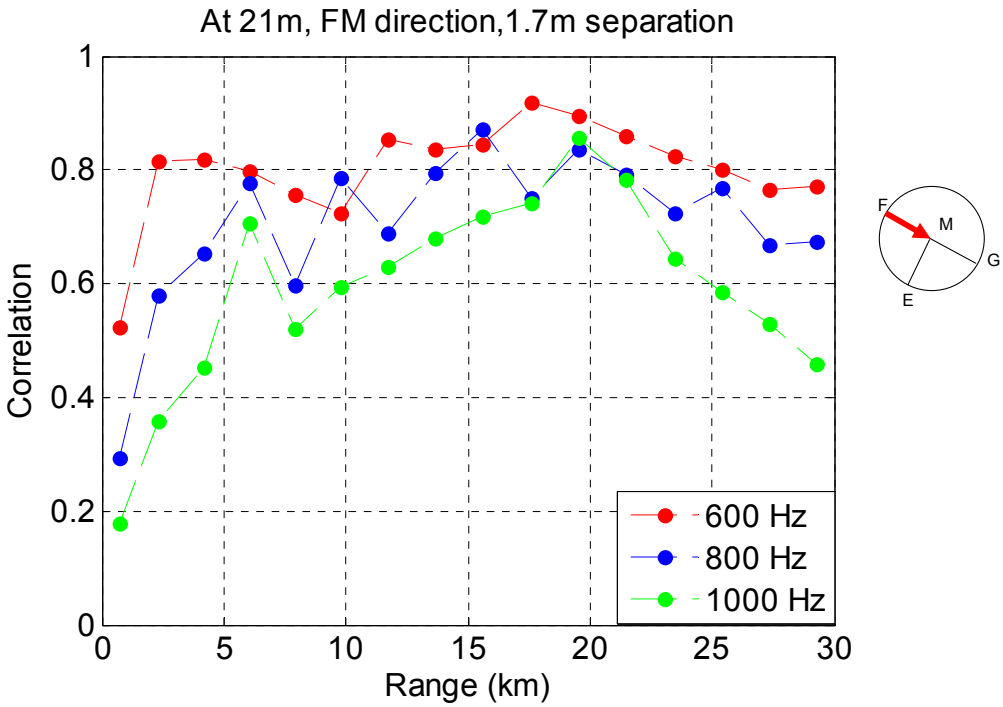

Figure 4.9 Cross-correlation comparisons of F-M direction at three frequencies.

CHAPTER 5

ENVIRONMENTAL PARAMETER I:

PROPERTIES OF THE SEABED

5.1 Geoacoustic Modeling of the Seabed

Several techniques have been developed to measure the properties of the sediments which include gravity and piston coring analysis, subbottom profiling using a water gun, and long-range sediment tomography. Still, direct measurement of sediment properties over a large area is impractical. The extracted sediments may change properties due to hydrostatic pressure, water temperature, porosity, etc. Consequently, inversion techniques are still a very important and convenient way in extracting seabed properties.

In this thesis work, a simplified three-parameter bottom model will be used. The parameters are: effective sediment sound speed, attenuation and density. In principle, only the surficial sediments, on the order of one or two wavelengths, will affect the long range acoustic propagation. For the frequency range of interest here, it is in the range of 1~10 meters. Due to this small penetration depth, it is more sensible to use this simplified model instead of trying to include the sub-bottom profiling which would be impractical to gather over a 30 km circular region.

An inversion technique will be introduced next based on normal mode theory. Sediment sound speed and attenuation are varied simultaneously and the sediment

parameters are taken to be the best match between experimental and modeled vertical coherence. The density is measured as 1.83 g/cm^3. The inverted sound speed, attenuation and effective bottom loss will be found as a function of frequency.

5.2 Inversion Techniques

We chose the M→E direction to show preliminary inversion results for a couple of reasons. One is that ME has fairly flat bottom over the 30 km range (Figure 2.2); two, ME measurements were done under very calm sea state (wind speed 3m/s); three, ME had little internal wave effects based on oceanographic data.

As derived in Chapter 3, the theoretical cross-correlation between two hydrophones is eq.(3.15). The expression for pressure is recited from eq. (3.13) as a reference.

$$p(r,z) = \frac{i}{\rho(z_S)}\sqrt{\frac{1}{8\pi r}}\exp(-i\pi/4)\sum_{m=1}^{M}\Psi_m(z_s)\Psi_m(z)\frac{\exp(ik_{rm,r}r)}{\sqrt{k_{rm,r}}}e^{-\alpha_m r} \qquad (3.13)$$

Let's look at the vertical cross-correlation without the ensemble averages ($d_L = 0$):

$$\gamma = P(r,z)P^*(r+d_{L,}z)$$

$$= \frac{1}{8\pi r\rho(z_s)}\left[\sum_{m=n}\left|\Psi_m(z_s)\right|^2\Psi_m(z)\Psi_m{}^*(z)\frac{e^{-2\alpha_m r}}{k_{rm}} + \sum_{m\neq n}\Psi_m(z_s)\Psi_m(z)\Psi_n^*(z_s)\Psi_n^*(z)\frac{e^{i[(k_{rm}-k_{rn})r]}e^{-(\alpha_m+\alpha_n)r}}{\sqrt{k_{rm}k_{rn}}}\right]$$

There are two terms in this equation. The first term, referred to as the incoherent sum of the same modes, is slow-varying while the second representing the interference pattern varies rapidly. The second term is often neglected when a smooth averaging is taken (Wang et al, 1992). Hence, the averaging of γ can be written as:

$$\gamma = \frac{1}{8\pi r \rho(z_s)} \left[\sum_{m=n} \overline{\Psi_m(z_s)^2}\ \overline{\Psi_m(z)\Psi_m{}^*(z+d_V)}\ \frac{e^{-2\alpha_m r}}{k_{rm}} \right] \tag{5.1}$$

Several studies have presented methods to evaluate the depth averaging functions in eq.(5.1) (Zhou et al, 1979; Wang et al, 1992; Ellis, 1995; Zhou et al, 2004). The first squared average mode function over depth is based on WKB approximations. For each mode, it can be expressed as (Zhang et al, 1987):

$$\overline{|\Psi_m(z)|^2} = \frac{1}{S_m \left[k^2(z) D(z) + k^2(z) - k_m^2(z) \right]^{1/2}} \tag{5.2}$$

Here, S_n is the cycle distance of each mode and can be calculated numerically by:

$$dk_{rm} / dm = -2\pi / S_n \tag{5.3}$$

k_m is the m^{th} eigenvalue and $k(z) = \omega/c(z)$ and they are related by:

$$k_{rm} = k(z)\cos\theta_m(z) \tag{5.4}$$

$\Theta_m(z)$ is usually referred to as the mode angle. Finally, the function D(z) in (5.2) is: $D(z) = 0.875 \left| \frac{1}{\pi f} \frac{dc(z)}{dz} \right|^{2/3}$. The second average term can be approximated by:

$$\overline{\Psi_m(z)\Psi_m{}^*(z+d_V)} = \overline{|\Psi_m(z)|^2}\ \cos\left(k(z) d_v \sin(\theta_m(z))\right) \tag{5.5}$$

For two vertically displaced hydrophones, the normalized cross-correlation from (5.1) can now be written as:

$$\Gamma(z, z_s, d_v) = \frac{\sum_m \overline{|\Psi_m(z_s)|^2}\ \overline{|\Psi_m(z)|^2}\ \cos\left(k(z) d_v \sin(\theta_m(z))\right) e^{-2\alpha_m r} / k_{rm}}{\sum_m \overline{|\Psi_m(z_s)|^2}\ \overline{|\Psi_m(z)|^2}\ e^{-2\alpha_m r} / k_{rm}} \tag{5.6}$$

The normalized cross-correlation (5.6) is used for deterministic prediction. When there is stochastic process, eq.(5.6) will be calculated for a certain number of time using

different eigenvectors and eigenvalues. The eigenvectors and eigenvalues are computed each time under the influence of the random process and an ensemble average is taken at the end. For the inversion results shown in this chapter, there is little randomness involved. This will help us concentrate on or decouple the sediment properties from the complex environment.

The inversion scheme is as follows: a wide range of values is given to both sound speed and attenuation. For each sound speed and attenuation, the normal mode eigenvalues and eigenfunctions are computed and used to calculate theoretical cross-correlation (5.1). The theoretical cross-correlation is evaluated at the ranges where experimental data were taken. The whole procedure is repeated as sound speed and attenuation varies and inversion result is selected based on the least-square-error between theory and experiment.

The vertical line array has 32 elements and the depth information is listed in Figure 2.4. Not all channels will be used for inversion here since some of them are too close to the surface or within the thermocline where sound speed fluctuates too much. The selected hydrophone pairs are shown in Figure 5.1. Most of the pairs below the thermocline have 4m separation except pair 3 (2m). Pairs with 4m separation will be used for inversion in the frequency range 300~800 Hz while 2m-separation pairs for 900~1500 Hz.

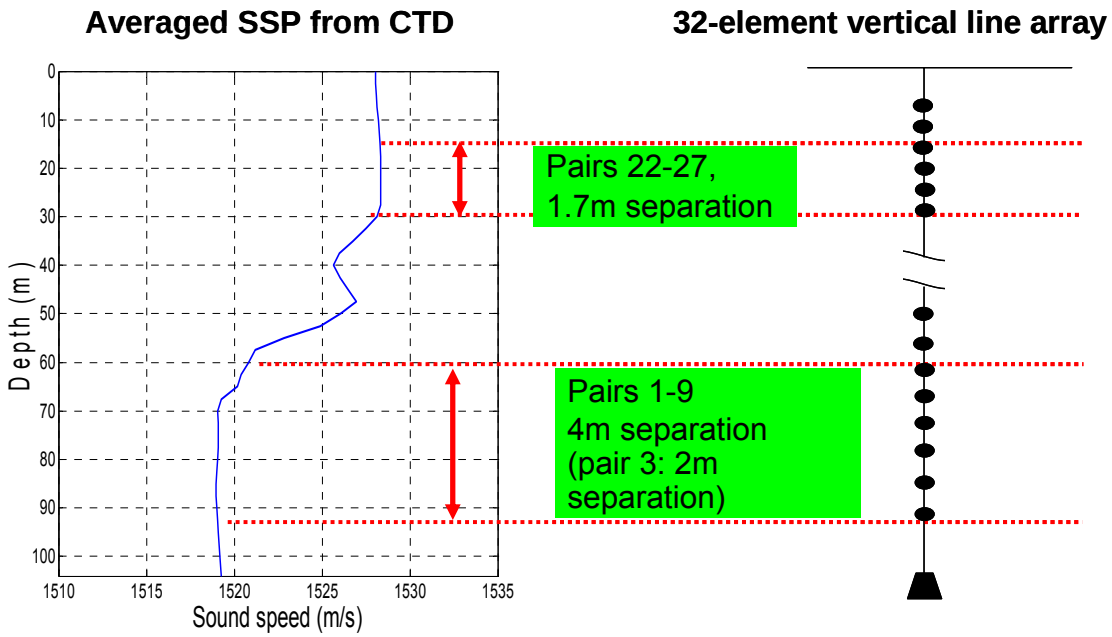

Figure 5.1 Hydrophone pairs used in the inversion and their depth information.

5.3 Inversion Results

Examples of the inversion results are plotted in Figures 5.2 and 5.3 for low and high frequencies. All plots show good agreement between model and data. The plots also indicate how to choose hydrophone separation in order to obtain sensible inversion results. As learnt from the characteristics of vertical coherence in Chapter 4, the best separation is between one and two wavelengths, usually referred to as the correlation length. The inversion results are computed using the hydrophone pairs that satisfy the previous statement. For example, for frequency range 300 to 800 Hz, a separation of 4m is chosen; while for frequencies higher, a separation of 1.7m is chosen.

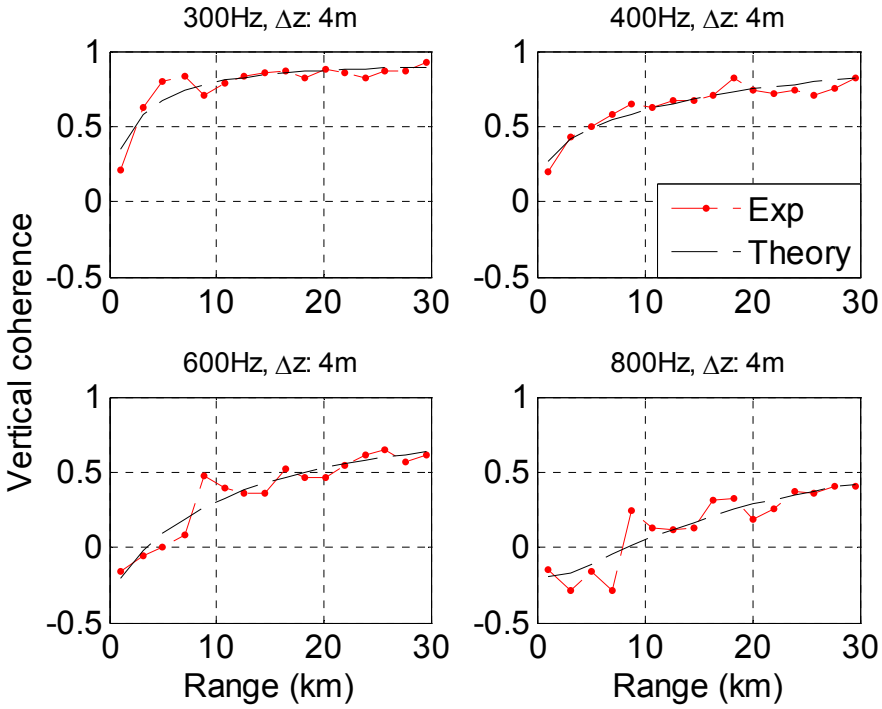

Figure 5.2 Sample data model comparisons using inverted parameters at low frequencies.

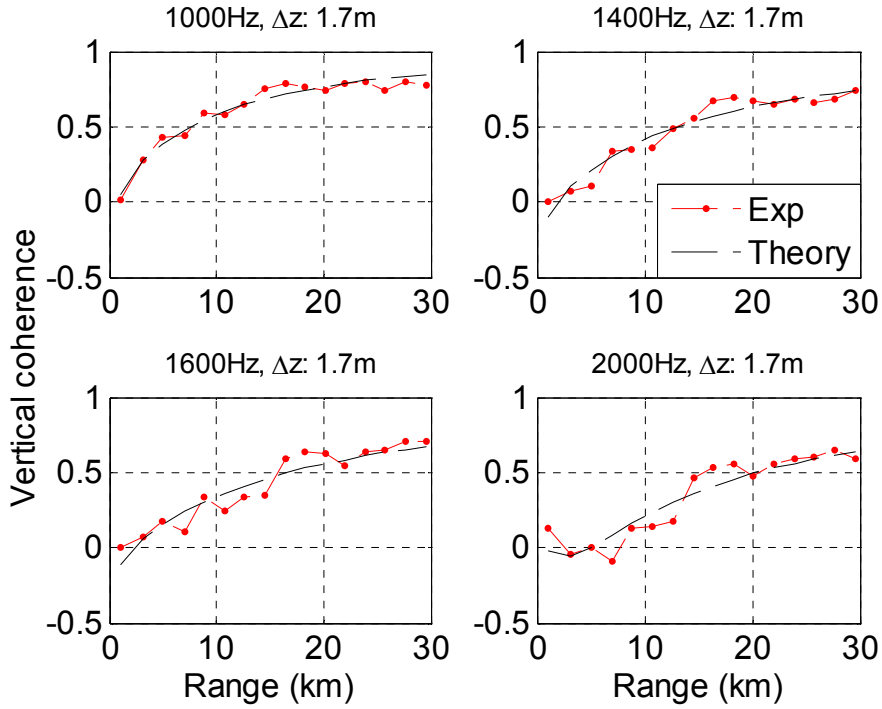

Figure 5.3 Sample data model comparisons using inverted parameters at high frequencies.

A good "dynamic" range of coherence, as shown in Figures 5.2 and 5.3, can help the sensitivity of the inversion scheme to the physical quantities. One issue here using the minimum error inversion scheme is the coupling issue between sediment sound speed and attenuation. The example chosen to show here is 4m separation pair at 70m at 300Hz in Figure 5.4. Three theoretical curves, one inverted and two tests, are compared with the experimental. All three curves fit the experimental quite well and the squared errors differ by approximately 11%. The coupling is that as one of the sediment properties C_b or α increases/decreases, the other will do the same as seen here. This is due to the fact that C_b and α have opposite effects on vertical coherence. By increasing C_b, the total number of modes will increase which will decorrelate the signal; by increasing α, the attenuation of each mode will increase and hence show a better coherence. The balance effects between C_b and α decide the final inversion results.

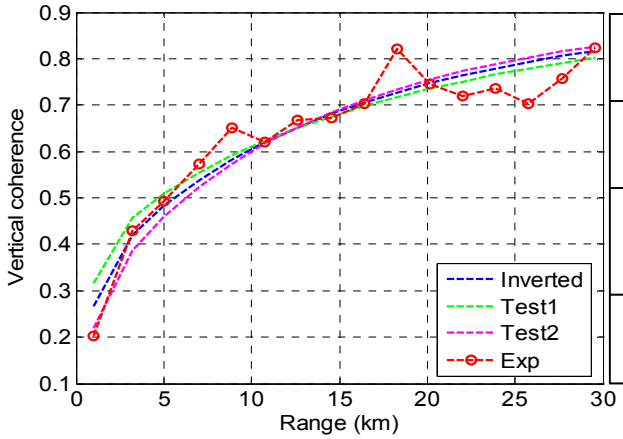

Cases (300Hz)	Cb (m/s)	α (dB/m)	Squared error
Test 1	1609	0.036	0.038
Inverted results	1622	0.048	0.034
Test 2	1638	0.060	0.038

Figure 5.4 Coupling effects of C_b and α from the inversion method.

The inverted sediment sound speeds and attenuations are computed for different frequencies and plotted in Figures 5.5 and 5.6. The inverted sediment sound speeds have considerable scatter around their mean values at each frequency. Since each inverted

value is from matching one pair of hydrophones with theory, the acoustic data have a lot of fluctuations. These fluctuations include fluctuations in the original SUS charge signal which may not be deployed at exactly the same depth and the bubble pulse may not collapse at the same depth, signal-to-noise ratio at long ranges, variability of the ocean environment, etc. The results could be improved if there were more signals deployed at every range. Then, their averaged results should have much less deviation. The overall averaged sound speed is 1645.9 m/s with standard deviation 22.8 m/s if using the averaged sound speed at each frequency.

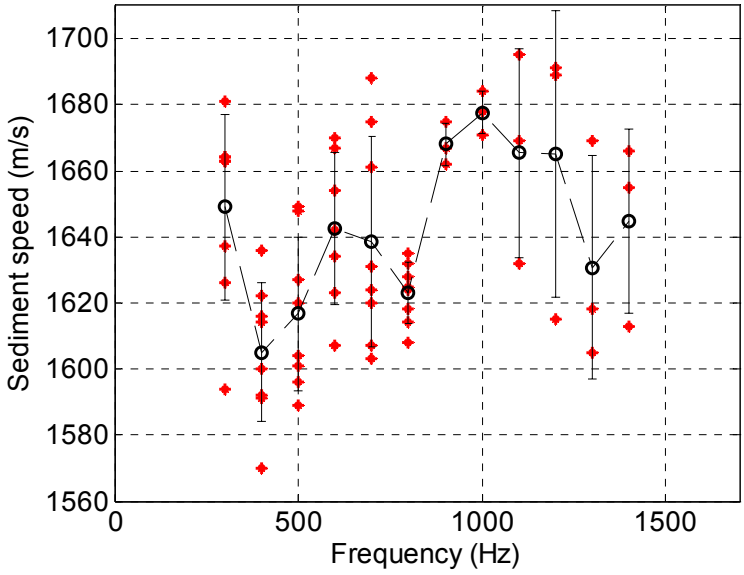

Figure 5.5 Inverted sediment sound speeds as a function of frequency.

As mentioned in the previous session, the sediment attenuation is usually written as a power law: $\alpha = \kappa f^n$. Based on the inversion results, the curve fitting results here is: $\alpha = 0.18 * f^{1.25}$. The power *n*, is smaller than results from Zhou et al (2004, 2007) but still in a reasonable range. The effective bottom loss can be calculated using sediment sound speed and attenuation (Zhou et al, 2007):

$$Q_{eff} = \frac{0.0366(c_1^2/c_2)(\rho_2/\rho_1)}{\left[1-(c_1/c_2)^2\right]^{3/2}} \kappa f^{(n-1)} \tag{5.7}$$

where c_1 and c_2 are in km/s, κ is the attenuation coefficient, f is in kHz, n is the power found from Figure 5.6, i.e. n = 1.25. The weak frequency dependence shown in Figure 5.7 is from the $f^{(n-1)}$ term in eq. (5.7).

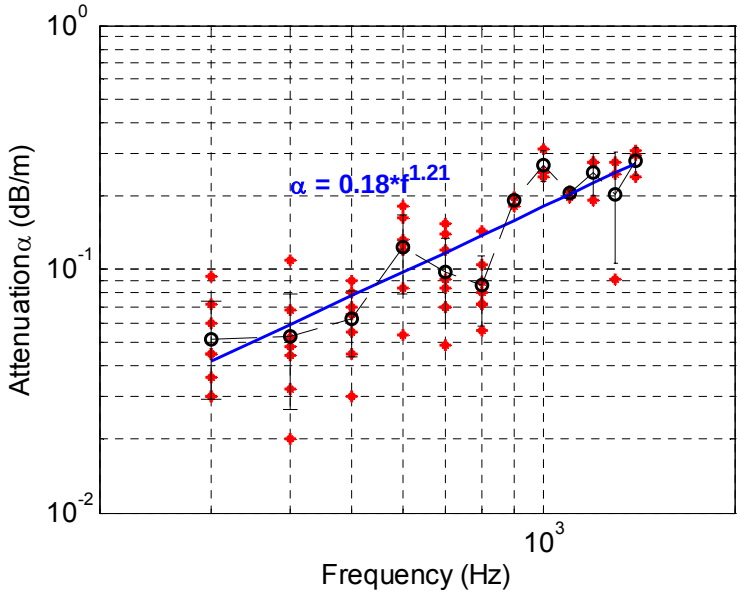

Figure 5.6 Inverted sediment attenuations as a function of frequency.

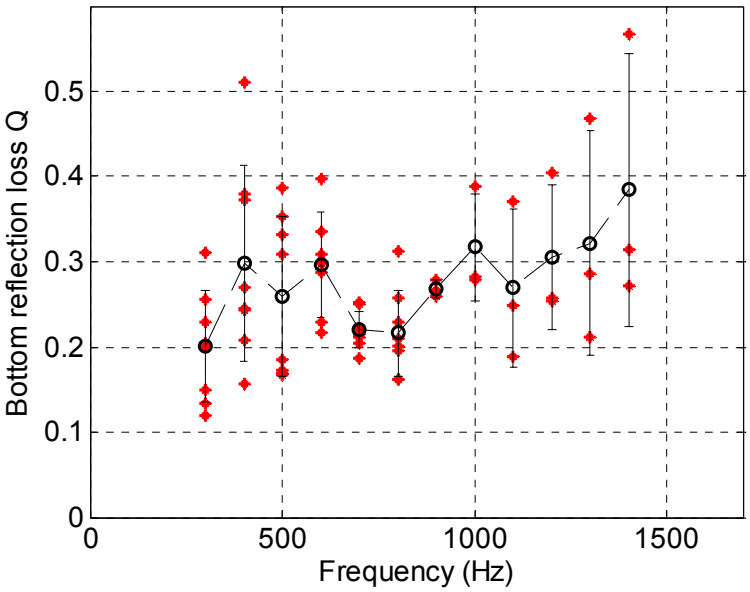

Figure 5.7 Effective bottom losses as a function of frequency.

After the ASIAEX, a lot of effort has been put into geoacoustic inversion using different techniques (IEEE JOE Special Issue for ASIAEX). A collection of the inverted sediment attenuation results can be found in Dahl et al (2004[1]). In Figure 5.8, the inverted sediment attenuations found in this thesis work are added to the collection from Dahl et al (in magenta). The inversion results are reasonably close to the results using different methods and they also exhibit weak non-linear frequency dependence.

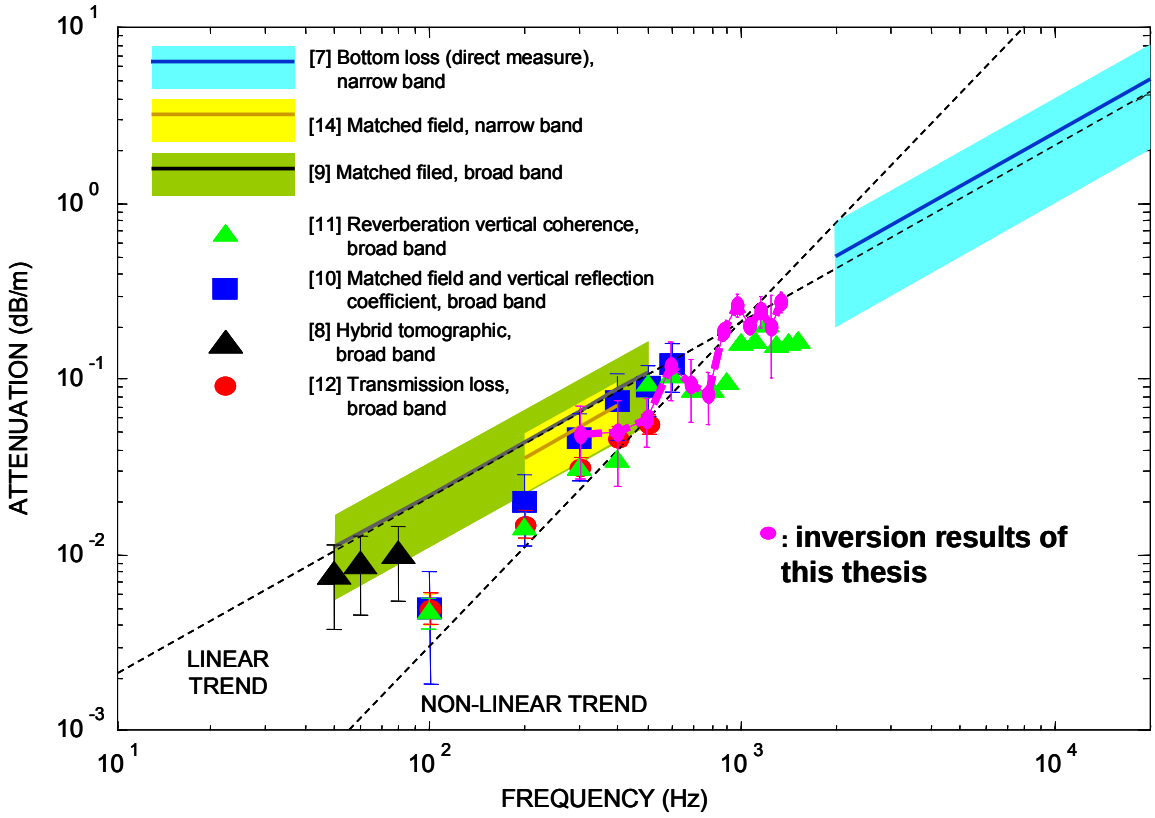

Figure 5.8 Comparison of inversion results with others at the ASIAEX (From: Overview of Results from the Asian Seas International Experiment in the East China Sea, P. H. Dahl, et al., IEEE J. Oceanic Eng. Special Issue on Asian Marginal Seas).

CHAPTER 6

ENVIRONMENTAL PARAMETER II:

INHOMOGENEITIES OF THE WATER COLUMN

6.1 Introduction

Inhomogeneities of the water column include internal gravity waves, coastal fronts, microstructure, eddies, and fish. These features can cause both temporal and spatial variations in temperature and salinity and hence in the sound speed distribution (Finette et al, 2000). One of the inhomogeneities that will be addressed here is the internal waves.

There are two types of internal waves: linear and nonlinear. The linear internal waves are produced by tidal currents and obey the wave equation:

$$\frac{d^2W(z)}{dz^2} + k_h^2\left[\frac{N^2(z)-\omega^2}{\omega^2-\omega_i^2}\right]W(z) = 0 \tag{6.1}$$

where $W(z)$ is the eigenfunction, k_h is the horizontal wavenumber or eigenvalue, N(z) is the buoyancy frequency, and ω_i is the inertia frequency. The buoyancy, or Brunt-Vaisälä (BV) frequency, can be calculated from the temperature and salinity data. It is defined as:

$$N^2(z) = -\frac{g}{\rho(z)}\frac{\partial\rho}{\partial z} \tag{6.2}$$

The relation between density, temperature, and salinity can be written as (Apel, 1987):

$$\frac{1}{\rho(z)}\frac{\partial\rho(z)}{\partial z} = -a_T\frac{\partial T(z)}{\partial z} + a_S\frac{\partial S(z)}{\partial z} \tag{6.3}$$

Here, a_T and a_S are the thermal expansion coefficient and the saline contraction coefficient respectively, with a_T = 2.41 $\times 10^{-4}(^{o}C)^{-1}$ and a_S = $7.45\times 10^{-4}(psu)^{-1}$. a_T and a_S are found for T = 20 ^{o}C and S = 35 *psu*. The BV frequency is shown in Figure 6.1, based on an average of 54 CTD profiles. It has peak values between 30 and 70 m in depth, corresponding to the region of the largest change in temperature and salinity.

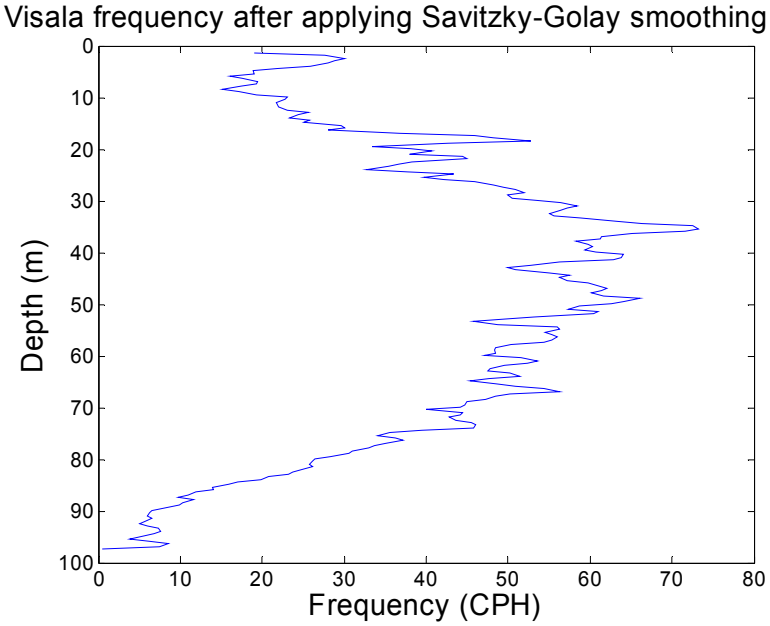

Figure 6.1 Average buoyancy frequency profile calculated from CTD data.

During ASIAEX, most internal wave activities recorded fell in this linear IW category. They are semidiurnal internal tides (internal waves at tidal frequency) and referred to as M_2. M_2 has a period of 12.42 hours and is usually generated by the tidal movement of density-stratified water over topography (Rattray et al, 1969; Baines, 1973 & 1974; Prinsenberg et al, 1974; Hsu et al, 2000; Kang et al, 2002). Observing the motion of the 19 ^{o}C, 20^{o}C and 21^{o}C isotherms, shown in Figure 6.2 for the entire period of measurement, a rough 12-h cycle can be seen.

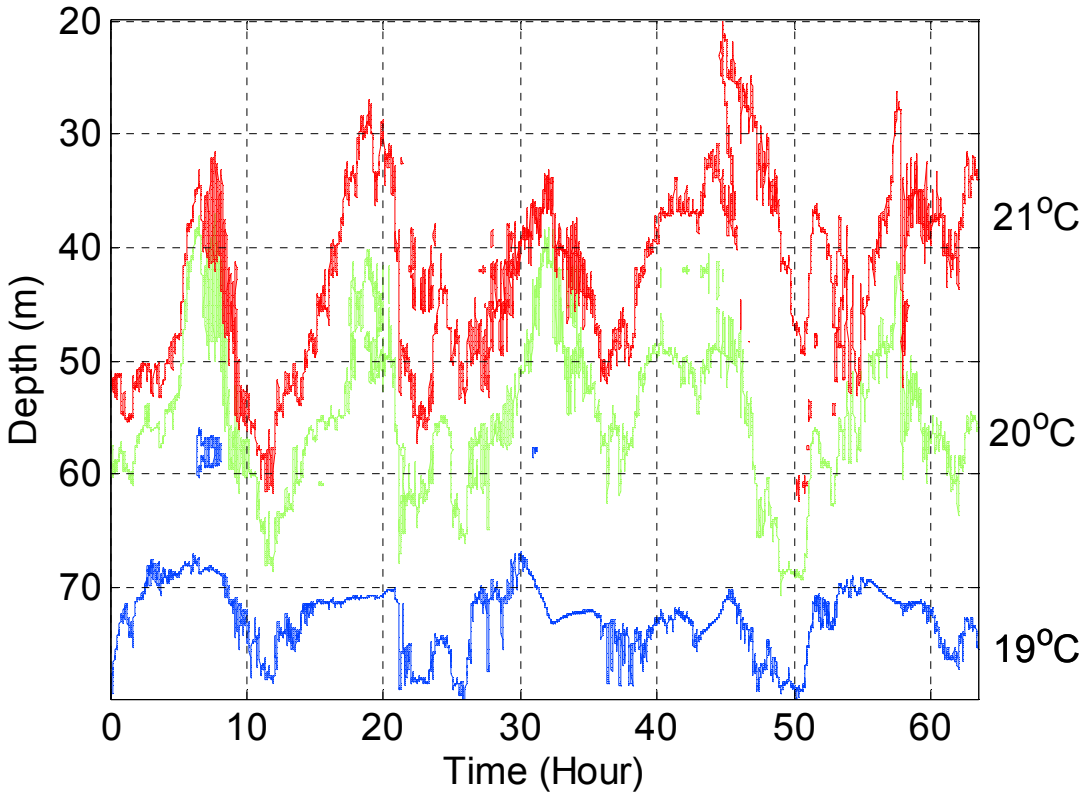

Figure 6.2 Isotherms at temperature 19°C, 20°C, and 21°C from 08:40, June 3rd to 00:00, June 6th, 2001 at location 126°54.32'E, 29°24.01'N.

The nonlinear internal waves, known as solitons, are usually generated by nonlinear transformation as the internal tides propagate over the continental slope (Katsnelson et al., 2001). These high-amplitude nonlinear internal wave trains usually lasts about 3~4 hours and can cause strong acoustic scattering and hence, produce an anisotropic sound field. The soliton is a solution to the nonlinear Korteweg-de Vries (KdV) equation:

$$A_t + C_0 A_x + \alpha A A_x + \gamma A_{xxx} = 0 \tag{6.4}$$

with solution:

$$A(x,t) = -A_0 \sec h^2\left(\frac{x - Ct}{L}\right) \tag{6.5}$$

Here, A is a wave amplitude function, C_0 is the linear wave speed, α and γ are the nonlinear and dispersion parameters respectively. In the solution, A_0 is the amplitude factor, L is the characteristic width of the soliton and C is the amplitude-dependent wave speed.

There is another analytic solution to the KdV equation which is called cnoidal waves (Rubinstein, 1999). The solution can be written as:

$$A(x,t) = A_0 + A_1 cn^2\left[k(x-ct); m\right] \tag{6.6}$$

cn(x;m) in eq. (6.6) is the Jacobian elliptic function and m is the modulus. We believe the HF internal waves (Figure 2.8) in ASIAEX belong to the cnoidal form, appearing as highly periodic and nondispersive (Figures 2.8 and 6.2).

6.2 Characteristics of Internal Gravity Waves

6.2.1 Vertical Displacements of Internal Waves

In order to calculate the acoustic effects of internal waves, one needs first to find the temporal and spatial sound speed fluctuations due to the internal waves. This can be done by studying the vertical displacements of the internal waves, i.e. the vertical displacements of the isopycnal surfaces, which can be found using temperature/salinity recordings. From the simple relation: $\delta C = \frac{\partial C_p}{\partial z}\xi$, the sound speed fluctuation δC is the product of the local vertical displacement and the sound speed gradient. The sound speed variation due to linear and nonlinear internal waves can be determined separately (Tielburger et al., 1997; Finette et al., 2000).

Temperature fluctuations are often regarded as proxies for the vertical displacement induced by internal waves (Holloway, 1984; Dewitt et al, 1986; Colosi et

al, 2001). As in eq. (6.3), temperature is usually the dominant factor over salinity, and if we neglect the salinity term and take the Fourier transform of (6.3), the spectra of the isotherms and the isopycnal surfaces should be identical at a given depth. Based on our CTD and thermistor data, we found that the $-a_T \frac{\partial T(z)}{\partial z}$ term is about an order of magnitude bigger (averaged over the water column) than the $a_S \frac{\partial S(z)}{\partial z}$ term in Eq. (6.3). In this situation, we can reasonably neglect the salinity term, incurring at worst a 10% error. In any case, we do not have a time series of salinity at various depths (just intermittent CTD casts), so that we could not obtain a continuous record of the isopycnal displacement contribution due to the salinity term.

The vertical displacement of the isopycnal surface has a simple relation with temperature (Apel et al, 1997):

$$\eta(t) = \frac{T^*}{[\partial T / \partial z]} \tag{6.7}$$

where $\eta(t)$ is the time series of vertical displacement, T^* is the internal wave-induced temperature fluctuation, and $[\partial T / \partial z]$ is the averaged "background" temperature gradient at the thermistor depth with IW filtered out beforehand.

Instead of using (6.7) to directly calculate the vertical displacement, we adopt an "inverse mapping" method to convert temperature to vertical displacements (Lynch et al, 1996; Apel et al, 1997; Rubenstein, 1999). Provided that the horizontal change in temperature is small, a given time series of thermistor data $T_i(z,t)$ can be related to the mean temperature field by:

$$T_i(z,t) = T_m(z_i + \eta(t)) \tag{6.8}.$$

Here, z_i is the depth of the thermistor and $\eta(t)$ is the time series of vertical displacement with respect to the "equilibrium" state. Mapping $T_i(z,t)$ to the mean temperature field T_m (by interpolation), we can find the vertical displacement $\eta(t)$. (There is no displacement for thermistors 1-6, 16, and 17 due to the fact that there is no interpolation.) We have converted the temperature records from thermistors No. 7, 8, 11, 12 and 15 to their vertical displacements. The resultant time series of vertical displacement for 63 hours is shown in Figure 6.3. Peak-to-peak vertical displacements due to the semidiurnal tides are about 15-30 m according to these selected thermistors. The curves displayed are plotted according to the thermistors' depths.

Next, we discuss the high frequency oscillation characteristics. The vertical displacements of the high frequency oscillation are obtained by high-pass filtering the previous vertical displacement data. To better compare the oscillation amplitudes, we plot the data from thermistors of No. 7, 8, 11, and 12 together in Figure 6.4. Amplitudes are seen to be decreasing with increasing depth from No. 7 to No. 12. The maximum peak-to-peak amplitude seen from thermistor No. 7 is about 20 m. It is apparent from Figure 6.4 that the high frequency IW's are quasi harmonic, with a period around 5-6 cph. The high frequency oscillations last about 3 hours each occurrence and recur at almost the same time each day. This strongly suggests that the HF IW's are associated with tidal forcing (Halpern, 1971). Using the wave speed of mode one (Flatté, et al, 1979), the wavelength of HF internal waves estimated is between 130-200 m.

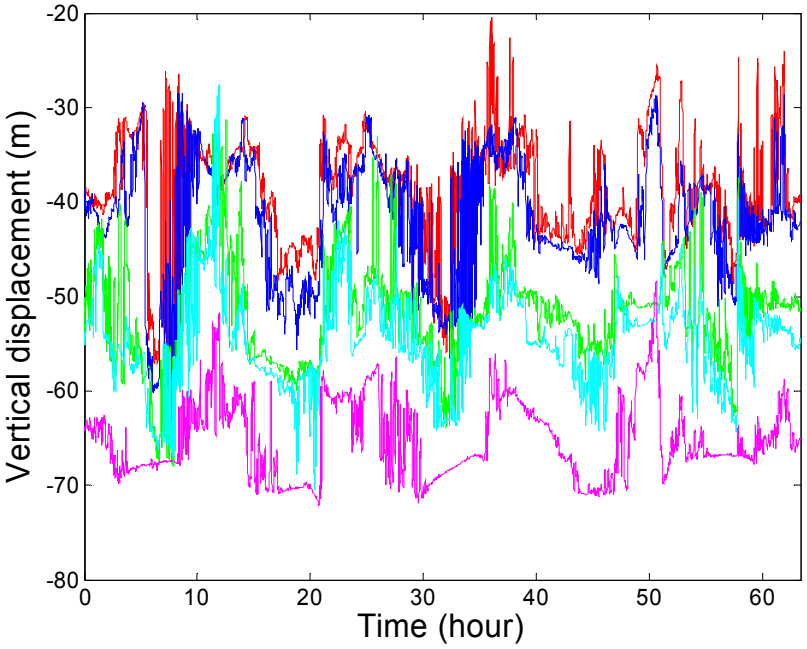

Figure 6.3 Time series of vertical displacement obtained from thermistors of No.7, 8, 11, 12 and 15 at depths 38.9, 42, 51.5, 54.6, and 65 m.

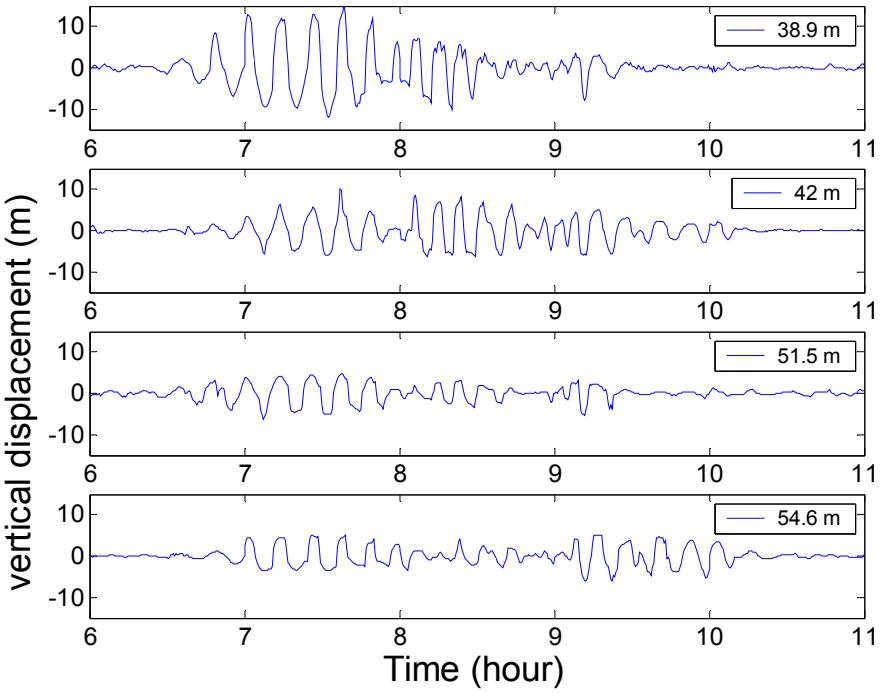

Figure 6.4 Vertical displacements measured by thermistors No. 7, 8, 11 and 12 at the depths listed, showing high frequency internal waves.

6.2.2 Shallow Water Internal Wave Spectrum

The internal wave spectrum is the spectrum of the vertical displacement of the isopycnal surfaces. As the vertical displacement is a function of depth, the IW power spectrum will depend on depth, too. From the 63-h data, we selected two extreme cases for which to examine IW spectra: one with maximum IW amplitudes (from thermistor #7, at depth 38.9m) and the other with minimum IW amplitudes (from thermistor #15, at depth 65m). The results are shown in Figures 6.5 and 6.6 respectively. In Figure 6.5, the spectral slope β for the IW frequency band of 0.1-4 cph is about -1.7, less than GM' -2, but in close agreement with the shallow water results of Apel et al (1997) and Colosi et al (2001). Also, one notices a peak due to non-linear internal waves at a frequency of 5-6 cph. This again agrees with the previously cited works. In the higher frequency band (beyond 6 cph, the highest BV frequency), the spectral slope is about -2.9; in this region, one is seeing ocean fine structure and turbulence effects, before losing the spectrum to instrumental noise and temporal undersampling. Figure 6.6 shows the results from the deepest thermistor, #15. The shape of the IW spectrum is basically similar to the one from thermistor #7, except that the HF IW peak has been reduced to a milder plateau at around 4-6 cph. The higher frequency band (above the internal wave band) shows a spectral slope of -2.6, close to the -2.9 observed before. The above analysis has been repeated for other depths (thermistors). The results from nine thermistors with different depths are summarized in Table I. The average spectral slope of vertical displacement for the frequency band 0.1-04 cph is -1.6; for the higher frequency (>6 cph) fine structure and turbulence band, it is –3.0.

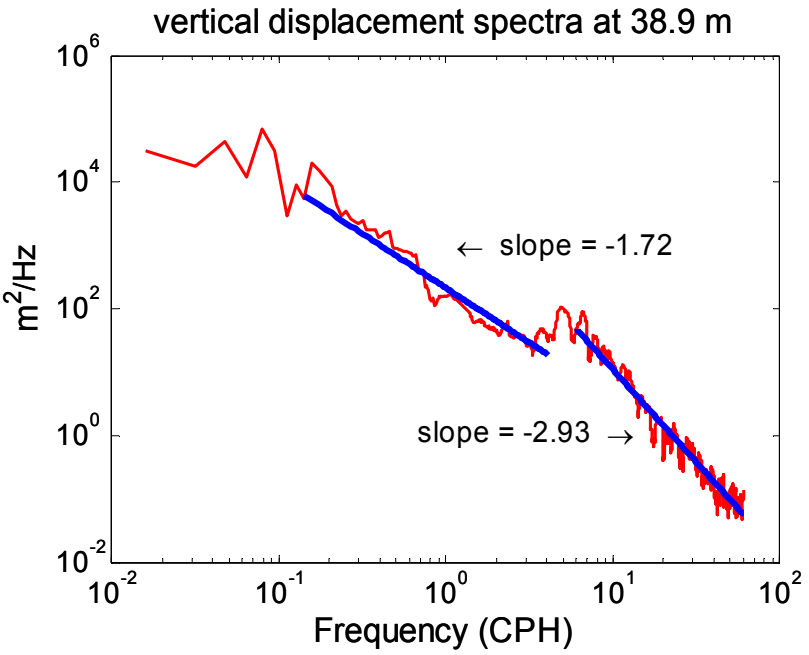

Figure 6.5 Vertical displacement spectrum from thermistor #7, the depth with maximum internal wave amplitude. Spectral slope is β = -1.7 in the frequency range 0.1-4 cph; β = -2.9 for frequencies higher than 6 cph.

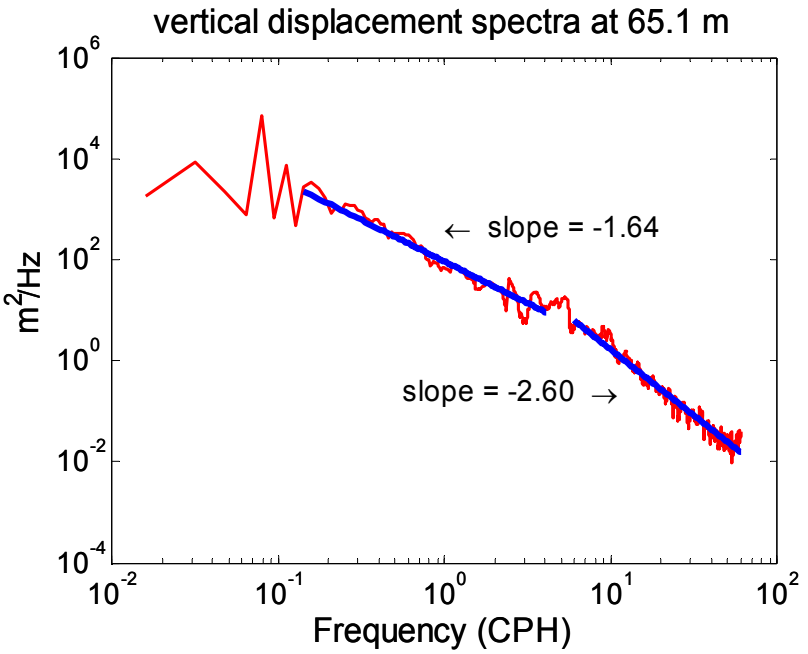

Figure 6.6 Vertical displacement spectra from thermistor #15, at a depth with minimum internal wave amplitude. Spectral slopes in the frequency ranges 0.1-4 cph and beyond 6 cph are -1.6 and -2.6 respectively.

Table 6.1 Internal Wave Spectral Slope Estimates

Depth	38.9	42	45.2	48.3	51.5	54.6	57.8	60.9	65.1	Avg.
Decay rate range 1	-1.7	-1.7	-1.8	-1.4	-1.4	-1.6	-1.5	-1.6	-1.6	-1.6
Decay rate range 2	-2.9	-3.1	-3.1	-2.8	-3.0	-3.2	-3.4	-2.9	-2.6	-3.0
Range 1 corresponds to frequency range 0.1-4 cph and range 2 is for frequency above 6 cph.										

The internal wave spectrum model was first proposed for the deep ocean which were described as stationary and isotropic. The internal wave spectrum in the deep sea is well presented by the modified Garret Munk (GM) model (Garret & Munk, 1972, 1975; Cairns & Williams, 1976). The GM model proposed a spectrum:

$$P_j(\omega) = E_0 \frac{\left(j^2 + j_*^2\right)^{-p}}{\sum_j \left(j^2 + j_*^2\right)^{-p}} \frac{4}{\pi} \omega_i \frac{\left(\omega^2 - \omega_i^2\right)^{1/2}}{\omega^3} \tag{6.9}$$

Here, j is the internal wave mode number, ω_i is the inertia frequency, E_0 is the average energy density of the internal waves, j_* and p are parameters chosen to fit the spectrum observed (chosen as 3 and 2 respectively). The GM model predicts the internal wave spectrum will decrease as ω^{-2} (slope -2 if plotted logarithmically).

Recent studies of internal waves in the coastal zone show many different characteristics compared with the deep water case (Lynch et al., 1996; Apel et al., 1997). The coexistence of two types of internal waves makes the internal wave spectrum a lot different than in deep water. First of all, the slope is usually smaller than 2 as seen in Figure 6.7 observed from the ASIAEX (Apel et al., 1997; J. Yang et al., 2004). Second,

the shallow water internal wave spectrum commonly has a plateau in the high frequency range (due to the nonlinear waves) which is highlighted in Figure 6.7. It is apparent that most energy concentrates around the semidiurnal tidal frequency.

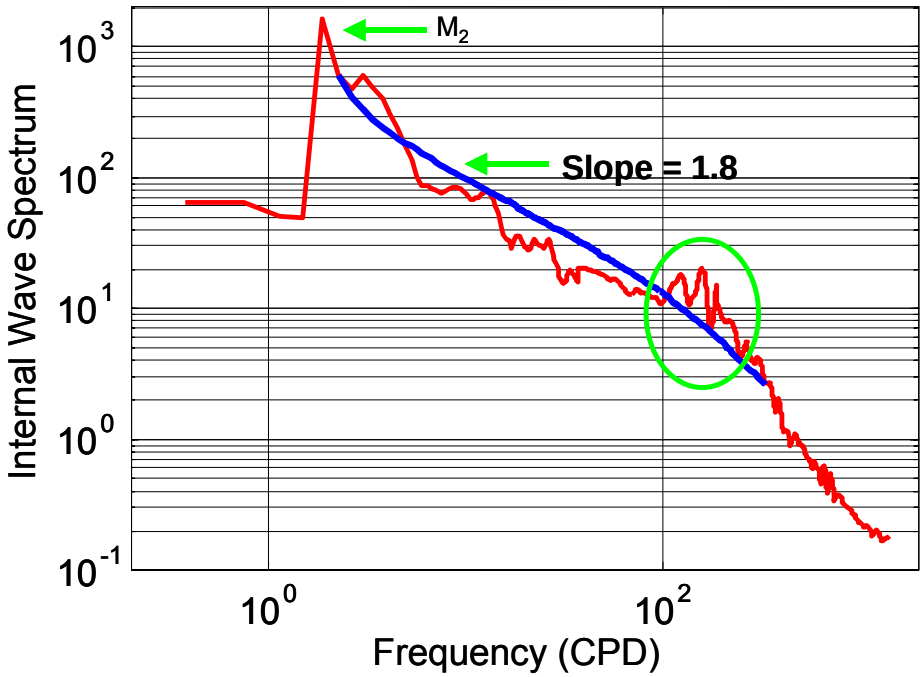

Figure 6.7 Internal wave spectra recorded in the ECS in 2001.

6.2.3 Vertical Coherence of Internal Waves

The vertical coherence of the internal waves is now calculated versus frequency and thermistor separation. The temperature time series are filtered at the center frequency of interest, in a 1/3 octave band. Here, we choose the two extremes of the IW frequency band as cases of interest, i.e. the semidiurnal tidal frequency (0.08 cph) and the HF oscillation frequency (6 cph).

For the first case, a 28-hour segment of temperature data is used to calculate the time-lagged correlation coefficient, in order to satisfy the relation $\Delta t * \Delta f >> 1$. Figure 6.8

shows the normalized IW vertical correlation coefficient as a function of time and separation (specifically, the separation between thermistor # 6, located at the depth of 35.7m, and others at deeper depths). In general, the overall coherence level is high (above 80%). This suggests that the first normal mode dominates the IW field at the semidiurnal tidal frequency (0.08 cph). We can also see from Figure 6.8 that the coherence drops with increasing separation and longer times.

For the high frequency IW component, the same process was repeated but using a much smaller segment (3 hours) to calculate the time-lagged correlation coefficient. The vertical correlation coefficient of the HF IW is shown in Figure 6.9. It exhibits some interesting (though not unexpected) characteristics: (1) it is periodic, with an average peak period of about 12 hours; (2) it has shorter correlation radius, i.e., it decreases much faster than the LF IWs with increasing time delay; (3) sometimes there is a negative peak value, i.e., IWs at two different depths have 180^{o} phase difference. The first characteristic just shows the correlation of the high frequency waves to the semi-diurnal tide, a well-known result. The second characteristic seems to indicate that the high frequency internal wave field is more variable in its characteristics than the semi-diurnal internal tide, again not unexpected. The third characteristic might indicate the existence of a mode-two internal wave component, which one would expect to anti-correlate for two thermistors on the opposite sides of a turning point. As this anti-correlation seems to occur during times of low internal tidal energy, it also could be due to there being a change in the characteristics of the IW field between the high energy and low energy internal tidal periods, with the high energy periods seeing stronger, and sometimes non-linear IW's.

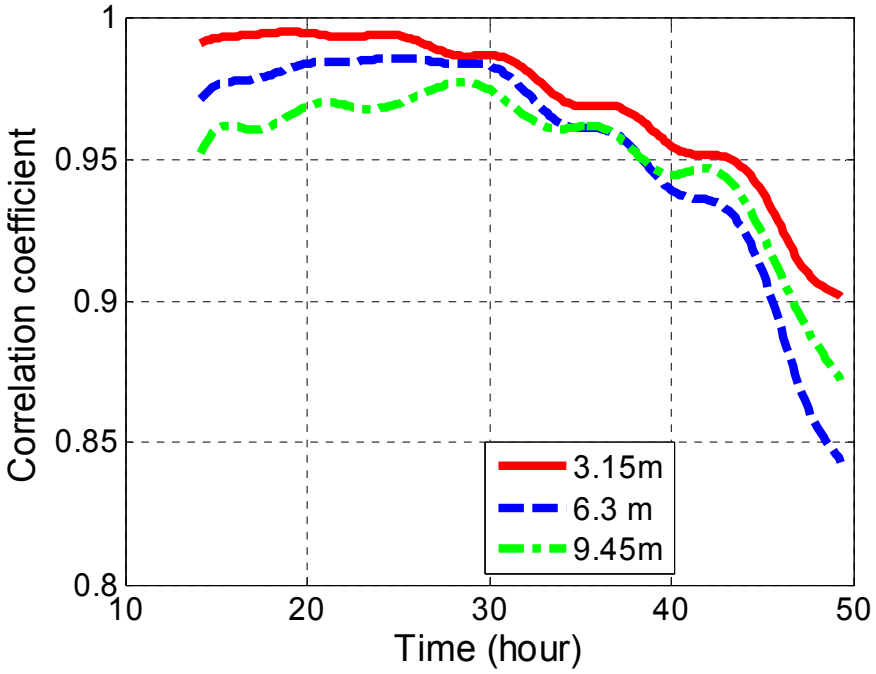

Figure 6.8 IW vertical coherence at the semidiurnal tidal frequency (1.92 cpd). Solid line: 3.15 m separation; dashed line: 6.3 m separation; dash-dot line: 9.45 m separation.

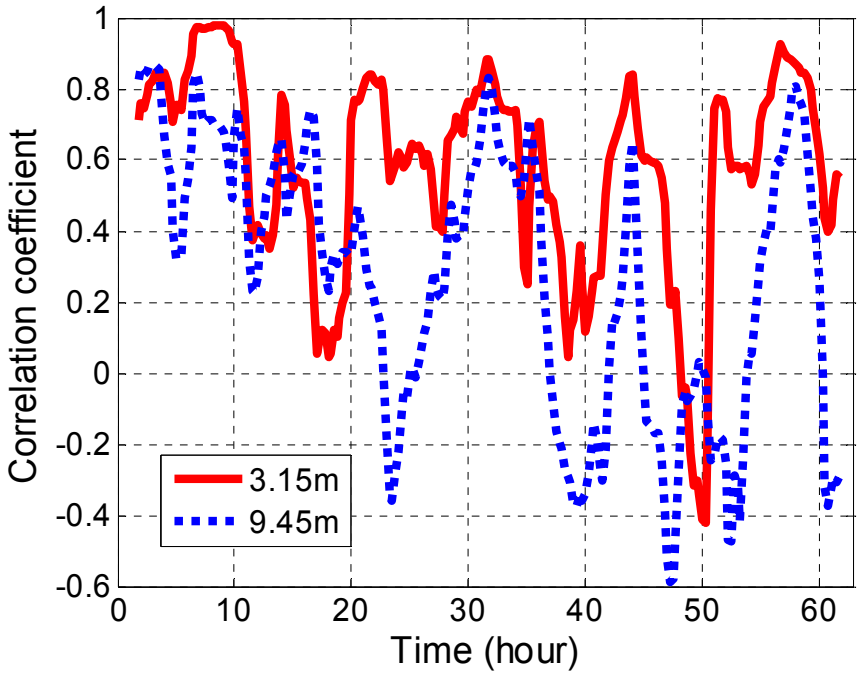

Figure 6.9 IW vertical coherence at the frequency of 6 cph. Solid line: 3.15 m separation; dashed line: 6.3 m separation.

6.2.4 Common Characteristics of Shallow Water Internal Waves

The characteristics of IW's in the coastal zone have not been well measured compared to the lower frequency oceanography, which had been generally of more interest to the physical oceanographic community in the past. However, in the recent decade several good measurements of shallow water IWs at different locations have been reported. In order to infer some common characteristics for shallow water IWs, we will compare our ASIAEX observations in the ECS with observations in the Barents Sea, the Mid-Atlantic Bight, and the Gulf of Mexico (Lynch et al, 1996; Apel et al, 1997; Rubenstein, 1999). The current observations and the cited previous observations, along with their locations, dates, and measurement types are listed in Table II.

Table 6.2 Location, Date and Type of Previous *In Situ* IW Experiments

Site	Time	GPS location	Data type
(A) Barents Sea	Aug. 1992	74^{o}N, 22^{o}E	CTD and thermistor
(B) Mid-Atlantic Bight (SWARM)	July-Aug., 1995	39^{o}N, 73^{o}W	CTD, thermistor, and current
(C) Gulf of Mexico	Nov. 1995	28^{o}N, 85^{o}W	Thermistor array
(D) ECS	June 2001	29^{o}N, 126^{o}E	CTD, thermistor

6.2.4.1 Observations of LF and HF IWs – Wave Type and Amplitude

For the measurements in Table II, the measured temperature data have been converted into vertical displacements of the isopycnal surfaces, which represent the amplitude of the internal waves. Amongst the four experiments, long-wavelength, linear, M2 internal tides were observed in A, B, and D. Experiments B, C, and D showed high frequency oscillations riding on top of the low-frequency internal tides. Experiment B

clearly showed trains of solitons with maximum crest-to-trough amplitude of 12 meters. Experiment C displayed nonlinear cnoidal waves with peak-to-peak amplitude 10 meters. In our case, the amplitude of the M2 internal tide was about 15-30 m and the high frequency oscillation amplitude was up to 20 m.

6.2.4.2 IW Spectral Characteristics

The HF peak or plateau is an interesting feature seen in many shallow water internal wave spectra. Experiments B, C, and D all showed some peaks at high frequency in the spectra, due to nonlinear waves. The spectral slopes estimated from A, B, and D are quite close, even though the latitudes are significantly different. Their numerical value is also intriguingly close to the -5/3 one sees in turbulence spectra. The explanation for commonly seen shallow water spectral slope presents an interesting challenge to the physical oceanography community.

6.2.4.3 HF IW Wave Taxonomy for the ECS Site

The nature of the high frequency IW oscillations seen in the ECS data is of particular interest to us. Wave trains such as the one seen in Figure 2.8 stand out clearly in the data record, and immediately suggest nonlinear waves. However, these waves have a rather sinusoidal form, and moreover calculations by Ramp (private communication) indicate that the nonlinear parameter is small for these waves. However, both these observations are consistent with cnoidal nonlinear waves, which asymptotically become sinusoidal in the limit of a small nonlinear parameter. These waves also appear at the same internal tidal phase, and last over a roughly constant period of three hours. This is again consistent with the tidal forcing of a nonlinear wave. Thus, we will tentatively identify these waves as cnoidal waves.

6.3 Acoustical Effects of Internal Waves

6.3.1 Internal Wave Spectrum Model

To quantify acoustical effects of internal waves, it is necessary to first find the sound speed fluctuations induced by the internal waves. As mentioned in section 6.1, temperature and salinity fluctuations can often be regarded as proxies for the vertical displacement of the internal waves. As a result, we can relate sound speed fluctuations with the internal wave displacements.

Vertical displacements can be written as an expansion of the internal wave eigenmodes calculated from eq.(6.1):

$$\zeta(r,z,t) \;=\; \sum_{j=1}^{N}\int_{-\infty}^{+\infty} A_j(k)W_j(k,z)\exp[ikr + i\omega_j(k)t]dk \tag{6.10}$$

Here, $W_j(k,z)$ is the j^{th} internal wave eigenmode. The expansion coefficients $A_j(k)$ are zero mean, complex Gaussian random variables with variance given by the modified GM spectrum (6.9) , whose general form is repeated as below:

$$P_j(\omega) = E_o \frac{(j^2 + j_*^2)^{-l}}{\sum_{j=1}^{\infty}(j^2 + j_*^2)^{-l}} \frac{2}{\pi} \frac{(\omega^2 - \omega_i^2)^s}{\omega^{2s+p}} \tag{6.11}$$

There are four parameters in this model: j_*, l, s and p which can vary from location to location. Since the IW spectrum was actually recorded, curve fitting scheme was used to find the particular set of parameters for the ASIAEX site. The results, shown in Figure 6.10, are $j_* = 1$, $l = 4$, $p = 1.8$, and $s = 0.5$.

In order to find the expansion coefficient in (6.10), the GM spectrum needs to be converted to the wavenumber domain using the dispersion relation (Yang et al, 1999):

$$k = k_j \sqrt{\omega^2 - \omega_i^2} \,/\, \omega_i \tag{6.12}$$

here $k_j = \pi j \omega_i \Big/ \int_0^H N(z)dz$. Again, ω_i is the inertia frequency and *N(z)* is the buoyancy frequency. The GM spectrum can be transformed from frequency to wavenumber domain following:

$$P_j(k) = P_j(\omega) d\omega \Big/ dk \tag{6.13}$$

From the dispersion relation, it can be found that $\frac{d\omega}{dk} = \frac{\omega_i k}{k_j \sqrt{k_j^2 + k^2}}$. Therefore, equation (6.11) is then:

$$P_j(k) = E_o \frac{(j^2 + j_*^2)^{-l}}{\sum_{j=1}^{\infty} (j^2 + j_*^2)^{-l}} \frac{2}{\pi} \left(\frac{k_j}{\omega_i} \right)^{p-1} \frac{k^{1+2s}}{\left(k_j^2 + k^2\right)^{s+(p+1)/2}} \tag{6.14}$$

For a deep water case ($p = 2$, $s = 0.5$), (6.14) is reduced to the GM form (6.9).

With (6.14), the expansion coefficient $A_j(k)$ can be readily generated as a zeros mean Gaussian random number with variance:

$$\left\langle A_j(k)^2 \right\rangle = P_j(k) = E_o \frac{(j^2 + j_*^2)^{-l}}{\sum_{j=1}^{\infty} (j^2 + j_*^2)^{-l}} \frac{2}{\pi} \left(\frac{k_j}{\omega_i} \right)^{p-1} \frac{k^{1+2s}}{\left(k_j^2 + k^2\right)^{s+(p+1)/2}} \tag{6.15}$$

Now the vertical displacement (6.10) can be calculated and then converted to sound speed fluctuations using the relation:

$$\delta c(r,z,t) \;\cong\; (dc_p / dz)\zeta(r,z,t) \tag{6.16}$$

dc_p / dz is the potential sound speed gradient and can be computed from temperature and salinity data:

$$\frac{dc_p}{dz} = \frac{\partial c}{\partial T}\left(\frac{dT}{dz} - \frac{dT_a}{dz}\right) + \frac{\partial c}{\partial S}\frac{dS}{dz} \tag{6.17}$$

where T_a is the atmospheric temperature.

The range dependent sound speed field can be decomposed into:

$$c(r,z,t) = c_{mean}(z) + \delta c(r,z,t) \tag{6.18}$$

c_{mean} is the averaged sound speed profile. The total sound speed field is used as an input to a range dependent acoustic model to give predictions of acoustic effects induced by internal waves. The randomness of the internal waves are preserved in the changing sound speed field $\delta c(r,z,t)$. The range dependent acoustic model reads a sound speed field (6.18) as a result of one realization using the internal wave spectrum.

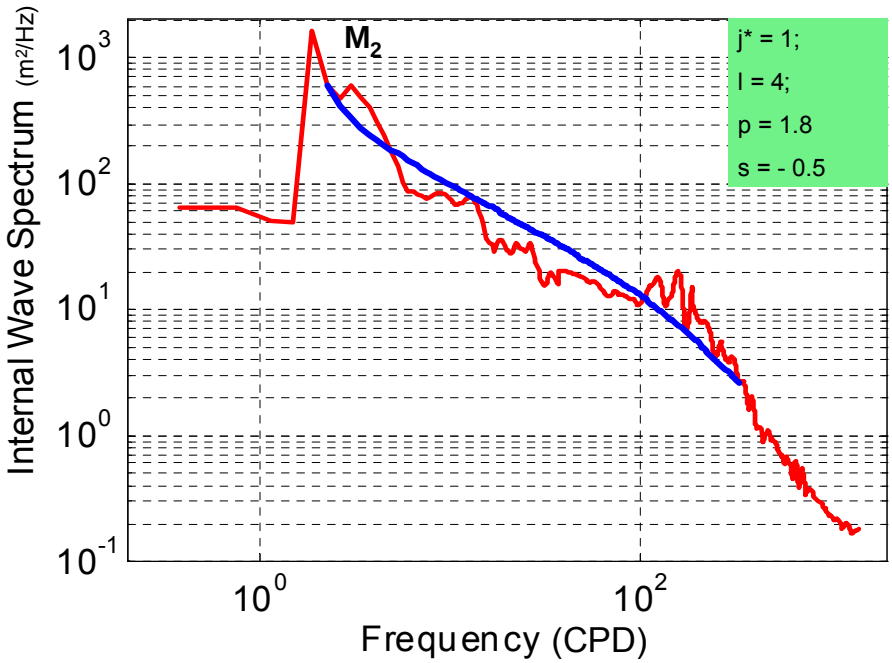

Figure 6.10 Curve fitting IW spectrum at ASIAEX with GM model.

As addressed in Chapter 4, the abnormal observations of vertical coherence in FM direction around 20km (see Figures 4.7-4.9) may be due to the interactions with the

internal waves. Using the ASIAEX IW spectrum (Figures 2.10 and 6.10), the acoustical effects may come from the interaction with both types of internal waves: one is the long wavelength internal tides and the other is the localized high frequency wave packets. The sample predictions of the acoustic models using the internal wave spectrum are shown in Figures 6.11 and 6.12. It is quite clear that simulations do not catch the changes of the coherence curves around 20km. There are several reasons to account for this.

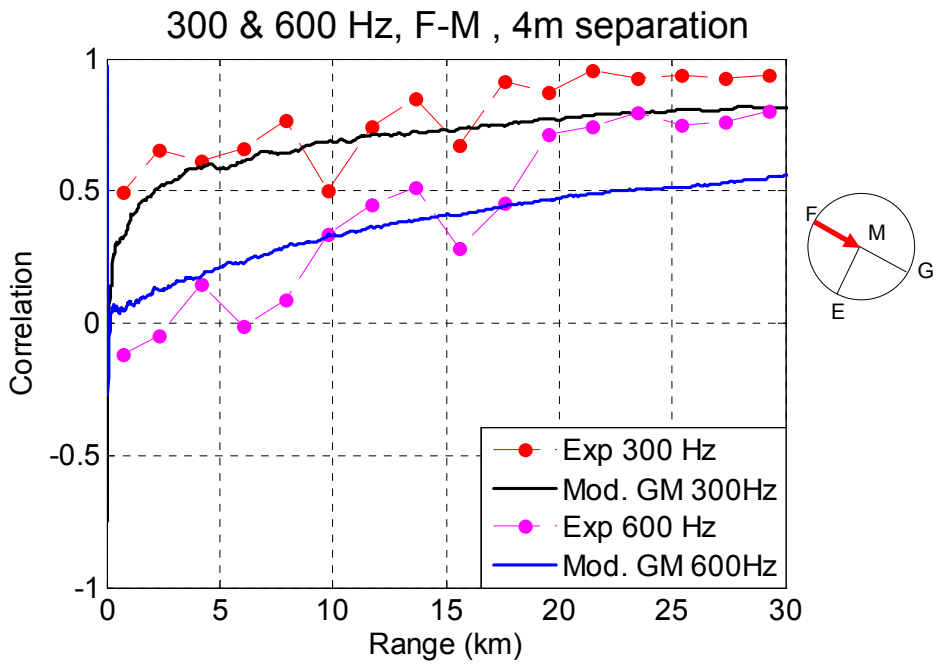

Figure 6.11 Data/model comparison using the modified GM spectrum at 300 and 600Hz. Sediment sound speed and attenuation used: 1615 m/s and 0.2 dB/m*kHz.

The most direct reason is that the internal wave spectrum does not contain time information. In another word, the sound speed field generated from the internal wave spectrum satisfies the energy content at each frequency but most likely differs from the real sound speed field as the data were taken. Provided that sound propagation depends heavily on sound speed profile, the predictions may show considerable discrepancies from the experimental. Another reason is that the above procedure has evenly distributed

the spectral content/energy into space. As shown in Figure 6.10, the energy at M_2, the semidiurnal tidal frequency, is of about 2 magnitudes higher than the high frequency oscillations (6cph). These high frequency oscillations might be the reason to cause the changes in coherence. They, however, seems to be overpowered by the M_2. The observed acoustic data may be due to the long wavelength M_2, or the high frequency wave packets, or the combination of the two.

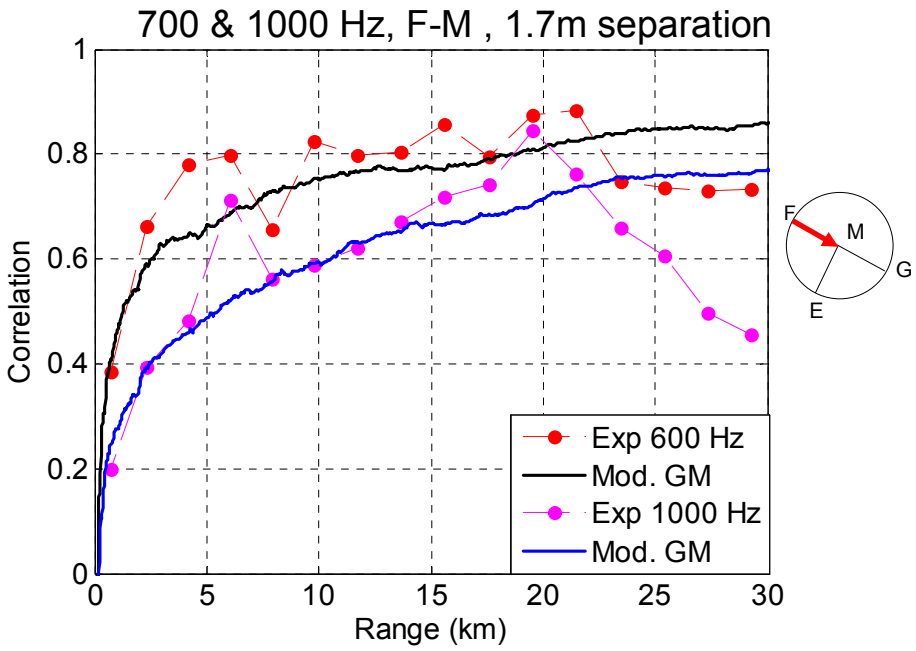

Figure 6.12 Data/model comparison using the modified GM spectrum at 600 and 1000Hz. (Same sediment properties as Figure 6.11.)

6.3.2 Alternative Range Dependent Acoustic Model

During ASIAEX, there was no towed CTD data taken simultaneously with the acoustic data. All we have are the 63-h thermistor recordings and intermittent CTDs at the mooring location M. In order to study the "real-time" internal wave effects, we need to make use of the 63-h temperature data.

In general, internal waves are generated as tides move across the shelf break, which is, in ASIAEX case, from M to F. In addition, the internal waves usually move at about 0.6m/s. To verify this IW speed, the CTD results from the ASIAEX were used to calculate the group speeds for different modes using the IW equation (6.1). The group speeds as a function of frequency are shown in Figure 6.13 for the first five modes. Internal waves in shallow water are usually dominated by mode one (Yang, et al, 2004[2]). For the internal tides (period close to 2 cpd), its group speed is close to 0.6 m/s. The HF IWs moves at 0.71 m/s which was calculated from the KdV equation (6.4). The difference in the group speeds of the two IWs makes negligible discrepancy in the propagated sound speed field.

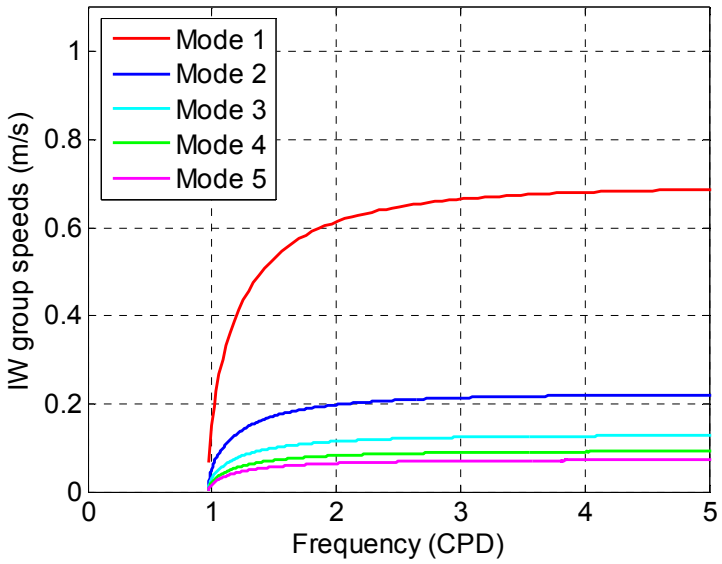

Figure 6.13 IW group speeds for the first five modes.

Based on this general knowledge about IWs, we can "propagate" the time series of temperature data into space. The "space" in between the two temperature points is equal to ΔT*0.6. Since the sampling rate of the thermistor is 30 sec/sample, the spacing is 30*0.6 = 18m. The salinity data used here are from CTDs. The resultant sound speed

field of FM will look like Figure 6.14. Figure 6.14 shows the snapshots of sound speed fields when signals 1, 8, and 16 were taken. The relative locations of the acoustic signals with the high frequency wave packets are plotted on the left. In this figure, not only the HF wave packets are clearly defined but also the long wavelength semidiurnal tides. This plot provides evidence for the hypothesis that the coherence in FM was under the influence of strong internal wave activities. As observed earlier, the approximate location of where coherence started to change happens to be around 20km. This coincides with the HF wave packets and the crest of the internal tides. The thermocline varies between 35~65m induced by the internal tides with the high frequency oscillations riding on top. To separate the effects of internal ides and HF packets, the HF packets in Figure 6.14 are filtered out. The sound speed field corresponding to the internal tides is shown in Figure 6.15.

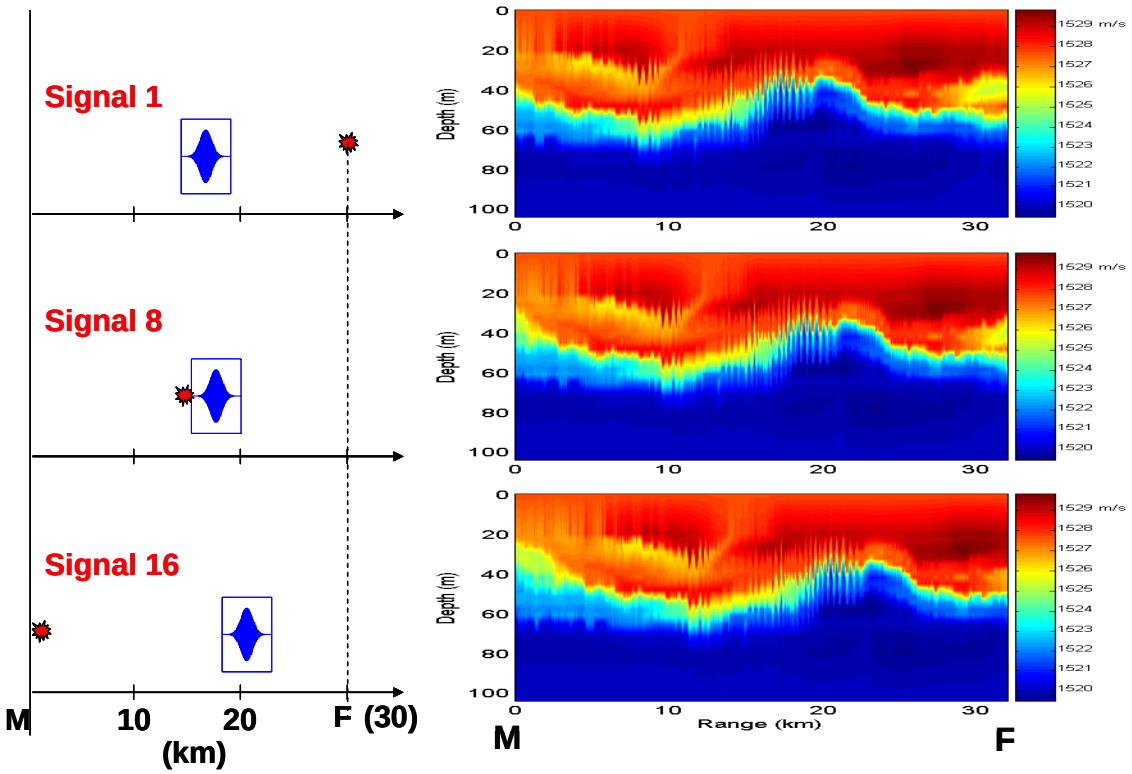

Figure 6.14 Propagated sound speed field using temperature time series.

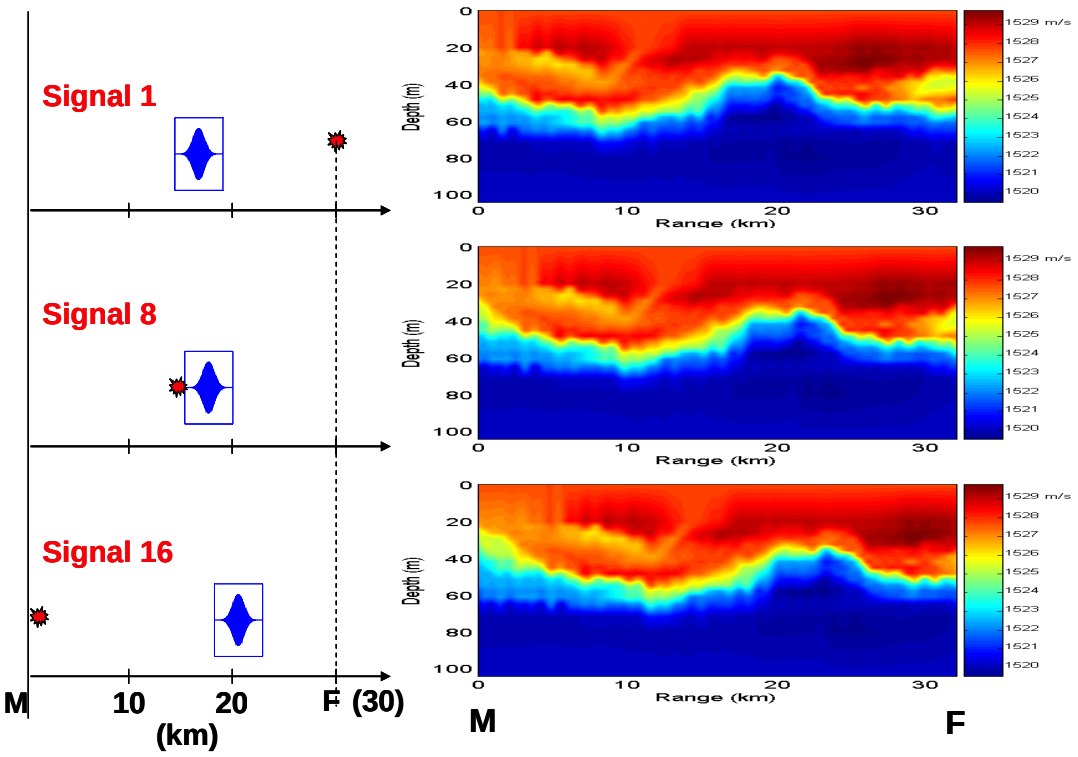

Figure 6.15 Propagated sound speed field using LPF temperature time series.

The propagated sound speed field is again used as an input to the range dependent acoustic model and results are collected in Figures 6.16 and 6.17. Each figure has three curves: one from experiment, one from the modified GM spectrum model, and one from the above "propagated" sound speed field. 6.16(a) and 6.17(a) correspond to sound speed field only containing the internal tides (linear IWs, Figure 6.15) while 6.16(b) and 6.17(b) include both internal tides and the high frequency wave packets.

The results are a little surprising. The long wavelength internal tides are usually regarded to have little acoustic effects on sound propagation using SUS charge signals, which is due to the difference in their speeds. In addition, the nonlinear high frequency wave trains have been reported to cause considerable variations in acoustic signals (see section 1.1.2). The comparison here with and without the HF packets is not substantial.

Both predictions capture the change in signal coherence while case (b), with additional HF packets, shows more fluctuations.

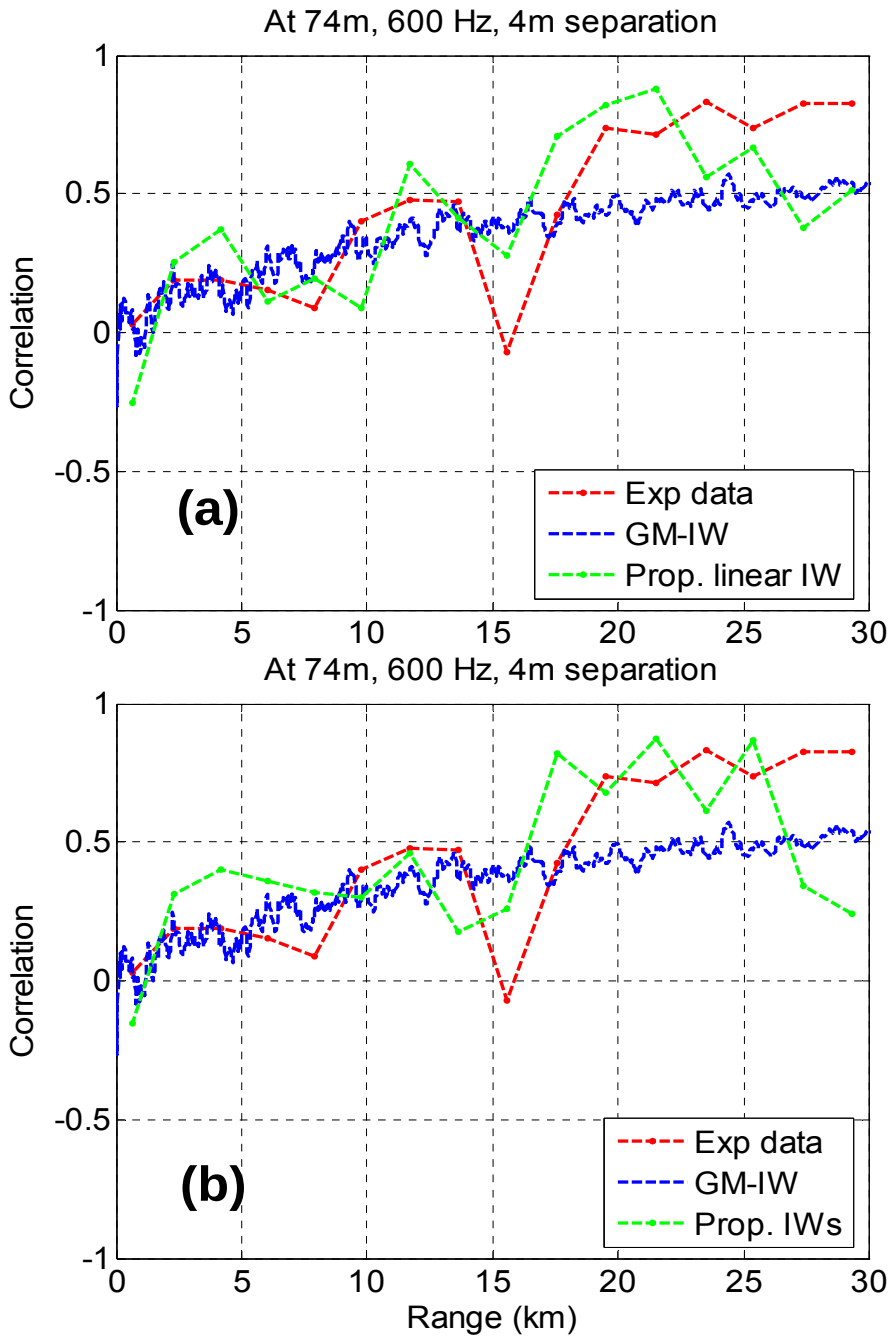

Figure 6.16 Comparison of experimental data with GM model and propagated sound speed fields at 600 Hz. (a) case of Figure 6.15; (b) case of Figure 6.14. (Same sediment properties as Figure 6.11)

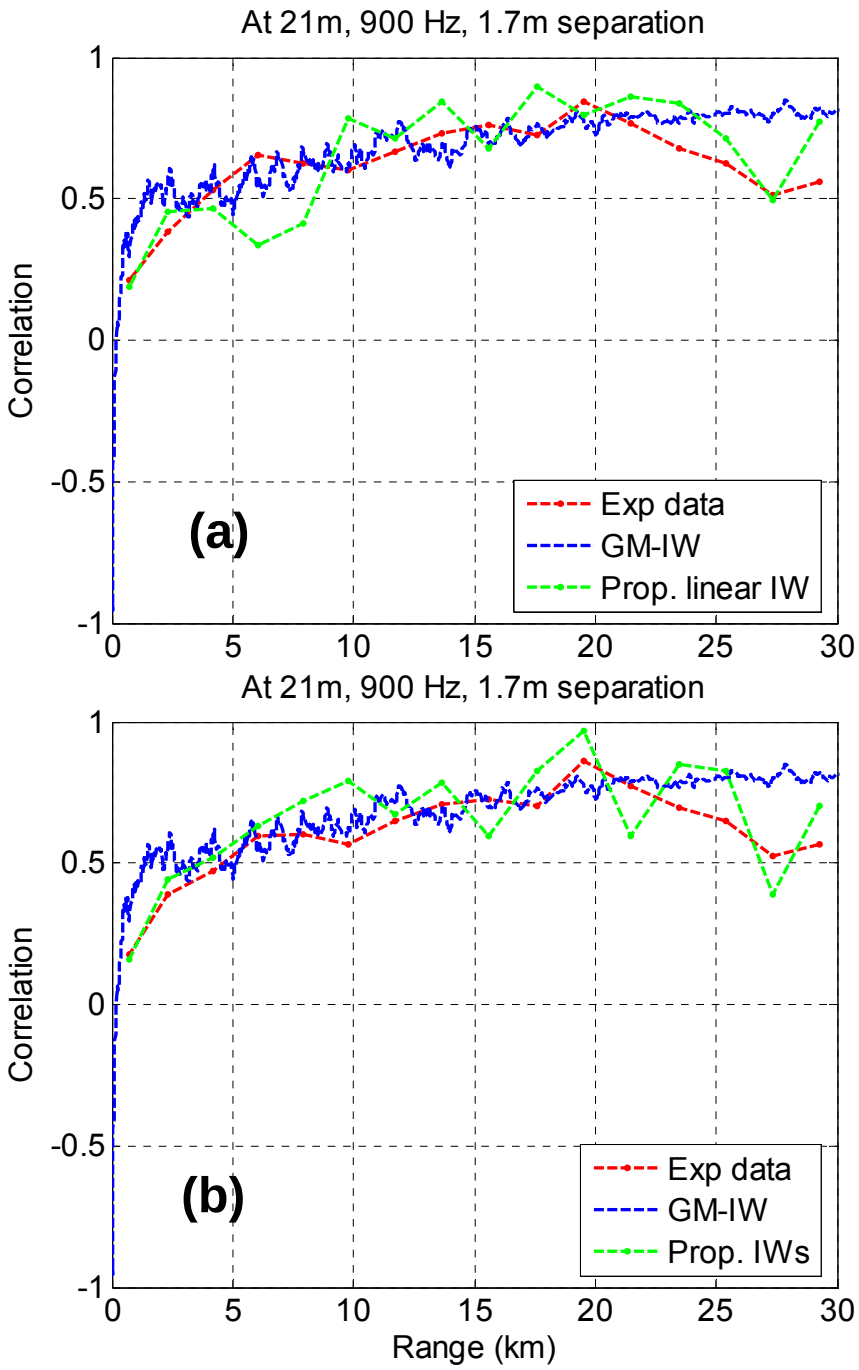

Figure 6.17 Comparison of experimental data with GM model and propagated sound speed fields at 900 Hz. (a) case of Figure 6.15; (b) case of Figure 6.14. (Same sediment properties as Figure 6.11)

CHAPTER 7

ENVIRONMENTAL PARAMETER III:

SEA SURFACE WAVES

7.1 Characteristics of Wind-Generated Surface Waves at ASIAEX

During the Asia Seas International Acoustics Experiment (ASIAEX) in the ECS (ECS), nine days of consecutive wind velocity and directional wave spectrum data were recorded and made available online by Peter H. Dahl (APL-UW).

The acoustical effects of the surface waves from ASIAEX were investigated by Dahl (2004[2]) and Zhou et al (2004, 2007). Dahl presented the spatial coherence of a sound field scattered once from the rough sea surface and received on a vertical array. A narrow-band source was used in mid to high frequency range, i.e. 8-20 kHz. Field data agreed well with theoretical models using the van Cittert-Zernike theorem. Zhou *et. al.* demonstrated the surface effects on reverberation vertical coherence, reverberation level, and inversion results based on reverberation vertical coherence. The frequency range of interest here is 100-2500Hz. Both vertical coherence and inversion results show clear response to the surface waveheight variations. The inverted effective bottom attenuation increases with the RMS surface waveheight. Figure 7.1 is an example of reverberation vertical coherence that increases with rising RMS surface waveheight (Zhou et al, 2004).

7.1.1 Wind Velocity and Wave Age

During ASIAEX, wind speed and direction were recorded every half an hour from the R/V Melville's IMET station, which is about 14 meters high. Figure 7.2 shows the

nine-day wind speed record together with its direction. One interesting feature to note is the sharp decrease in wind speed at the beginning of day 2 and day 9 which may be due to 180º wind direction change. The ASIAEX data provide valuable information on surface wave field response to changing wind fields.

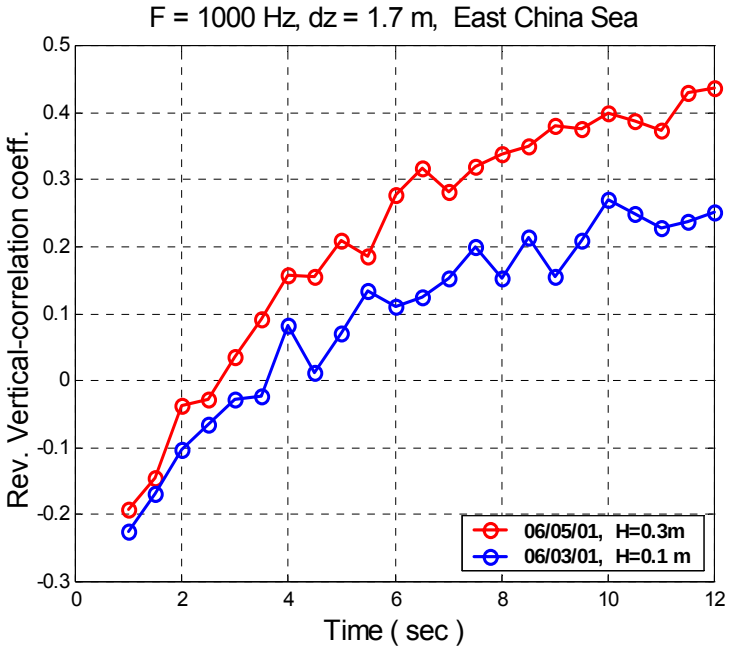

Figure 7.1 Comparison of vertical coherence at different sea states.
H indicates RMS surface waveheight.

Many authors (Hasselmann et al, 1980; Allender et al, 1983; Masson, 1990; Smith et al, 1992) used "wave age" to quantify the development of surface wave fields. Wave age is defined as U_r / c or U_r / c_p with U_r the wind velocity at a reference height, c the surface wave phase velocity and c_p the phase velocity at the peak frequency of its spectrum. The magnitude of wave age is a measure of wind input. For a young developing sea, its wave age is more than unity. As time goes on, the young sea will reach fully developed state with U / c_p in the range 0.8 ~ 1.0. Energy input from the wind

ceases when the wave speed exceeds the wind speed. The wave age keeps decreasing as the fully developed sea gradually die out to old waves. Figure 7.3 shows that for the conditions during ASIAEX, U/c_p was in the range of 0.05~1.6. Over the 9 day observation period, a fully developed sea was rarely observed or only appeared for a very short period although the wind speed changed significantly from 1~11m/s.

The variability of the recorded spectrum sometimes makes it difficult to determine the spectral peak directly. Therefore, we implemented the technique introduced by Young (1999) to calculate f_p instead of finding the maximum spectral density directly.

Young's formula is:

$$f_p = \int_0^\infty fF^4(f)df \Big/ \int_0^\infty F^4(f)df \tag{7.1}$$

where *F(f)* is the surface frequency spectrum.

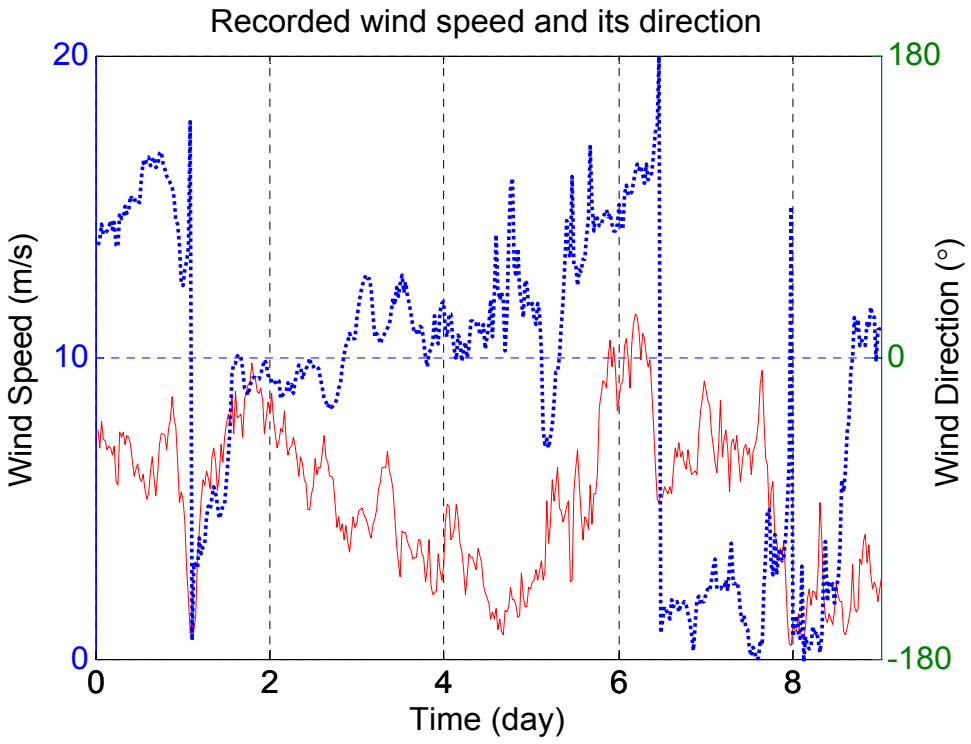

Figure 7.2 Record of wind speed and direction for nine consecutive days at the ASIAEX starting 00:00 May 29, 2001. Solid line: wind speed; dotted: wind direction.

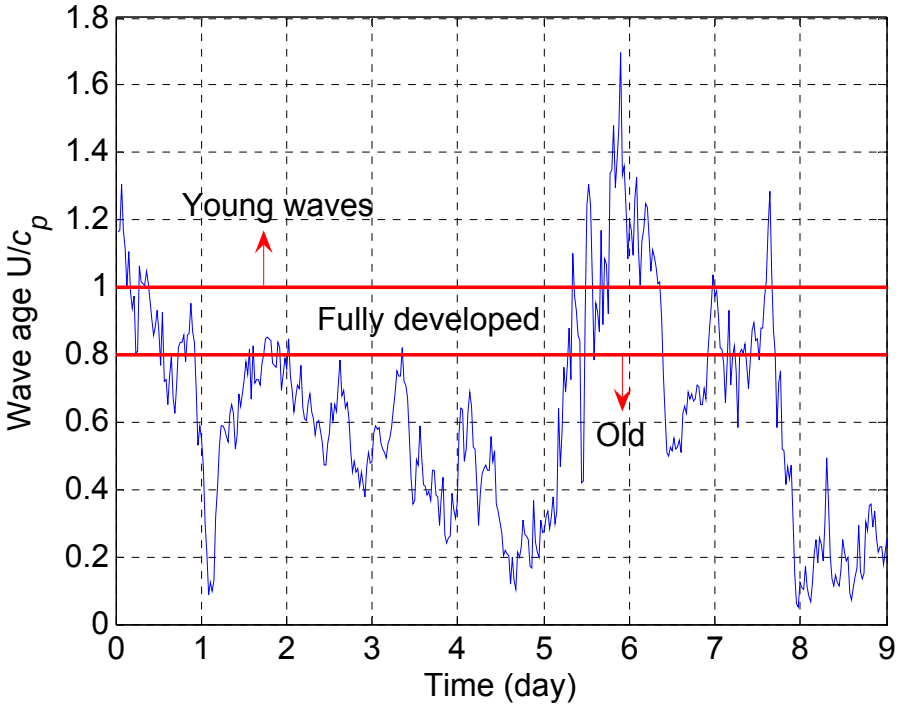

Figure 7.3 Time history of wave age from ASIAEX.

Directional surface wave spectra were recorded by Dahl (2004[1],[2]) using a 0.9-m diameter TRIAXYS directional wave buoy 500 meters away from Melville. The directional wave buoy measured waveheight variance spectra in 0.005-Hz bins from 0.03 Hz to 0.64 Hz, and in 3-degree directional bins. Spectra were computed every 0.5 h based on a 20-min averaging time. The non-directional spectrum shown in Figure 7.4 is the average of directional wave spectrum over all angles. It is apparent that surface wave energy is highly concentrated in the frequency range 0.1 ~ 0.3 Hz and spectral level is in direct response to the magnitude of the wind speed.

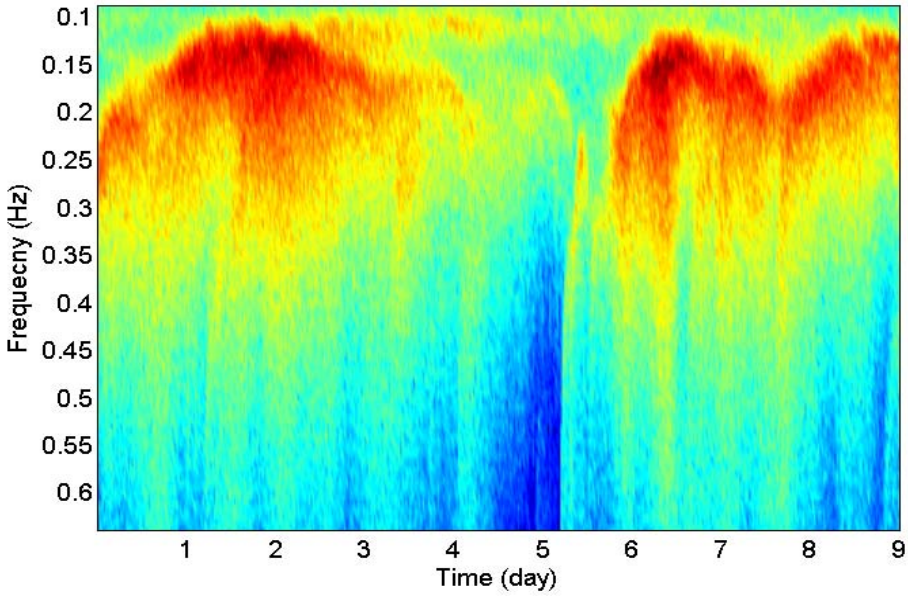

Figure 7.4 Color plot of 9-day surface spectrum starting May 29, 2001. (From: Overview of Results from the Asian Seas International Experiment in the East China Sea P. H. Dahl, et al., IEEE J. Oceanic Eng. Special Issue on Asian Marginal Seas).

7.1.2 Non-Directional Surface Spectra

The surface frequency spectrum usually takes a unimodal or one-peak form as in Figure 7.5(a) left. The well-defined peak falls in the range of 0.1~0.3 Hz and f_p tends to decrease with increasing wind speed. High frequency has higher values for U/c which makes it respond to wind force more rapidly and hence to have a flatter rear face. For steady or gently changing wind field, the spectral peak usually aligns with the wind direction quite well (Figure 7.5(a) right).

Figure 7.5(a), (b), (c) corresponds to young waves, fully developed sea, and old waves with U/c_p = 1.1, 0.92, 0.41 respectively. The three cases have a decreasing wind speed that is confirmed by their spectral density.

A bimodal structure of the frequency spectrum was observed from 12:00 June 1 to 20:00 June 3 as shown in 5(c). The first peak existed throughout the period at the same position 0.11 Hz. The color plot of a twin peak case indicates this as well (Figure 7.5(c) right). This bimodal structure has also been observed in the coastal region by other authors (Allender et al, 1983; Masson, 1990; Smith et al, 1992).

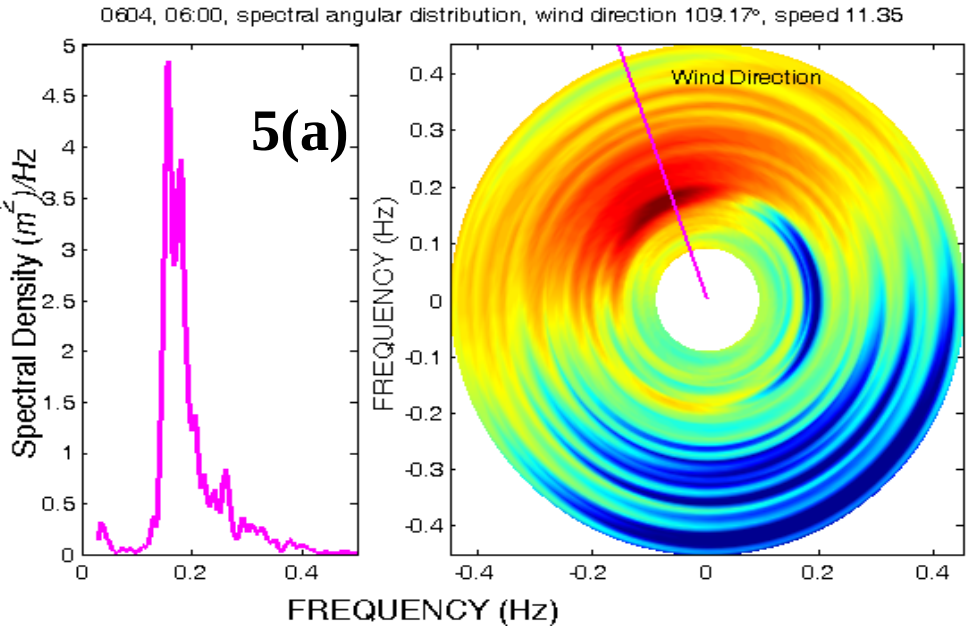

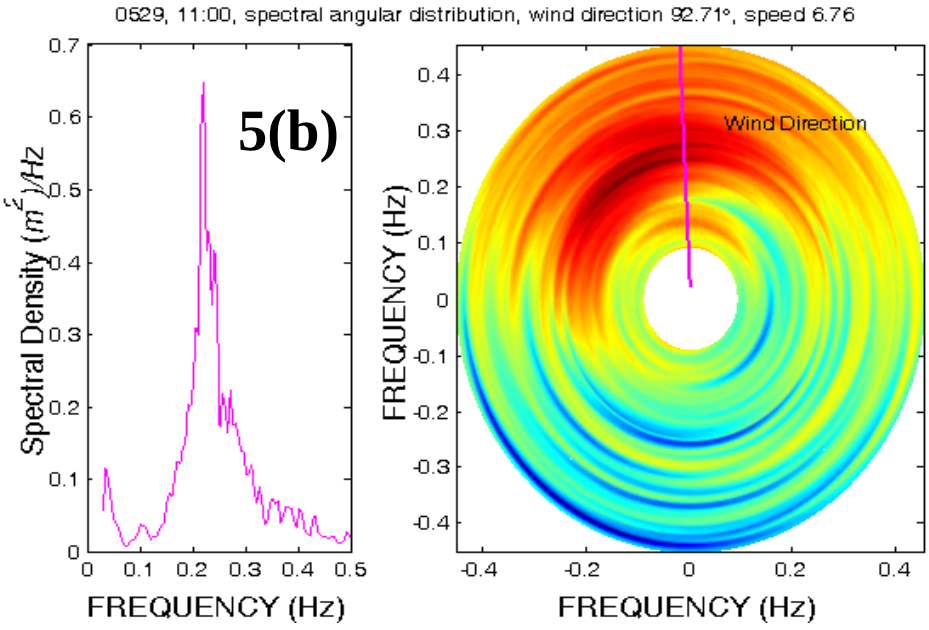

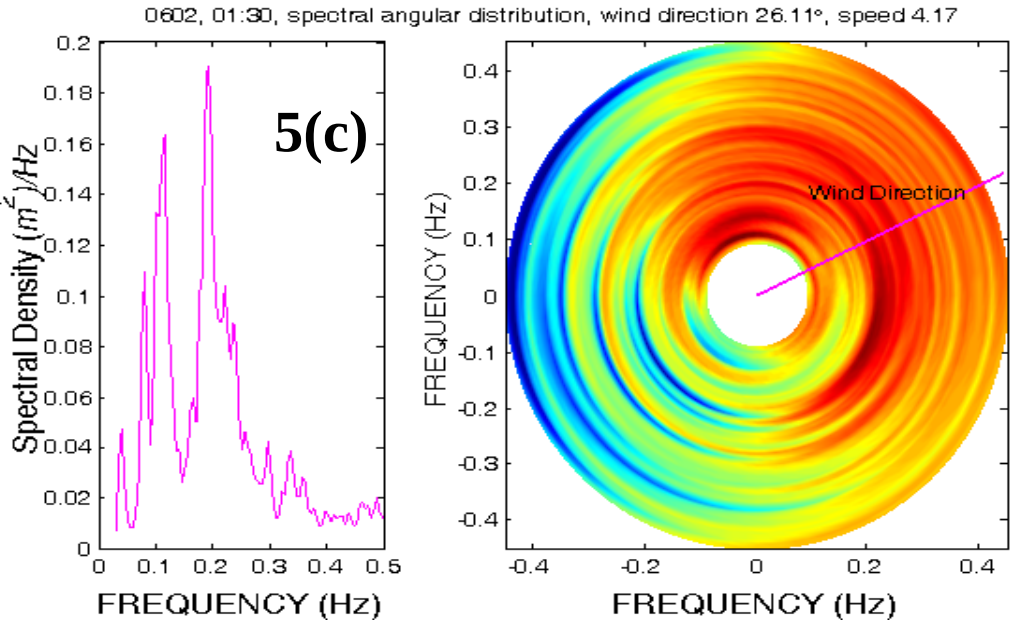

Figure 7.5 (a) young waves, (b) fully developed waves, and (c) old waves.

7.1.3 Response of Directional Wave Spectra to Veering Wind Fields

7.1.3.1 Gradual Change in Wind Direction

The ASIAEX data contains a 16-h period on day one (00:00 to 16:00, May 29) which exhibits a gradual change in wind direction. The wind speed was between 6-8 m/s and wind direction changed 45º in about 13 hours. Figure 7.6(1)-(4) shows the evolution of the directional spectra. It is apparent that the spectra responded to the mild direction change very well and the spectral peaks lined up with the wind direction most of the time. Our observation agrees with Young (1987) that the whole spectrum will rotate with the wind if the wind direction change was less than 60º. Four different frequencies were chosen to show the directional response in Figure 7.6(5). The four frequency components, from low to high, follow the gradual direction change pretty well.

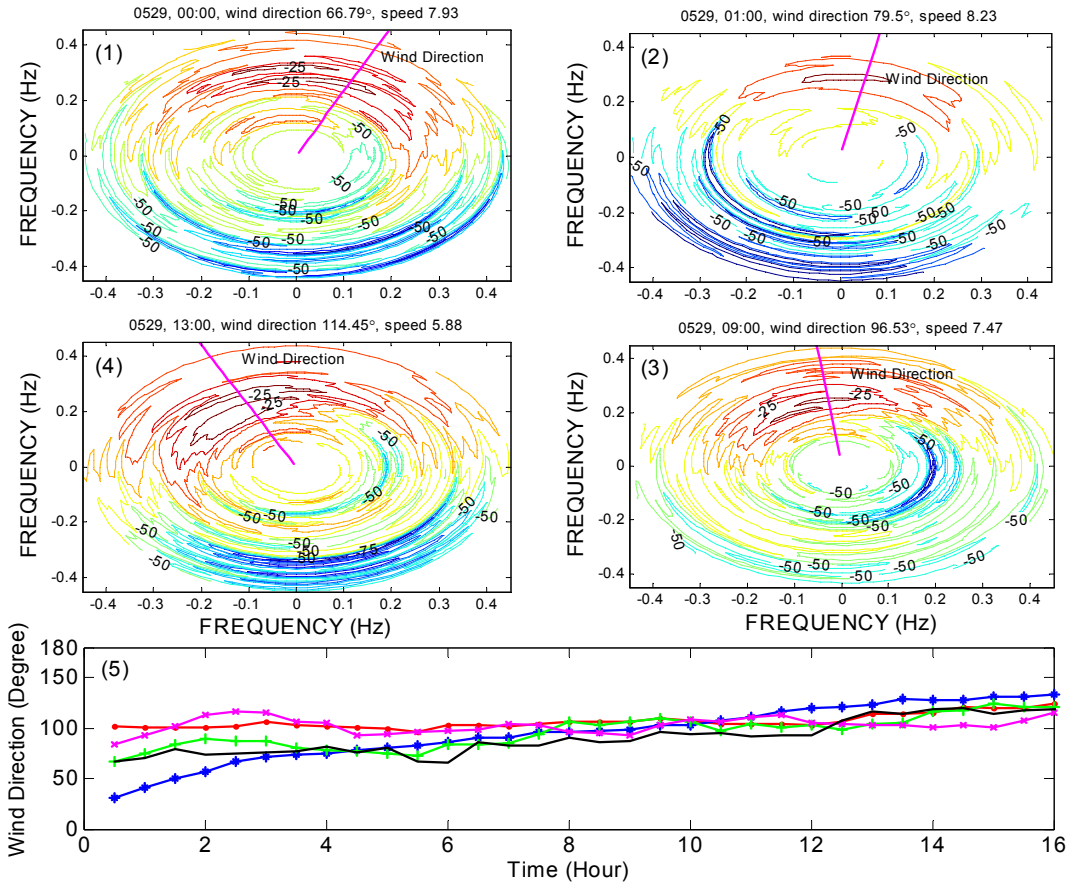

Figure 7.6 Response of surface waves to 45 º wind direction change from 00:00-13:00, May 29, 2001. (1)-(4) are snapshots showing the alignment between directional spectral and wind direction within this period. (5) shows the wave direction at four different frequencies. Dots, stars, pluses and crosses represent 0.15, 0.25, 0.35, and 0.45 Hz.

7.1.3.2 Sudden change in wind direction

Two periods of sudden wind direction change were also recorded between 01:00-03:00 May 30 and 08:30-12:00 June 4 (day two and seven). The first period has about 210º over 2 hours and the second has 75 º variation over 3.5 hours. The latter was chosen as an example here (Figure 7.7).

The quick response in the high frequency range is anticipated while the rather rapid shift in the low frequency is a bit surprising. In about 3.5 hours, not only the high

frequency, but also the low frequency components show an obvious movement towards the wind direction except the 0.15 Hz case. Young (1987) found that a second peak would be formed in the new wind direction if the sudden change was greater than 70º. This is also observed from Figure 7.7(3) and (4) using the ASIAEX data. It took about 5 hours for a second peak to be formed in the new wind direction. The old peak which remains in Figure 7.7(4) will gradually die out. Figure 7.7(5) demonstrates how low and high frequencies respond to the sudden change. Frequencies above 0.3 Hz exhibit clear response to the direction change while the lowest frequency components show no sign of responding.

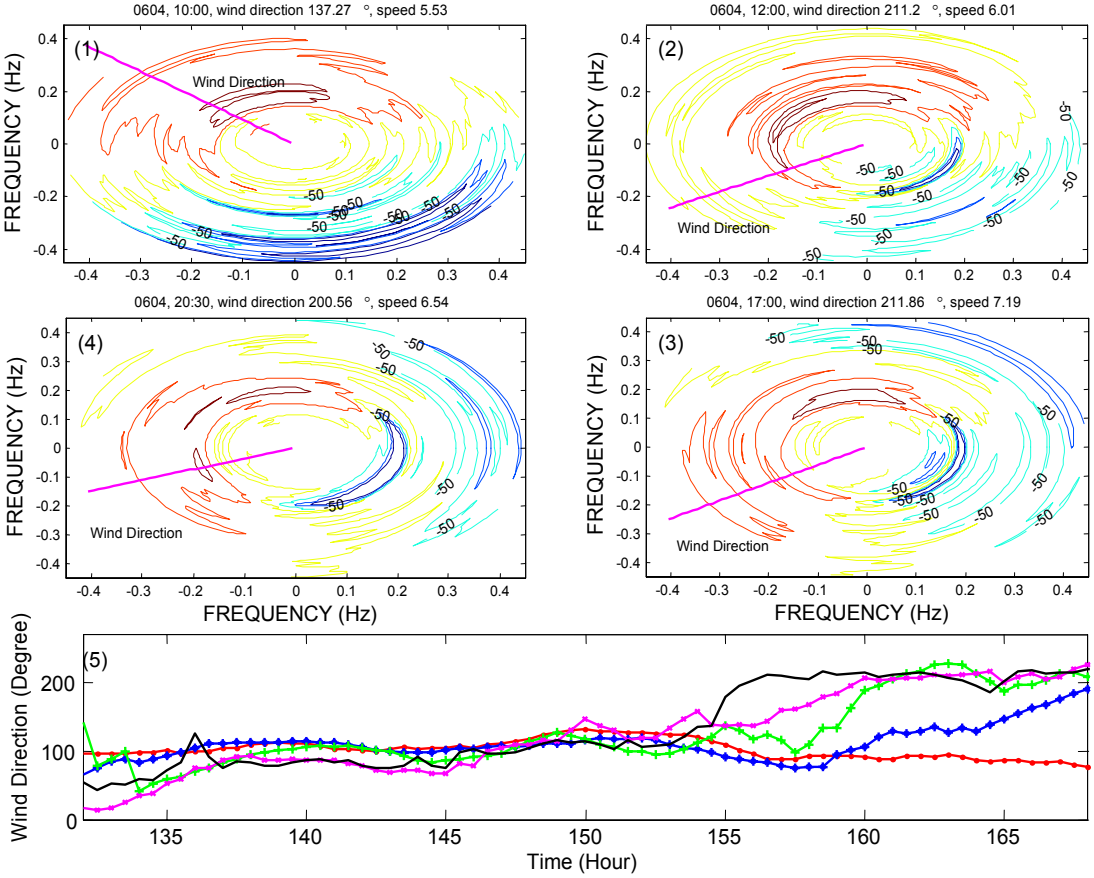

Figure 7.7 Response of surface waves to 75° wind direction change, 8:30:12:00, June 4, 2001. Figure format and symbols are the same as Figure 6.

7.2 Comparison of ASIAEX Data with Proposed Surface Spectrum Models

There are two kinds of surface spectra that appear in the literature that differ primarily in the slope of the spectrum beyond the spectral peak. The first category includes most widely used Pierson-Moskowitz (Pierson and Moskowitz, 1964) and JONSWAP (Hasselmann et al, 1976) models with f^{-5} proportionality for frequency dependence beyond the spectral peak. The other form, proposed by Toba (1973), has f^{-4} frequency dependence. The PM model has a simple form but is only valid for a fully developed sea which requires steady winds of long fetch and duration. Both of the JONSWAP and Toba spectra made modifications to the PM form based on the high frequency formulation of Phillips (1958).

Since the 1990's, much effort has been made to build a surface spectrum that is valid over all wavenumbers for application in the area of electromagnetic scattering (McDaniel, 1982; Elfouhaily et al, 1997; Lemaire, et al, 1999; Plant, 2002). The new form has combined low- and high-wavenumber regimes corresponding to both surface gravity and capillary waves. The low-wavenumber regime takes a similar form from the existing JONSWAP or Toba-Donelan model (Donelan et al, 1985). The spectral forms at high wavenumbers are based on the work of Phillips, Kitaigorodskii and Plant (Kitaigorodskii, 1973; Phillips, 1985; Plant, 1986). Since the ASIAEX data only contained frequency components up to 0.64 Hz, the inclusion of these references is merely for the sake of completeness.

7.2.1 Surface Spectrum Models

For surface gravity waves, the two types of surface spectrum models are based on the work from Pierson & Moskowitz and Phillips. The original Pierson-Moskowitz model (PM) has been most widely used due to its mathematical simplicity:

$$S(f)=\frac{\alpha g^2}{(2\pi)^4 f^5}\exp\left(-\frac{\beta g^4}{(2\pi)^4 f^4 U^4}\right)=\frac{\alpha g^2}{(2\pi)^4 f^5}\exp\left(-\frac{5}{4}\left(\frac{f_p}{f}\right)^4\right) \tag{7.2}$$

Here, α = 0.0081, β = 0.74, U is the wind speed at 19.5m, g is the gravitational acceleration. f_p is the spectral peak frequency defined as $f_p = 0.14g/U_r$. The PM model is only valid for fully developed sea, i.e. U/c_p between 0.8 and 1, which usually is not suitable for the coastal area (Heitsenrether et al, 2004). Examples of the PM model at median and high wind speeds (6.27 and 11.45 m/s) are shown in Figure 7.8 along with the actual measured surface spectra at the two times. The PM model shows a relatively quite good fit to the experimental (7.8, left) while it exceeds the experimental by a factor of 2 at 11.45 m/s. This supports the theory that the assumption of fully developed sea state may not be suitable for shallow water.

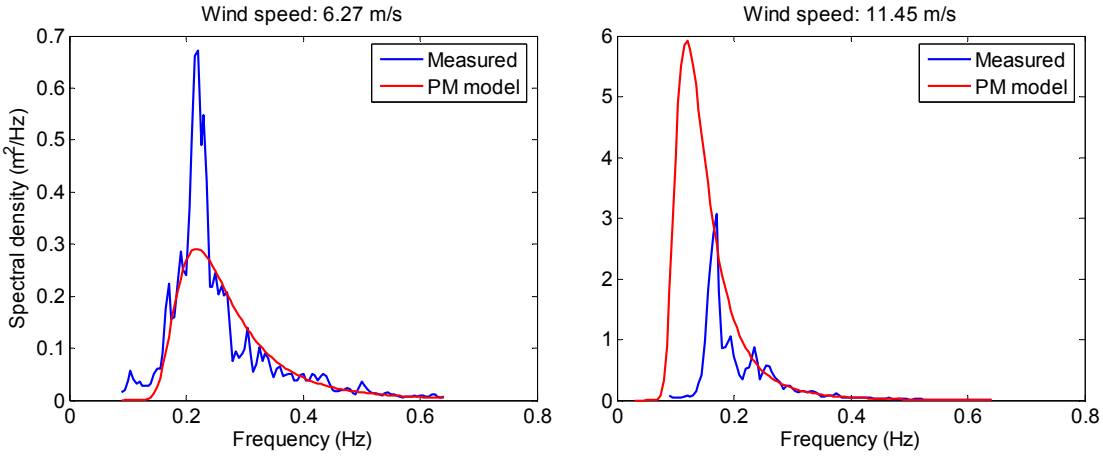

Figure 7.8 Comparisons of PM model with measured spectrum at two wind speeds.

In coastal area, a fully developed sea state is rarely reached due to limited fetch and swell component. This is the case for ASIAEX. Based on Phillips' formulation in high frequency range, Hasselmann et al (1976) proposed JONSWAP (Joint North Sea Wave Project) spectrum of fetch-limited conditions:

$$S(f)=\frac{\alpha g^2}{(2\pi)^4 f^5}\exp\left(-\frac{5}{4}\left(\frac{f_p}{f}\right)^4\right)\gamma^{\exp\left(-\frac{(f-f_p)^2}{2\sigma^2 f_p{}^2}\right)} \tag{7.3}$$

In (7.3), α, γ, and σ are functions of non-dimensional parameter υ by power law with $\upsilon = f_p * U_r / g$. The parameter υ and the wave age U/c_p only differ by a factor of $1/2\pi$. The peak frequency f_p is now fetch-dependent: $f_p = 3.57g/\left(U_r \xi^{0.33}\right)$ where ξ is non-dimensional fetch defined as: $\xi = gx/U_r^2$. x is the actual fetch in meter. Using the same formula, Mitsuyasu et. al. (1980) found a new set of relations between α, γ, σ and υ with less scatter. Both of their results are summarized in Table I (Young, 1999).

Toba (1973) proposed the f^{-4} form:

$$S(f)=\frac{\alpha g^2}{(2\pi)^4 f_p f^4}\exp\left(-\left(\frac{f_p}{f}\right)^4\right)\gamma^{\exp\left(-\frac{(f-f_p)^2}{2\sigma^2 f_p{}^2}\right)}. \tag{7.4}$$

The spectrum changes as $f_p{}^{-1} f^{-4}$ instead of f^{-5}. This formulation has been supported in the literature both experimentally and theoretically (Donelan et al, 1985; Kitaigorodskii, 1983). Donelan et al (1985) found his results based on a data set with U_r/c_p in the range of 0.83 ~ 4.6 (Table 7.1).

Table 7.1 Surface Model Parameters
(All parameters in the form of y = amp.* υ^{power}.)

Model		PM	JONSWAP-Hasselmann	JONSWAP-Mitsuyasu	TOBA-Donelan	ASIAEX
U/c_p range		0.8 ~ 1	0.88 ~ 5	< 0.82	0.83 ~ 5	1~1.6
α	Amp.	Const = 0.0081	0.036	0.033	0.0165	0.011
	Power		0.87	0.86	0.55	0.465
γ	Amp.	-	4.12	4.42	1.7, if υ <0.159; 6.489+6log υ, o.w.	4.560
	Power		0.32	0.43		0.257
σ_a	Amp.	-	0.54	Const. = 0.07	σ =0.08+ $1.29*10^{-3}\,\upsilon^{-3}$	0.270
	Power		-0.32			0.578
σ_b	Amp.	-	0.078	Const. = 0.09		0.075
	Power		-0.16			-0.061

7.2.2 RMS Surface Waveheight

For acoustic considerations, surface wave height is a very important parameter. It is valuable to know which surface model gives the best wave height prediction. The RMS wave height was calculated using the four models and compared with the ASIAEX data. Figure 7.9 shows the comparison between models and the experimental data. It is quite obvious that the JONSWAP-Mitsuyasu model exhibits the best fit of the four. A possible explanation for this is that over 70% of the ASIAEX data have low wind input (U/c_p <0.8) which is similar to the case of Mitsuyasu. The Mitsuyasu model shows a little deviation from the experimental curve under three cases, if compared with Figure 7.3: (1) U/c_p <0.6; (2) U/c_p >1; (3) existence of swell (12:00 June 1 to 20:00 June 4).

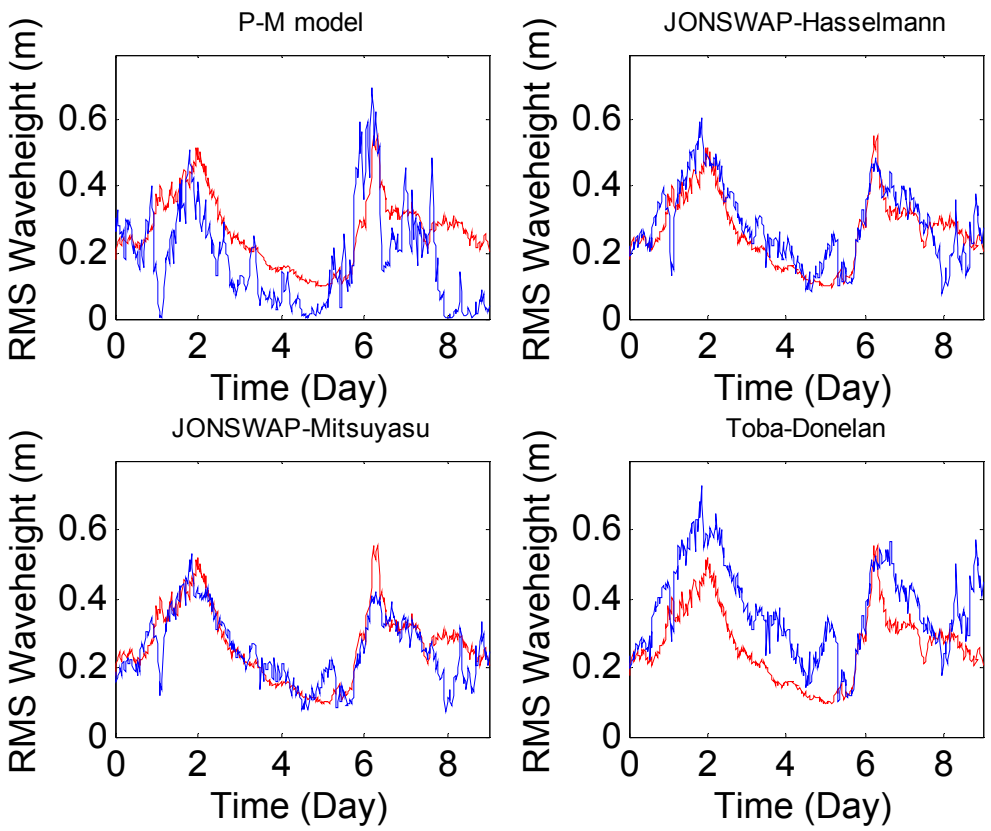

Figure 7.9 Comparison of calculated RMS waveheight from four models with the ASIAEX data. Red: experimental RMS; blue: model RMS.

7.3 Acoustical Effects of Sea Surface Waves

The combined JONSWAP-Mitsuyasu model found previously will be used to study the surface effects on vertical coherence. The procedure is as follows:

1. Start with the 1-D surface spectrum and multiply a random phase to each spectrum data point; then, convert that to surface height variations using inverse spatial FFT;
2. Assume half-space sediment sound speeds as 1620 and 1630 m/s in ME and MG directions (Figure 7.10 top right);

3. Since sound propagates much faster than surface gravity waves, we assume a "frozen" ocean for each received signal. Therefore, the representative surface waveheight pattern found in step 1 can be used as the top boundary of the ocean;
4. A FORTRAN program called Range-dependent Acoustic Model (RAM) is used to calculate the sound field and vertical coherence;
5. Repeat step 1-4 for 100 independent realizations of the surface wave pattern. Then take the average of these 100 realizations at each center frequency;
6. Compare results with the ECS measured spectrum and with other surface models.

As mentioned in Chapter 2, there were three radial tracks with acoustic measurements: ME, MG, and MF. Corresponding oceanographic data have shown that they were acquired under different sea states: ME has the lowest wind speed while MG has the highest (Figure 7.10). Here, we will compare mainly ME with MG since we believe there were internal wave activities when FM measurements were performed. The 1-D spectrum in Figure 7.11 for the MG direction shows much higher energy than for the ME direction. The spectrum peak in between 0.2 and 0.3 Hz is due to the wind forcing and will keep shifting to lower frequency with rising wind speed. A smaller peak at 0.1 Hz is swell which may be the result of a distant wind field.

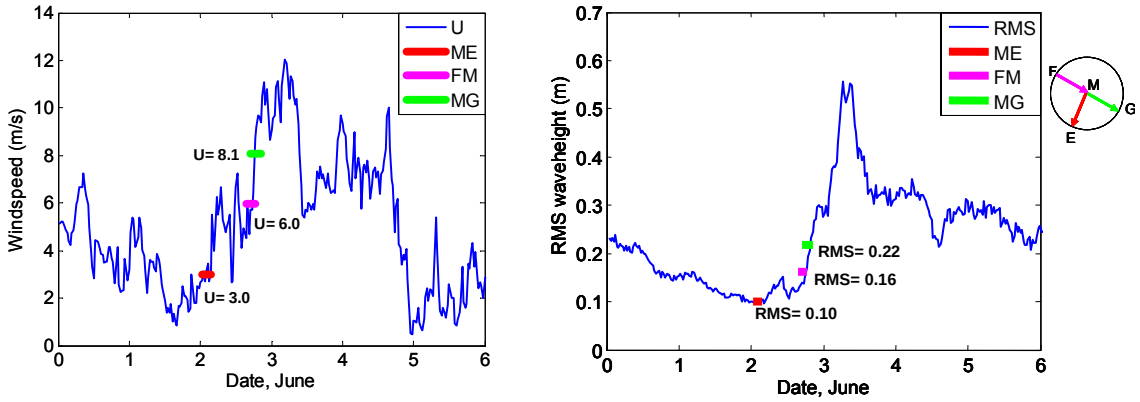

Figure 7.10 Left: windspeed; right: RMS waveheight from ASIAEX.

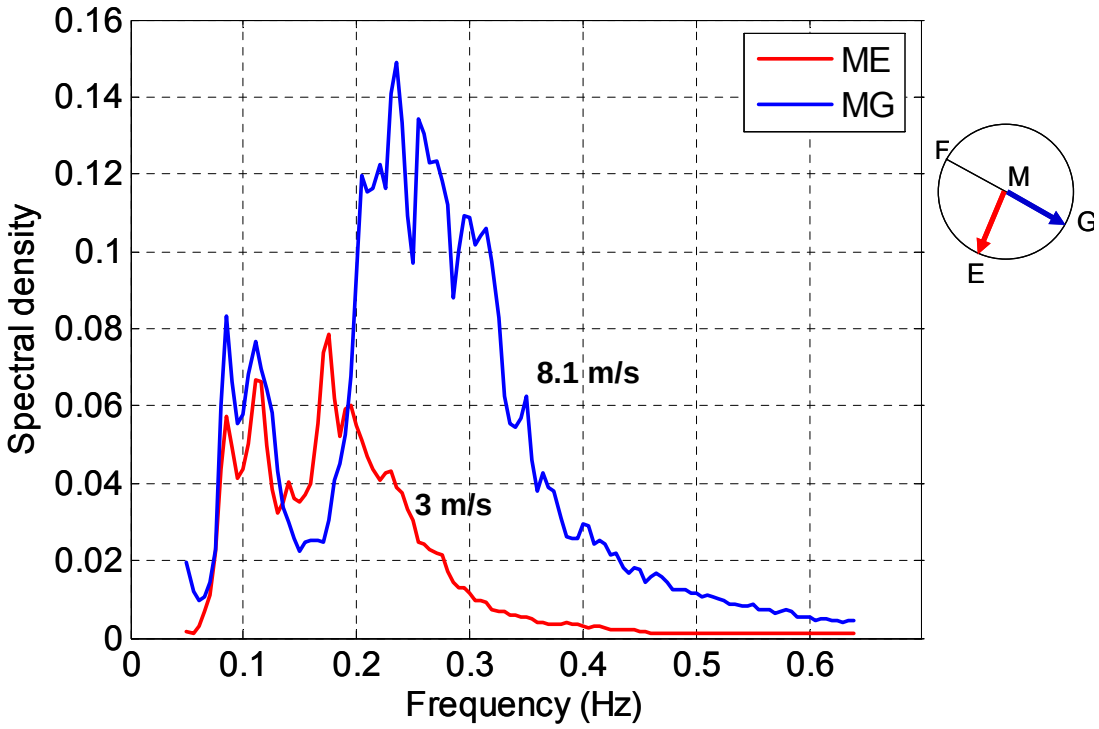

Figure 7.11 Comparison of 1-D surface spectrum at wind speeds 3 and 8.1m/s.

Before showing the data/model comparison, we will first show how the acoustic measurements change due to different wind conditions. Four comparisons of measured correlation versus range plots are shown in Figure 7.12. For the ME curves (red), the windspeed is 3.0m/s and for the MG curves (blue), it is 8.1 m/s. Figures 7.12 (a)-(d) are arranged according to ascending frequency. The depths of the hydrophones are chosen based on two considerations. One, the roughness of the sea surface will have much bigger influence on the receivers close to the surface. The other, the surface effects begin to show up in the data when frequency is greater than 800Hz. In order to have enough coherence between two hydrophones, we need a relatively small separation. Thus, the hydrophone pairs of short separations above the thermocline are selected. As the *kd*-plot

in Figure 4.3 suggests, the separation needs to be smaller than 2λ (2λ is the vertical coherence length).

Figures 7.12 (a)-(d) confirm some of the characteristics of vertical coherence presented in Chapter 4: vertical coherence increases with range and decreases with frequency and separation. The two curves, representing ME and MG respectively, start to deviate from each other around 900Hz. As frequency increases, the difference becomes larger. It is interesting to see that for the most part, the range, where they disagree, is between 5~15 km. This can be explained as the follows.

Surface effects add extra attenuation to the sound field by scattering lower order modes to higher order modes. Therefore, within a short range (5 kilometers in this case), the coherence with higher surface waveheight is a little lower (Figure 7.12 (b)-(d)). This is to say, the propagation distance is not far enough for the surface effects to show up. As range increases, the mode stripping process is accelerated since higher order modes have higher attenuation coefficients. Between 5 ~ 15km, surface effects have made a considerable difference in the results through mode coupling. After sufficient propagation distance, only a few of the lower order modes survive. Therefore, the two curves conform to the same level beyond 15km.

Now, a propagation model using the parabolic equation is applied to examine whether we can explain what we observed. The detailed procedure for the modeling has been addressed at the beginning of this section.

Figure 7.13 shows the results for ME direction. Each figure contains three curves which represent experimental coherence, simulation results using 1-D spectrum measured in the ECS, and simulation results using a flat surface. Other surface models are not

included since they are very close to the ECS curve. Only two cases are shown here since the wind speed is only 3m/s and the difference between flat and rough surfaces is negligible. They both agree with the experimental curve except the first data point at 1km which may contain the non-propagating or evanescent modes.

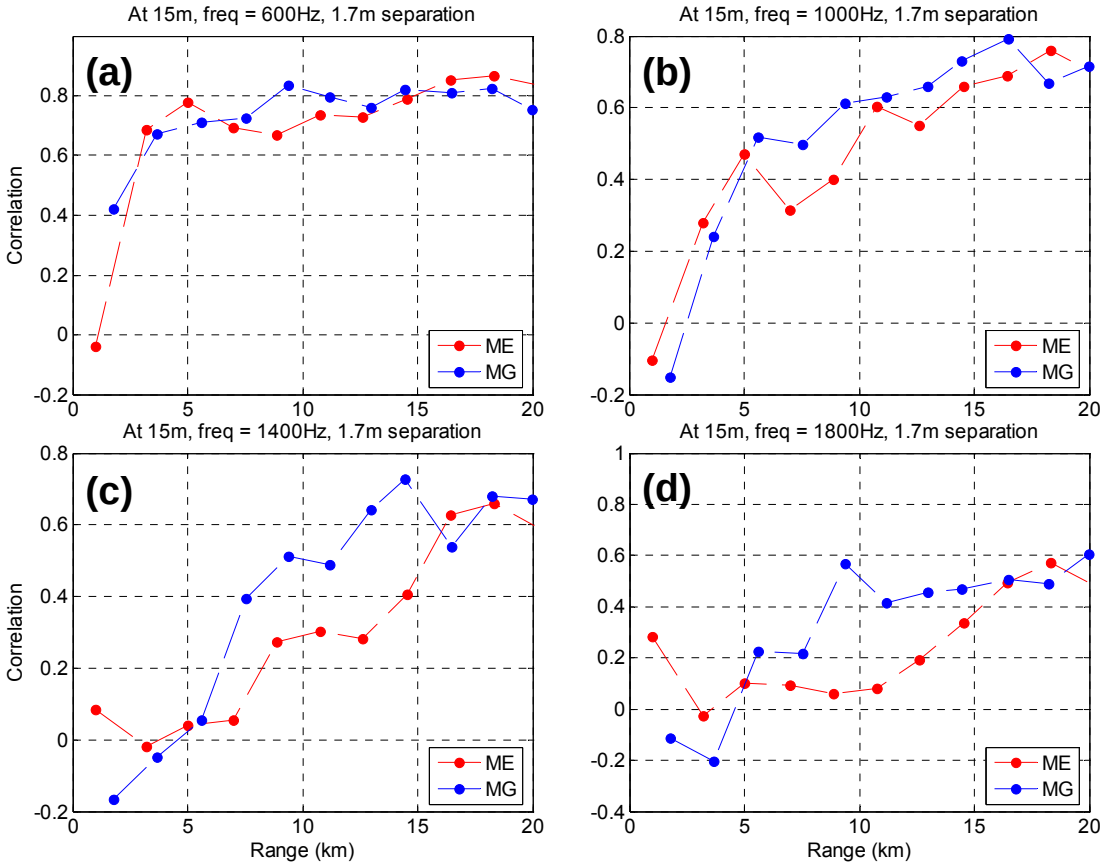

Figure 7.12 Acoustic data comparison between ME and MG at different frequencies.

For the case of MG in Figure 7.14, two surface spectrum models are also included: PM and JW. The two models are very close to each other and to the results obtained using directly measured 1-D spectrum. For frequencies below 500Hz, the four curves show little difference. At 800 Hz, the models, which include surface roughness, show much higher coherence than does the flat surface case. Both models follow the

experimental curve well. The other two figures show similar features. The model results show that surface effects can be considerable for frequencies higher than 800Hz and these effects also depend on the propagation distances.

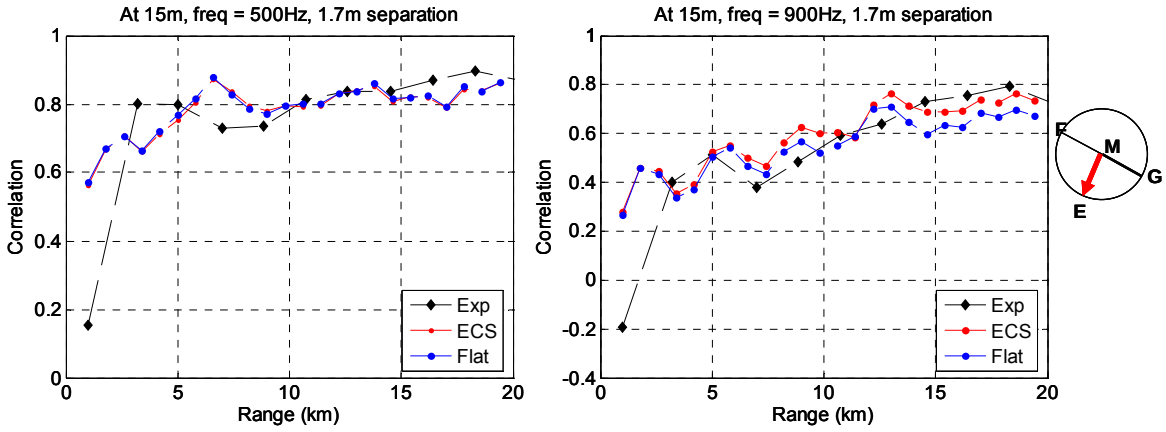

Figure 7.13 Data model comparison for ME direction at two frequencies.

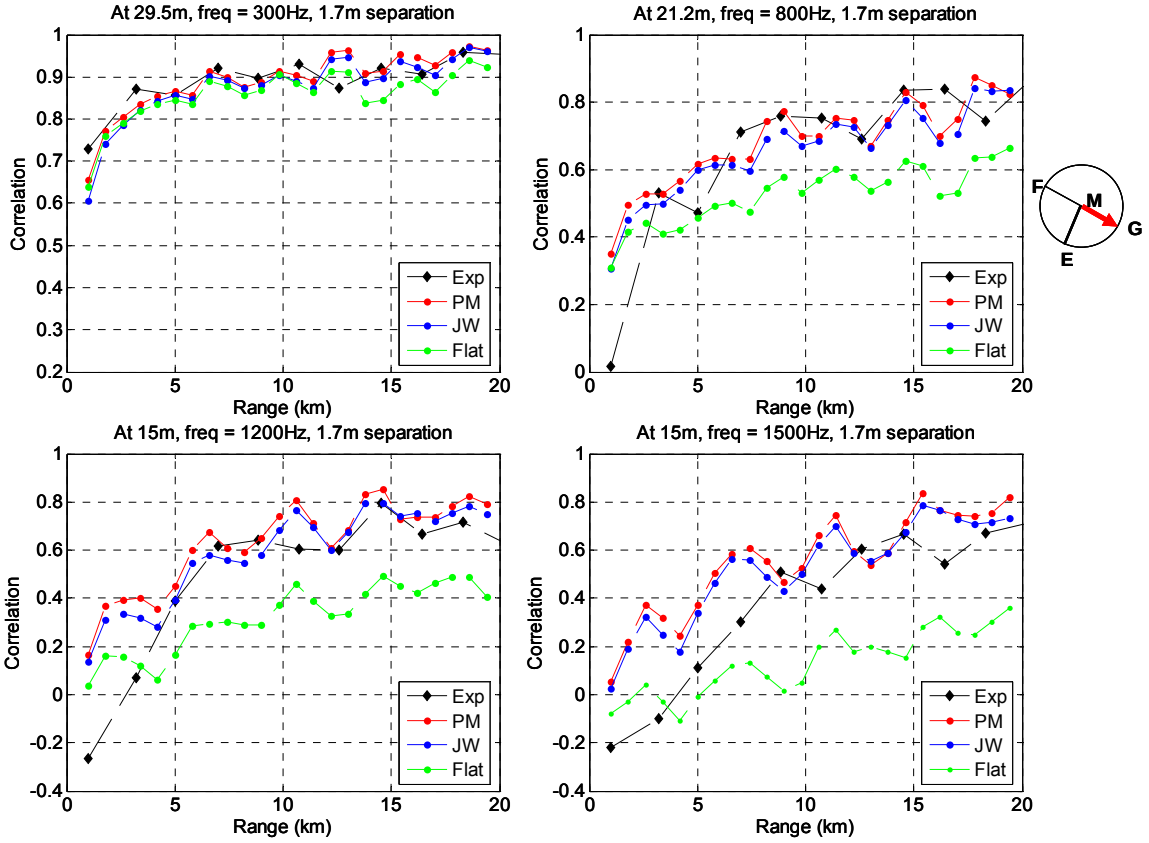

Figure 7.14 Data model comparison for MG direction at four frequencies.

The bootstrap method is used for uncertainty analysis for the sea surface modeling. A total of 200 random surfaces realizations were generated and each time, 50 of them, randomly chosen, were used for calculation of coherence. The 50 coherence results were averaged. The uncertainty was found by repeating the above by 100 times. The results are compared with experimental data in Figure 7.15.

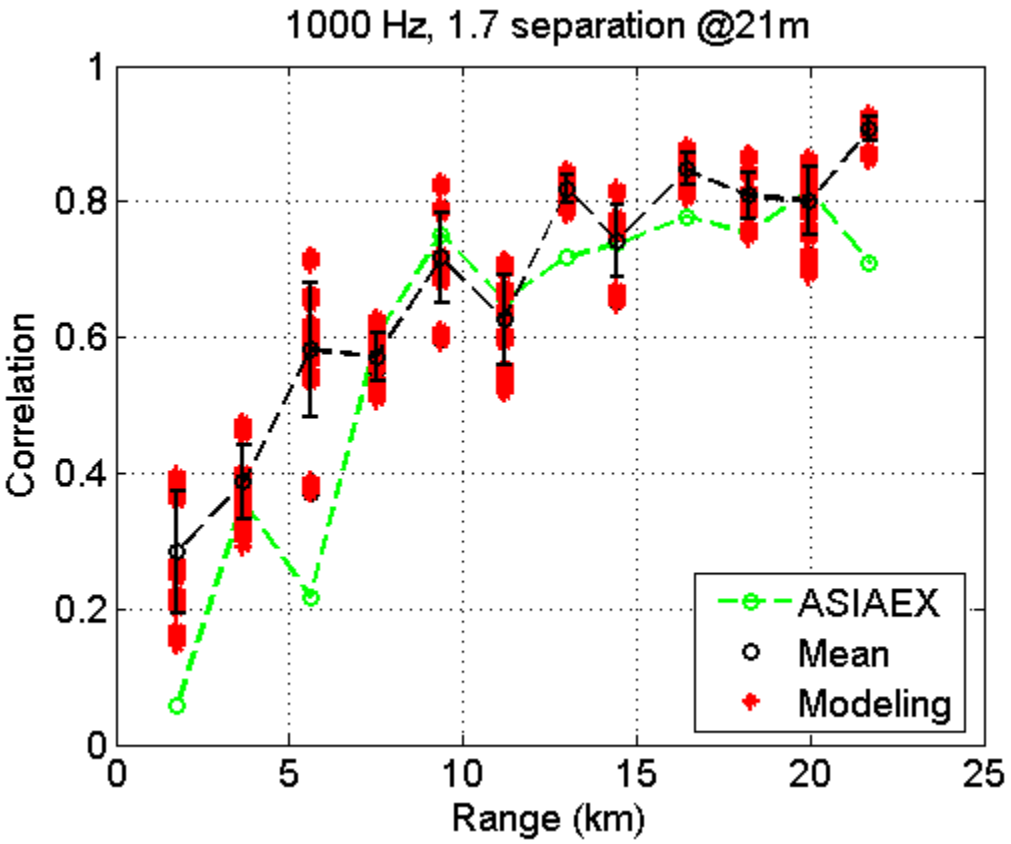

Figure 7.15 Uncertainty analyses for surface modeling using bootstrap method.

CHAPTER 8

TANK EXPERIMENT

8.1 Pulse Compression Technique

8.1.1 Introduction to Pulse Compression Technique

Pulse compression is widely used in radar signal processing as it helps to achieve the desired range resolution with a reduced power of the transmitter. The range resolution of a radar system depends on the bandwidth of the received signal. A short pulse can provide a wide bandwidth since the bandwidth is inversely proportional to the duration of the pulse. On the other hand, however, the transmitted power is proportional to the duration of the pulse, which is to say, the longer the pulse duration, the better the Signal-to-Noise-Ratio (SNR). Therefore, long duration pulse is coded to have appropriate bandwidth. There are two main ways to code long pulses: phase coding and linear frequency modulation. The latter is used in this tank experiment.

8.1.2 Digital Signal Processing Background

Given an input signal s(t), the received signal r(t) is the convolution of s(t) and h(t) in time or multiplication of $S(\omega)$ and $H(\omega)$ in frequency domain after a linear system h(t). For a physical linear system in Figure 8.1, s(t) and r(t) are the transmitted and received signals respectively.

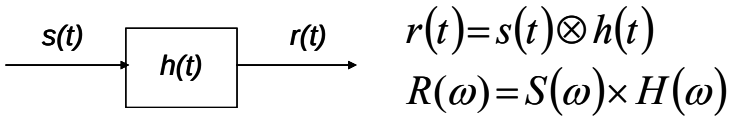

Figure 8.1 A linear system. $\otimes$ indicates convolution.

The system transfer function *h(t)* or *H(ω)* is then found by:

$$H(\omega)=R(\omega)/S(\omega)$$

After finding the system transfer function *H(ω)*, it is straight forward to find the system response of any pulse as long as it has the same or less bandwidth than the original signal S(ω). Mathematically, the system response of any pulse, with an appropriate bandwidth, can be written as (Martin et. al. 2004):

$$R^*(\omega)=S^*(\omega)\times\frac{R(\omega)}{S(\omega)} \tag{8.1}$$

Here, $S^*(\omega)$ has the desired spectrum with bandwidth equal or within that of $S(\omega)$.

This makes the process of data recording much shorter and only one data set is needed. This data set should have a bandwidth wide enough to cover the entire frequency range of interest. To study the received signals at each center frequency, a finite duration Gaussian pulse modulated with sinusoidal waves is used. One main advantage of using this pulse, compared with a sinc function or a square spectrum widow, is that there is no sidelobes in time. The bandwidth of the Gaussian pulse is set to 1/3 octave band here (23%). Figure 8.2 is an example of the Gaussian pulse, i.e. $S^*(\omega)$ in eq.(8.1) at 200 kHz. The pulse has duration about 50 microseconds which is not very "short". This is due to the fact that the pulse should have finite length in order to have a narrow bandwidth.

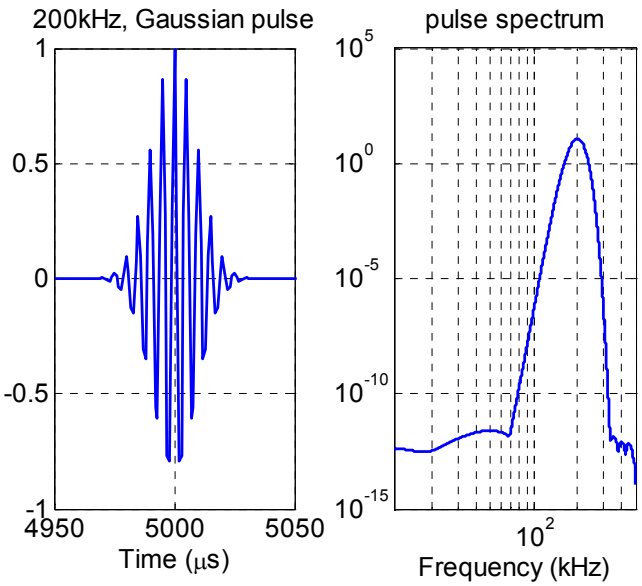

Figure 8.2 A Gaussian pulse used (left) and its spectrum (right).

8.1.3 Linear Frequency Modulated Signal

The transmitted signal, $S(\omega)$ in eq.(8.1) is a linear frequency modulated (LFM) chirp signal which has a bandwidth between 50 and 350 kHz:

$$s(t)=\sin\left[2\pi\left(f_1 t+\frac{f_2-f_1}{2\tau}t^2\right)\right] \tag{8.2}$$

where, f_2 and f_1 are high and low frequencies of the band, τ is pulse duration, and t is time.

For the tank experiment, pulse duration τ of 10ms is chosen and repeatedly transmitted. The received signal has the same duration of 10ms. Signal length, τ, is chosen to incorporate all the ringing of the tank, i.e. front and back reflections, until the amplitude of the reflected signal is negligible. The spectrum of the LFM chirp along with the spectrum of the Gaussian pulse is plotted in Figure 8.3.

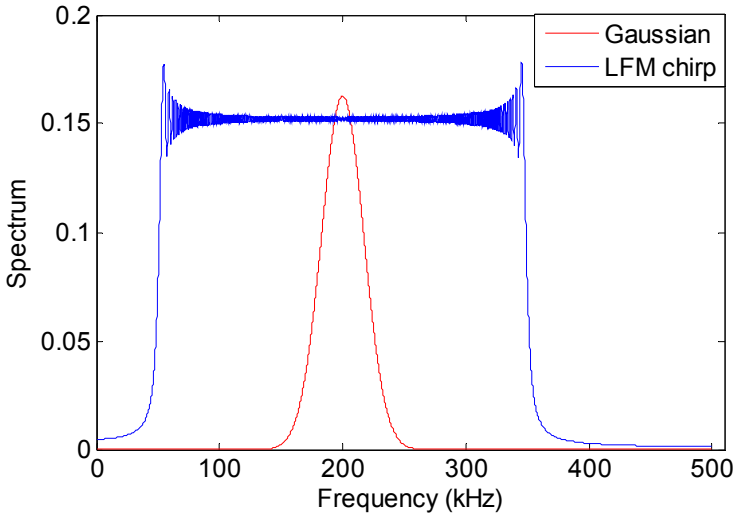

Figure 8.3 Transmitted LFM chirp signal and spectrum of a Gaussian pulse at 200 kHz.

8.2 Pekeris Waveguide Results

8.2.1 Data Processing

The tank experiment was done at room temperature. Water temperature, which is around 21^{o}C, was recorded simultaneously with the acoustic measurements. The tank was sampled longitudinally every 12cm and 1.2mm vertically. In total, 28x14 (depth x range) data points were recorded and each has a 10ms duration.

The transmitted signal, as mentioned in the previous session, is a wideband LFM chirp shown in Figure 8.2. The system response of a Gaussian pulse is then determined by taking the inverse Fourier transform of eq.(8.1). The 10ms time series of pulse compression result are plotted in Figures 8.4 and 8.5 at the shortest and longest distances. Each plot contains 28 depth samplings. Multiple reflections can be identified by their arrival times as marked on both figures.

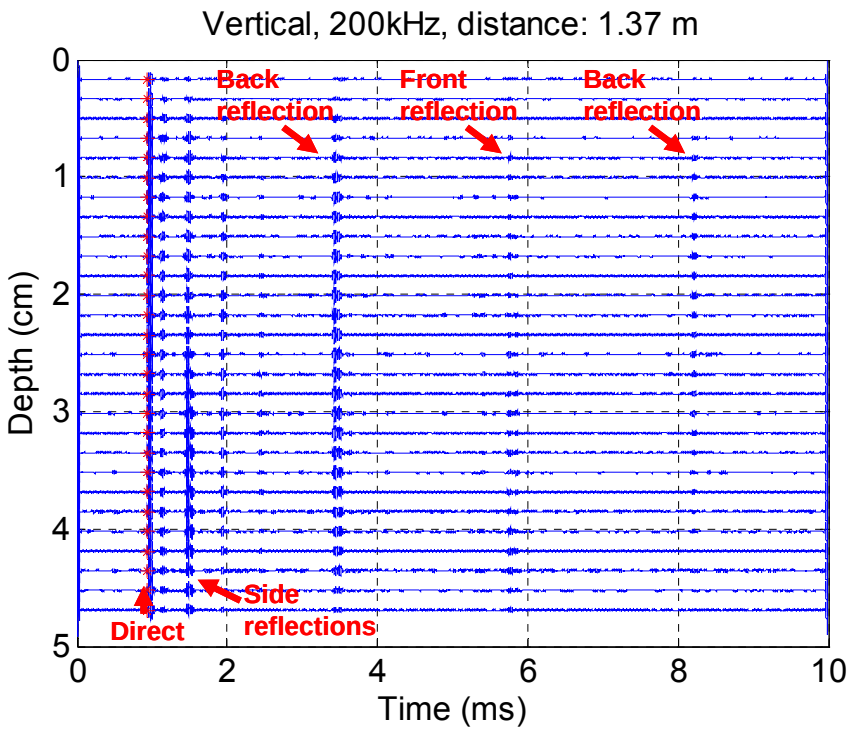

Figure 8.4 Time series of pulse compression results at the closest distance.

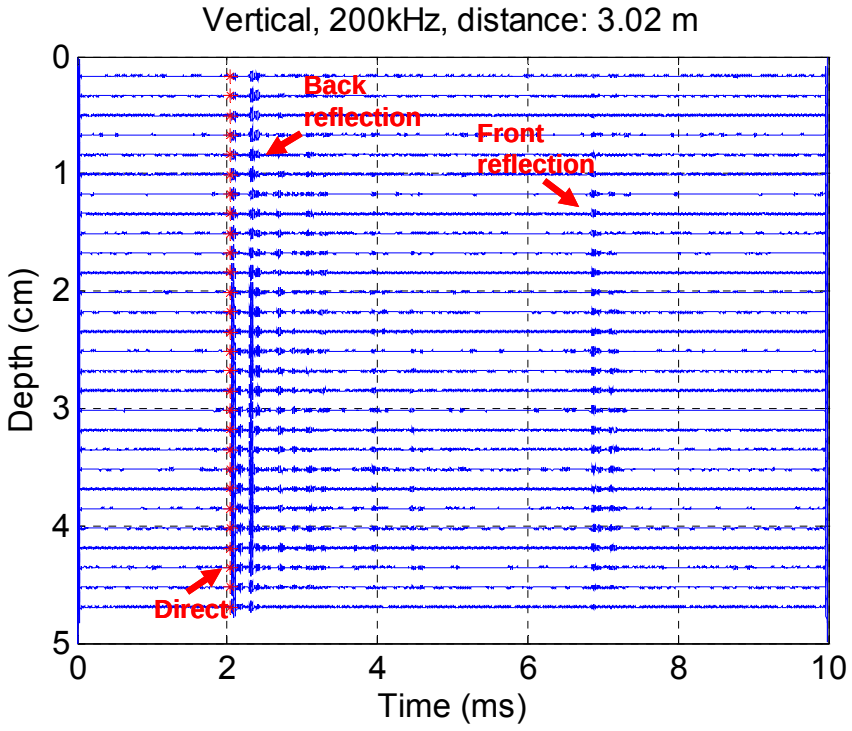

Figure 8.5 Time series of pulse compression results at the furthest distance.

The 10ms signal recorded as shown in Figures 8.4 and 8.5 contains acoustic signals of direct arrivals, multiple reflections, and scattering. To study sound propagation, we need to choose a time window with appropriate starting time and duration. Provided the Gaussian pulse is relatively narrow-banded, we will use the speed of sound in water to find the starting point. The time window is selected to be 100μs long to gate the closest arrival due to side reflection.

The truncated 100 μs time series are shown in Figures 8.6 to 8.7. At 200 kHz, the acoustic field starts with a total of 9 propagating modes. Since each of them has different group speed and amplitude, the resultant waveforms, as in Figure 8.6 and 8.7, is a combination of all of them. The longer tails indicates contribution from the higher order modes since they move slower. As range increases (Figure 8.7), the higher order modes will be attenuated out faster due to higher modal attenuations and the total signal amplitude keeps decreasing.

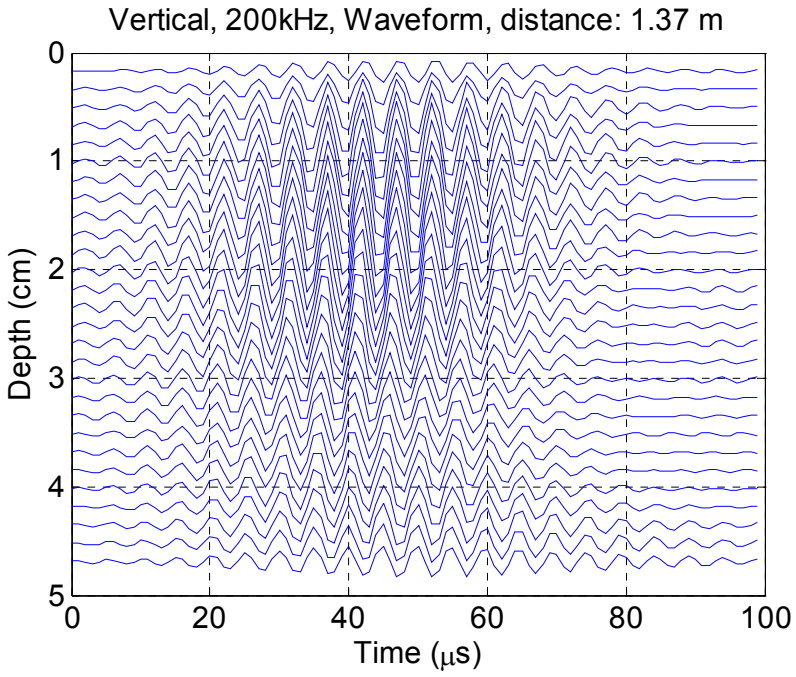

Figure 8.6 Gated signal with 100μs duration at the closest range.

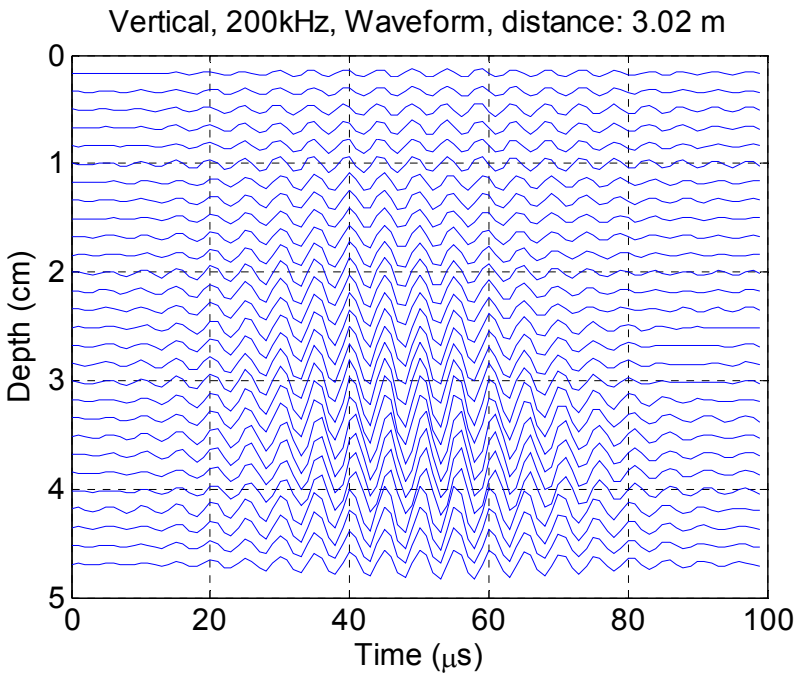

Figure 8.7 Gated signal with 100μs duration at the longest range.

8.2.2 Pressure Field

Using the truncated data, we can study the distribution of the mean-squared pressure field and transmission loss (TL) as a function of range. The transmission loss (TL), are computed using the logarithmic root-mean-squared (RMS) value of the truncated signals. It is interesting to plot the logarithmic mean-square pressure field at four different frequencies together (Figure 8.8). The color plots evidently show the interference pattern between modes. This is mainly due to the fact that there is limited number of modes. Among the four cases, 100 kHz has the fewest modes which is 5 while 250 kHz has 13. In addition, the rubber bottom has a rather large bottom loss which expedites the attenuation of higher order modes. As a result, the interference pattern looks like it is mainly between mode 1 and 2.

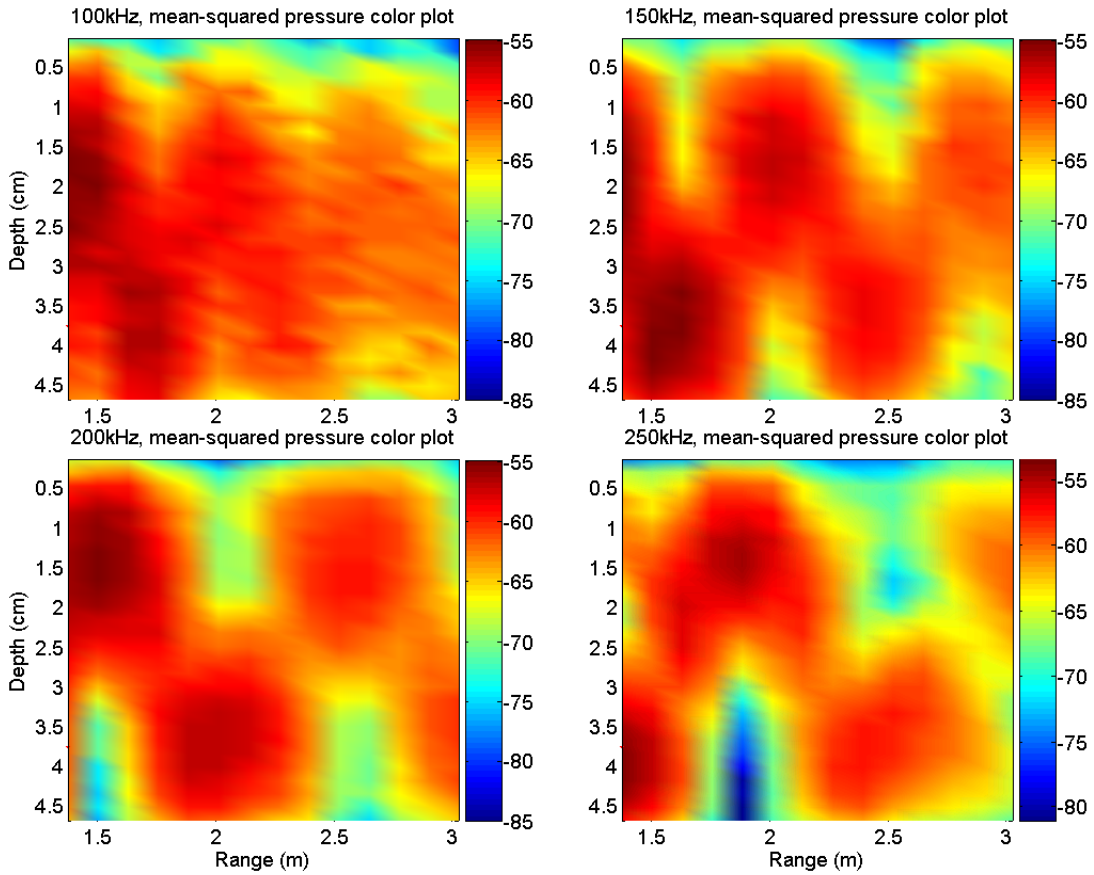

Figure 8.8 Logarithmic mean-squared pressure fields at four frequencies.

Normal mode theory is used to simulate sound propagation in the tank and compare with experimental data. Figure 8.9 shows the data/model comparison of coherent transmission loss (TL) which is defined in eq. (3.17). As a function of range, the TL curves in Figure 8.9 are from four different depths at 200 kHz. The results show a good match between experimental and theory though the fine structure of the latter is not well defined. This may be due to the finite-bandwidth signal used here while the theory simulates a single frequency (the center frequency). To explain the energy oscillation pattern in Figure 8.8, the color plots of the squared-pressure field are simulated using normal modes in Figure 8.10 for the same cases as 8.8. The model predictions are set to

the same scale as the experimental. It is apparent that the two figures show a good resemblance of each other.

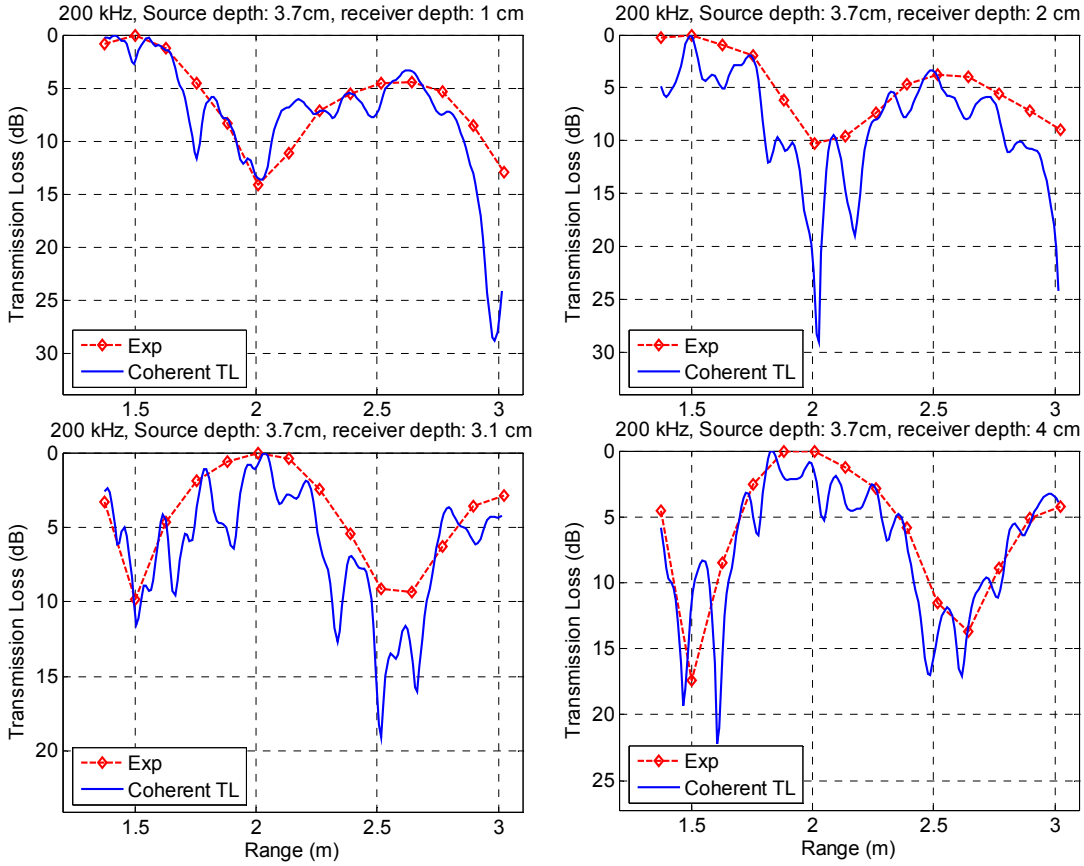

Figure 8.9 Comparison of transmission loss with theory at 200 kHz. (Bottom properties used are from the measurements in Chapter 2.)

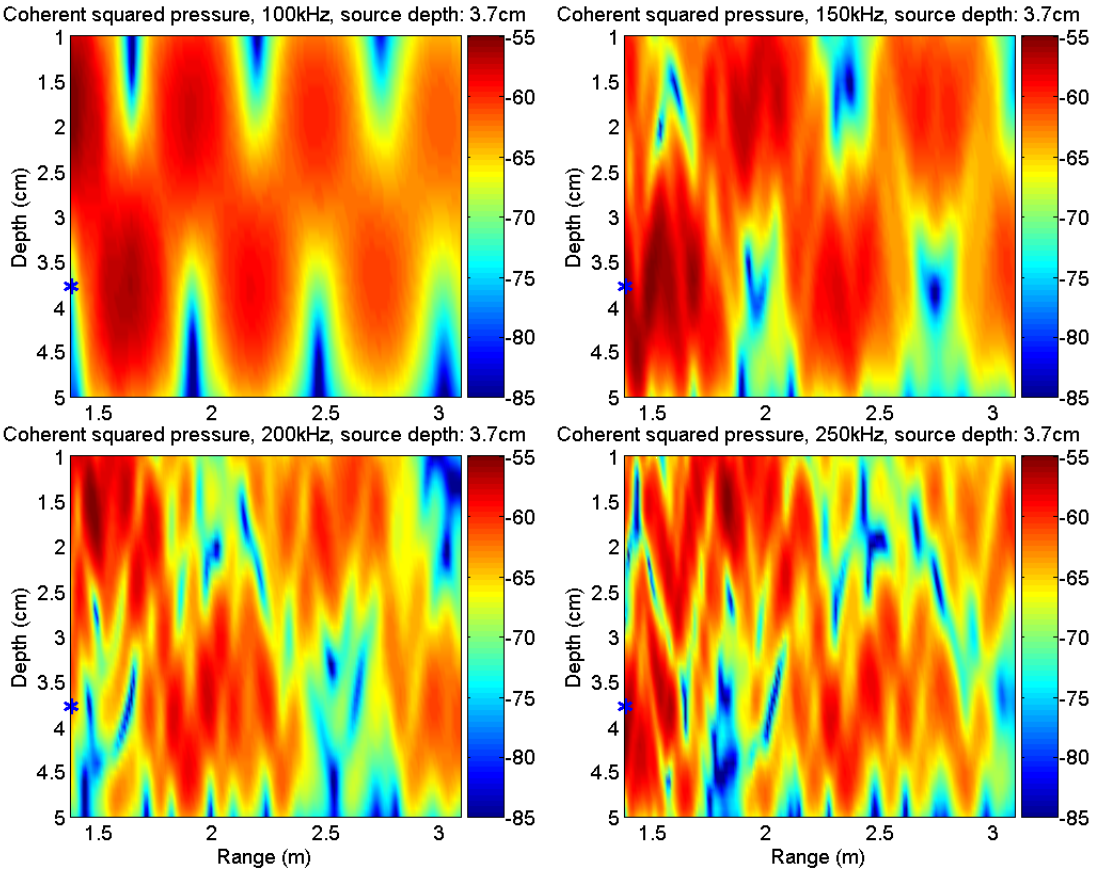

Figure 8.10 Predictions of squared-pressure field at four frequencies. (Bottom properties used are from the measurements in Chapter 2.)

8.2.3 Spatial Mode Filtering and Modal Attenuation Coefficients

One important aspect of the tank experiment is to study the propagation of each mode and use the modal attenuation coefficient as an inversion parameter. The spatial mode filtering method is applied here to separate each mode (Lo et al, 1983). The spatial mode filtering method is relatively simple. The first step is to find out all normal modes in the waveguide based on the experimental conditions such as water temperature, rubber sound speed, attenuation, and density. Then to filter a certain mode, the vertical time series of pressure samples are multiply-and-added by that mode shape which results in a time sequence of that mode. By repeating the above at all ranges, the decrease in modal

amplitude, i.e. the modal attenuation, can be found. Figure 8.11 shows the simulated mode shapes 1 to 3 based on experimental conditions. The filtered modes 1 and 2 at 100 and 200 kHz are plotted in Figure 8.12. Figure 8.13 and 8.14 show the filtered mode 1 and 2 as a function of range at 200 kHz. The range step here is 12.9cm.

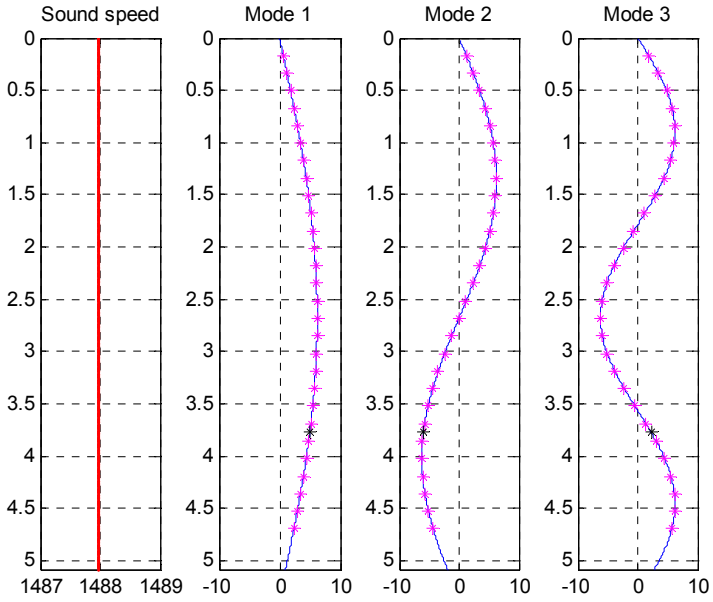

Figure 8.11 Numerical simulations of the first three normal modes at 22.1ºC. The magenta stars represent receiver depths; the black star indicates source depth.

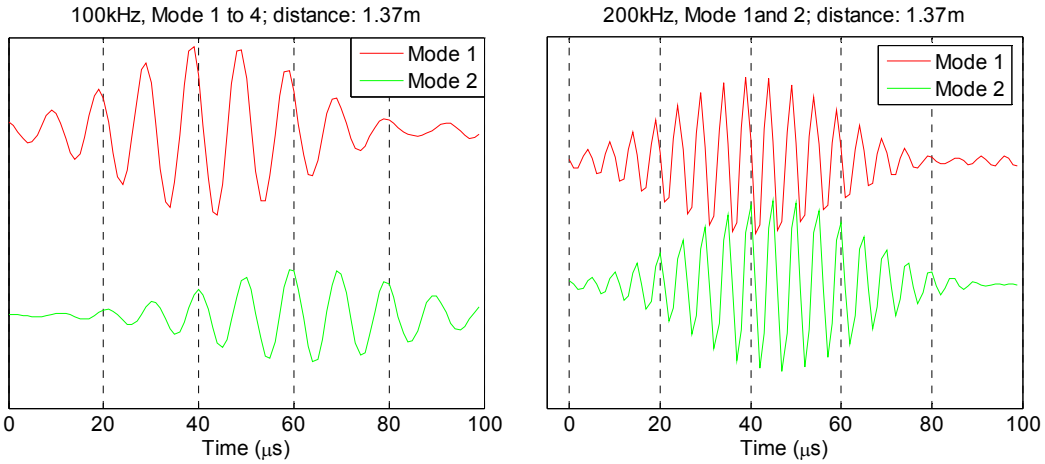

Figure 8.12 Spatially filtered modes 1 and 2 at 100 and 200 kHz.

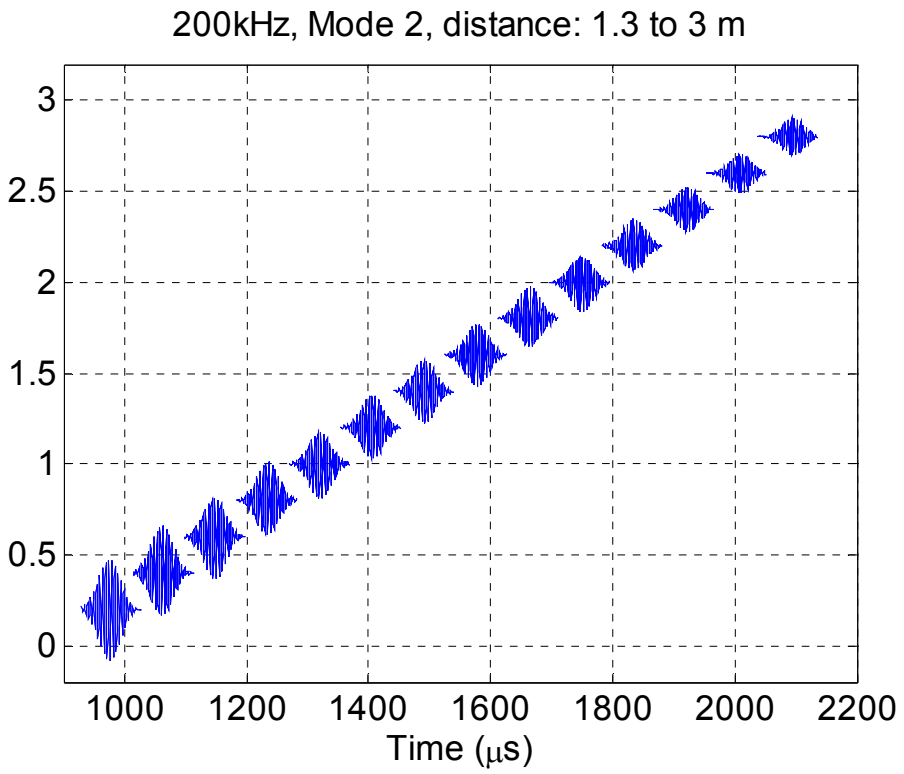

Figure 8.13 Spatially filtered mode 1 at 14 ranges, 200 kHz. Range step: 12.9cm

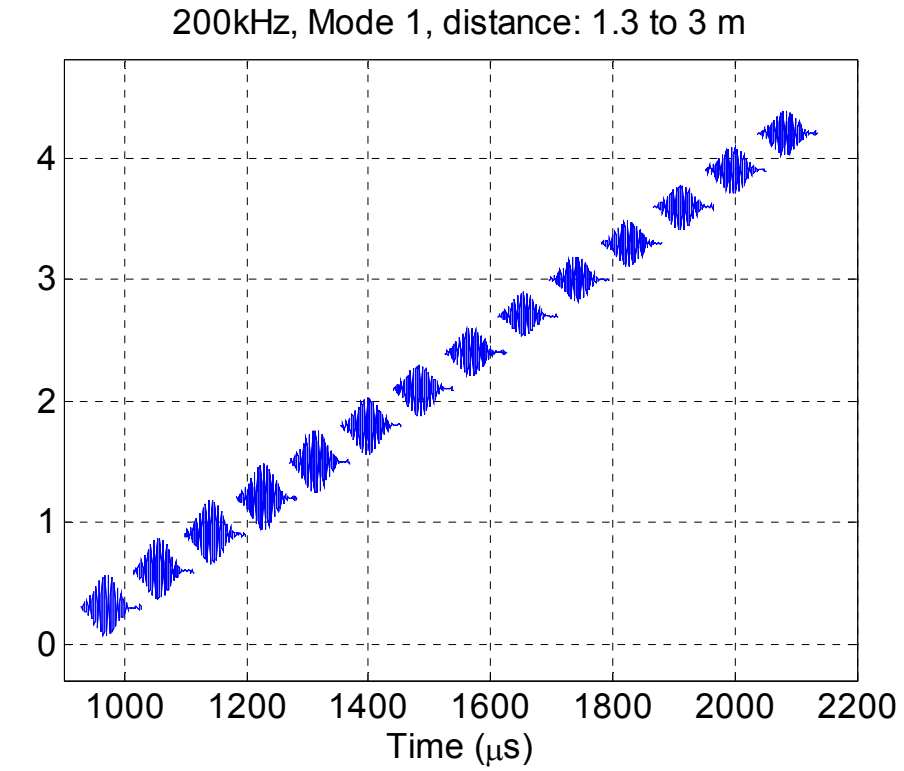

Figure 8.14 Spatially filtered mode 2 at 14 ranges, 200 kHz. Range step: 12.9cm

Finally, the modal amplitudes are found by integrating the filtered mode shapes. The normalized modal amplitudes are compared with theoretical modal attenuation coefficient. Two examples are included here: 100 and 200 kHz (Figures 8.15 and 8.16). The decrease in modal amplitude follows the theory closely. For 200 kHz, the oscillations in mode 1 and 2 indicate mode coupling between them.

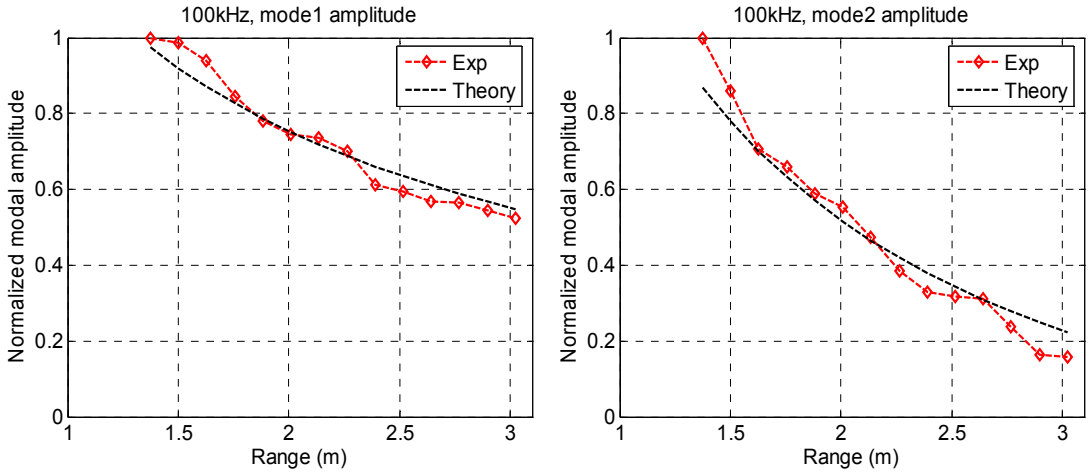

Figure 8.15 Comparison of theoretical and experimental modal attenuations at 100 kHz. (Bottom properties used are from the measurements in Chapter 2.)

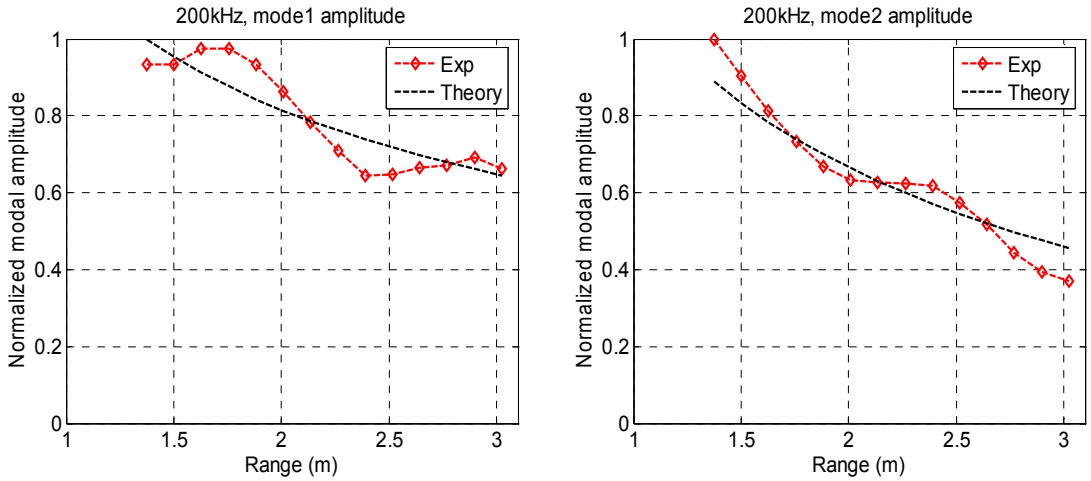

Figure 8.16 Comparison of theoretical and experimental modal attenuations at 200 kHz. (Bottom properties used are from the measurements in Chapter 2.)

8.3 Vertical Coherence Results

8.3.1 Vertical *kd*-Plot

Vertical coherence results here are referred to as the cross-correlation coefficient between two depth samples at the same range. As mentioned earlier, there are a total of 28 depth samples (each 100μs long) at every range. To avoid complexity due to boundaries, we only took 16 depth measurements centered in the middle of the water column. Since the water column is evenly sampled vertically (stepsize dz = 1.2mm), there are 15 cross-correlation coefficients with minimum separation dz and only 1 with maximum separation 15*dz. The vertical coherence results are assembled together for the *kd*-plot in Figures 8.17 and 8.18 at four different distances.

There are several interesting features in these two figures. First, for both 100 and 200 kHz cases, the cross-correlation coefficient is increasing with range. Second, at the same distance, the cross-correlation decreases with increasing frequency. Third, the vertical cross-correlation length, defined as cross-correlation drops to 1/*e*, is around 2λ at 200 kHz. All above observations are consistent with the characteristics analysis in Chapter 4.

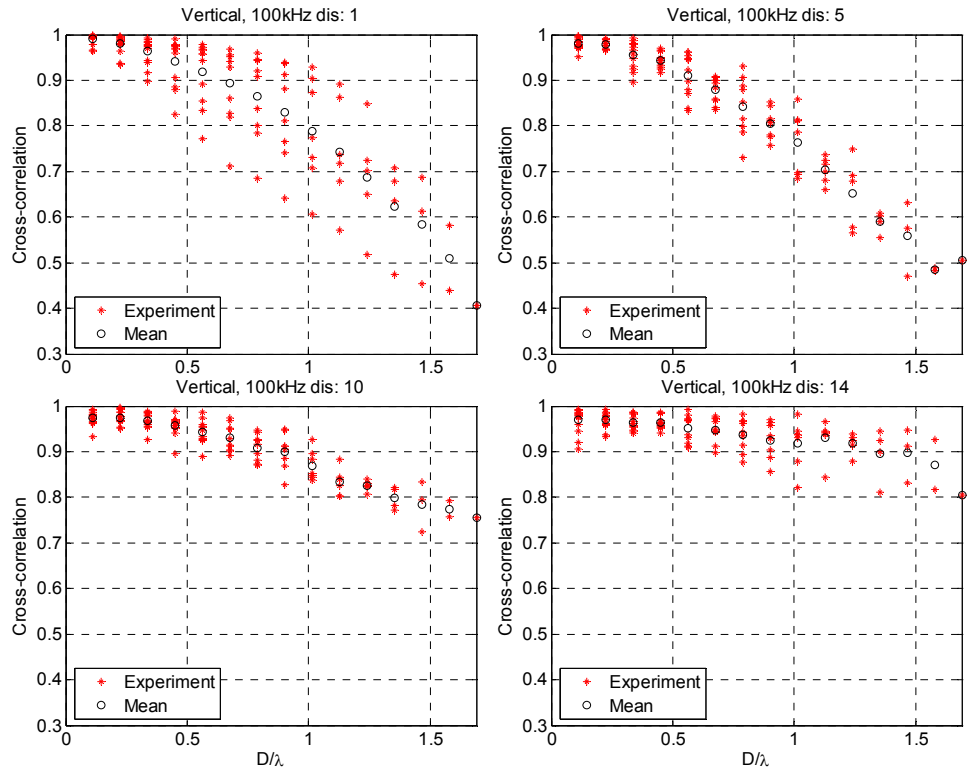

Figure 8.17 Vertical D/λ plot at four ranges, 100 kHz.
Red stars: experimental results; black circles: average value.

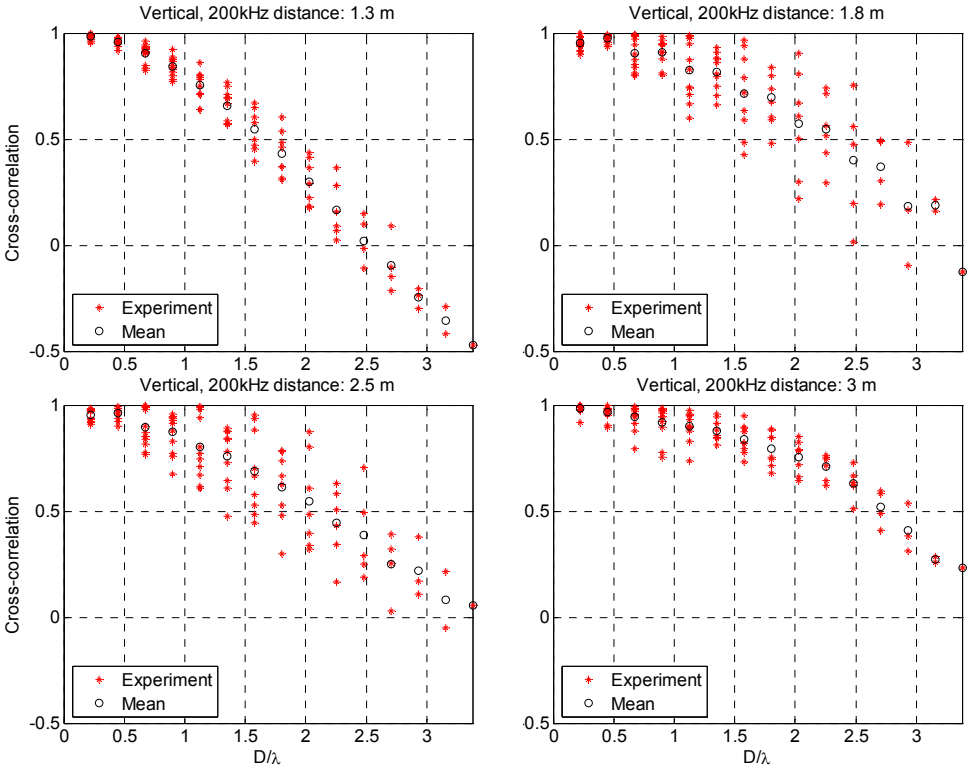

Figure 8.18 Vertical D/λ plot at four ranges, 200 kHz.
Red stars: experimental results; black circles: average value.

8.3.2 Range Dependence of Vertical Coherence

In Chapter 4, the dependence of vertical coherence on various parameters such as frequency, separation, and range has been presented using *in-situ* measurements. Similar characteristics have been observed through the tank experiments.

Figure 8.19 shows two cases: 100 and 200 kHz. For each case, vertical coherence is increasing with range while decreasing with bigger separation. For fixed separations, Figure 8.20, vertical coherence decreases with increasing frequency. The experimental data shown here have considerable fluctuations around the average curves especially when frequency goes beyond 150 kHz. This is due to the interference of different modes. The interference pattern also contains sediment information. In the following section, the vertical coherence data will be used to invert the rubber properties and results will be compared with previous measurements of rubber properties.

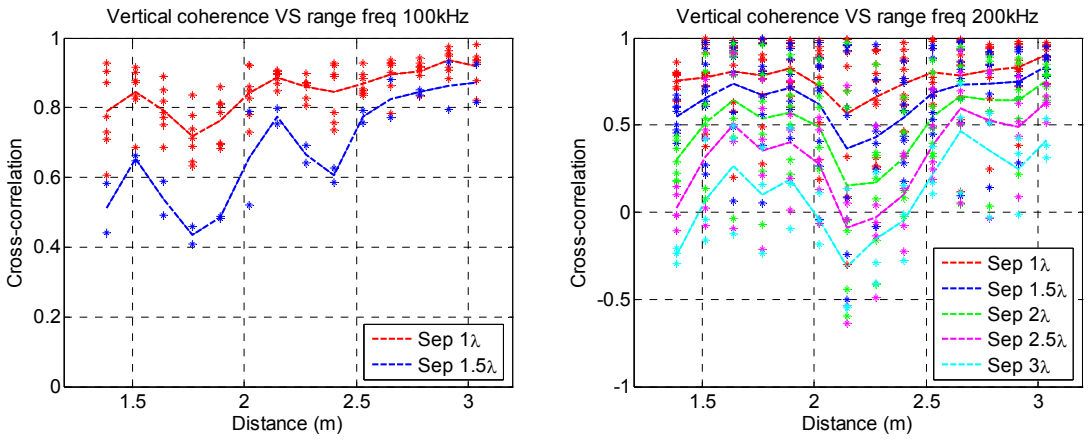

Figure 8.19 Vertical coherence versus range and separation.
Stars: experimental data; dashed lines: average.

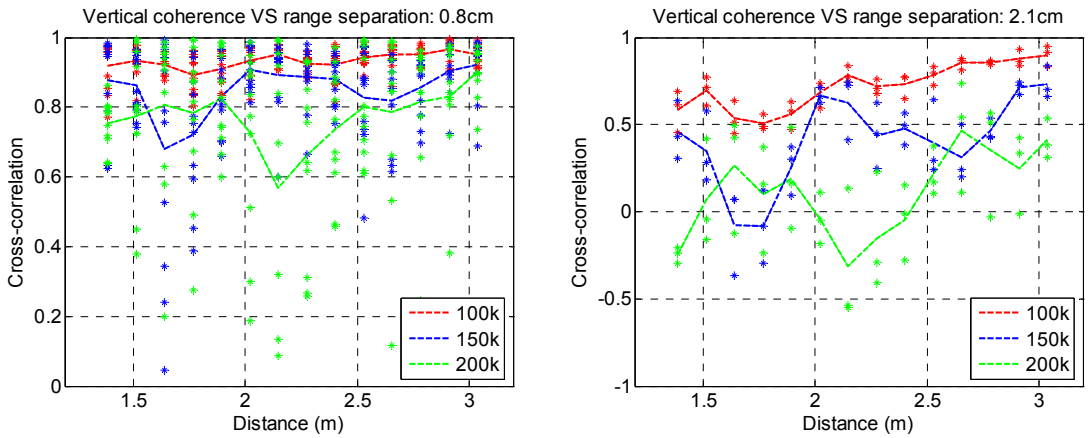

Figure 8.20 Vertical coherence versus frequency, range and separation.
Stars: experimental data; dashed lines: average.

8.3.3 Inversion Results

The inversion scheme used here is different from Chapter 5. The theoretical expression for vertical coherence can be written as:

$$\begin{aligned}\gamma &= P(r,z)P^{*}(r,z+d_v) \\ &= \frac{1}{8\pi r\rho(z_s)}\sum_{m=n}\left|\Psi_m(z_s)\right|^2\Psi_m(z)\Psi_m{}^{*}(z+d_V)\frac{e^{-2\alpha_m r}}{k_{rm}}+ \\ &\sum_{m\neq n}\Psi_m(z_s)\Psi_m(z)\Psi_n^{*}(z_s)\Psi_n^{*}(z+d_V)\frac{e^{i(k_{rm}-k_{rn})r}e^{-(\alpha_m+\alpha_n)r}}{\sqrt{k_{rm}k_{rn}}}\end{aligned} \tag{8.3}$$

There are two terms in this definition and they are referred to as the incoherent and coherent components of vertical coherence. In Chapter 5, only the first term is kept based on the assumption that there is enough number of modes to make the summation of the second term negligible due to $e^{i(k_{rm}-k_{rn})r}$. For the tank experiment, strong interference pattern has been observed. Therefore, both terms are included in the inversion scheme. The criterion is the same as in Chapter 5, i.e. finding sediment sound speed and attenuation by the minimum squared error between experimental and model.

The comparison between experimental and theoretical vertical coherence using inverted parameters are compiled in Figures 8.21-8.23. (Note, *dz* is 1.2 mm.) Figures 8.21 and 8.22 show similar data/model comparison at two different frequencies. For both cases, the fluctuation in coherence increases with separation; the inverted coherence shows fine predictions of the experiment. As frequency increases, it is observed that the inversion results may be less reliable due to the decrease in coherence and increase in fluctuation. Figure 8.23 shows an example. For the same separation, the match between inverted and experimental coherence gets worse although the inverted curve is still able to catch the main features (200 kHz in this case).

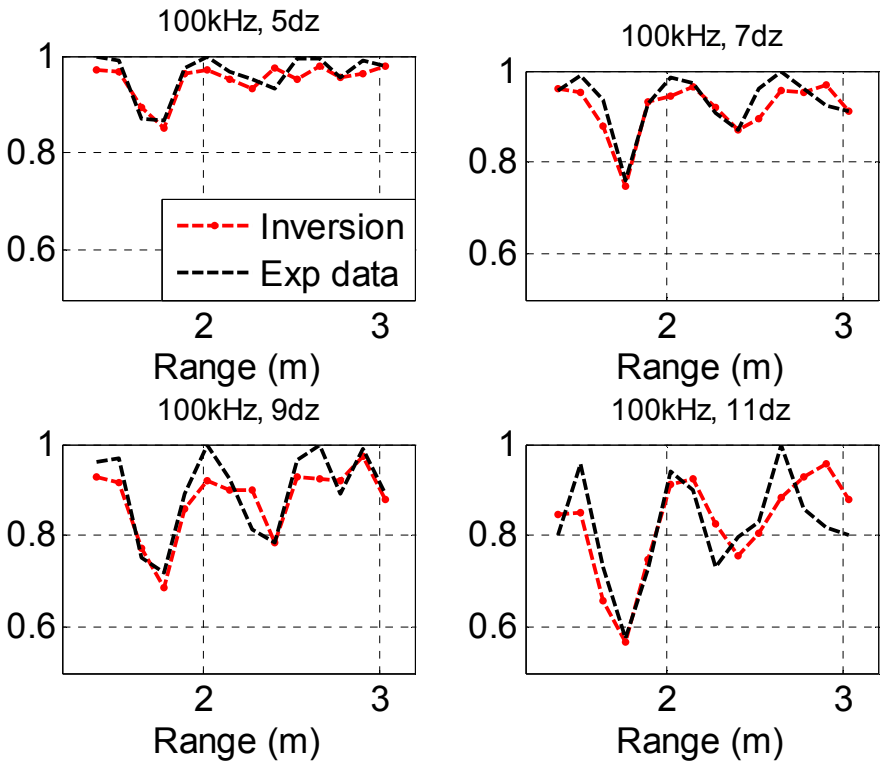

Figure 8.21 Comparison of experimental and inverted coherence at 100 kHz.

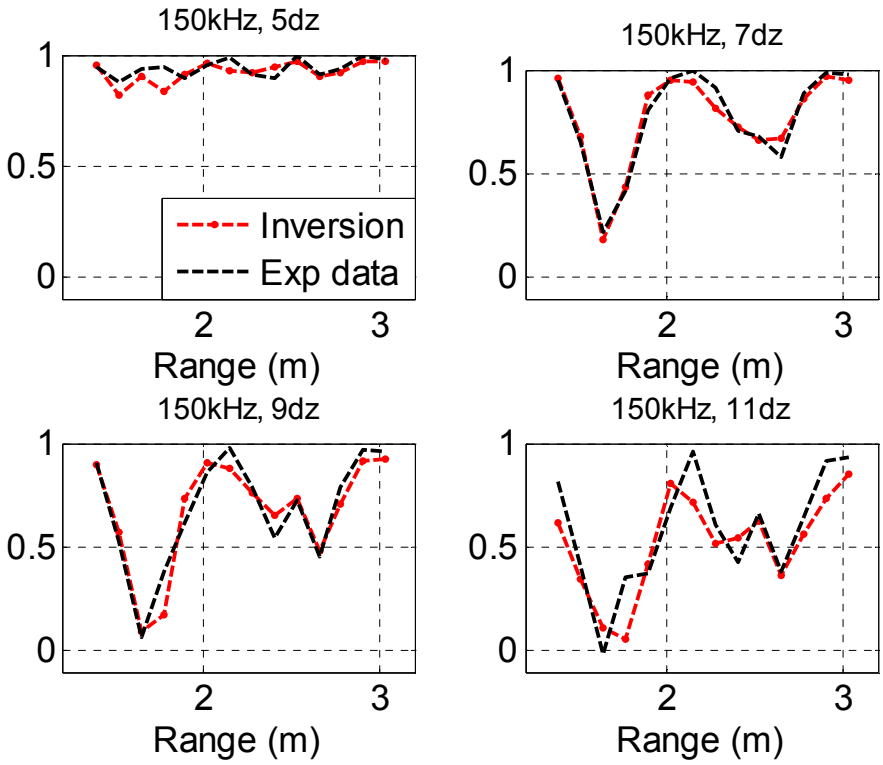

Figure 8.22 Comparison of experimental and inverted coherence at 150 kHz.

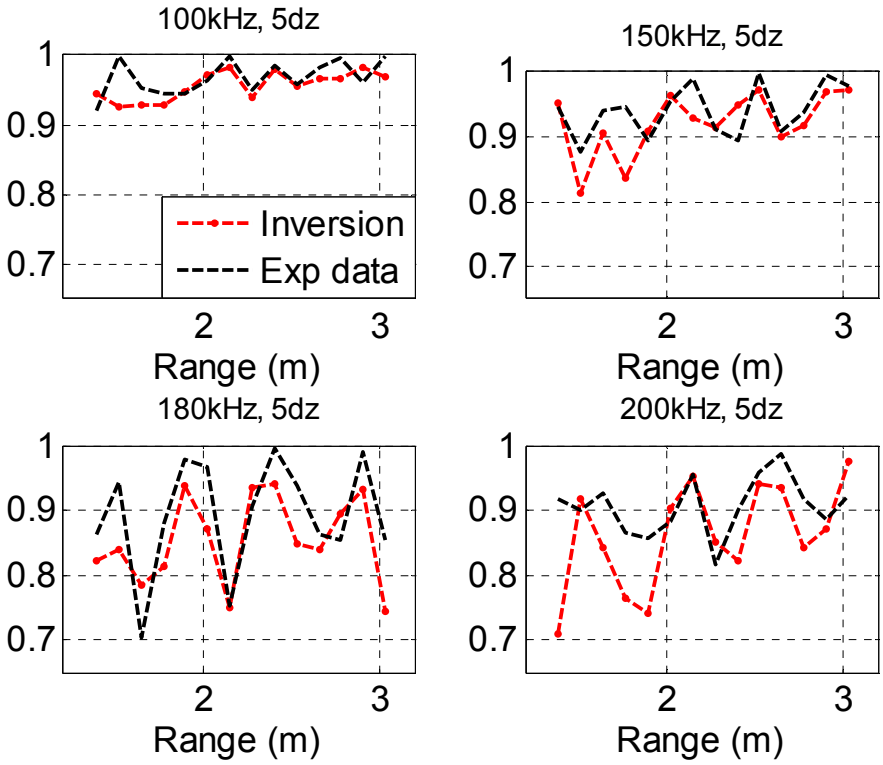

Figure 8.23 Comparison of experimental and inverted coherence with fixed separation.

The inverted sediment or rubber sound speed and attenuation are plotted in Figures 8.24 and 8.25. There is no obvious frequency dependence of sediment sound speed. The overall average sound speed is 1641.6 m/s. The inverted attenuation shows frequency dependence as $\alpha = 0.002 \times f^{2.23}$.

The comparison between rubber property measurements and inversion results (Figures 2.17 and 2.20) show considerable difference in both sound speed and attenuation especially the former. The discrepancy may be due to a couple of reasons. First, measurements show that the rubber sound speed is anisotropic. With the rubber sample perpendicular or parallel to the acoustic field, the sound speed can change from 1580 to 1840 m/s respectively. Plus, there may be inhomogeneities in the rubber sheet. Second, for the measurements, the sound field goes through two acoustic transmissions from the source to the receiver, which may result in a bigger attenuation.

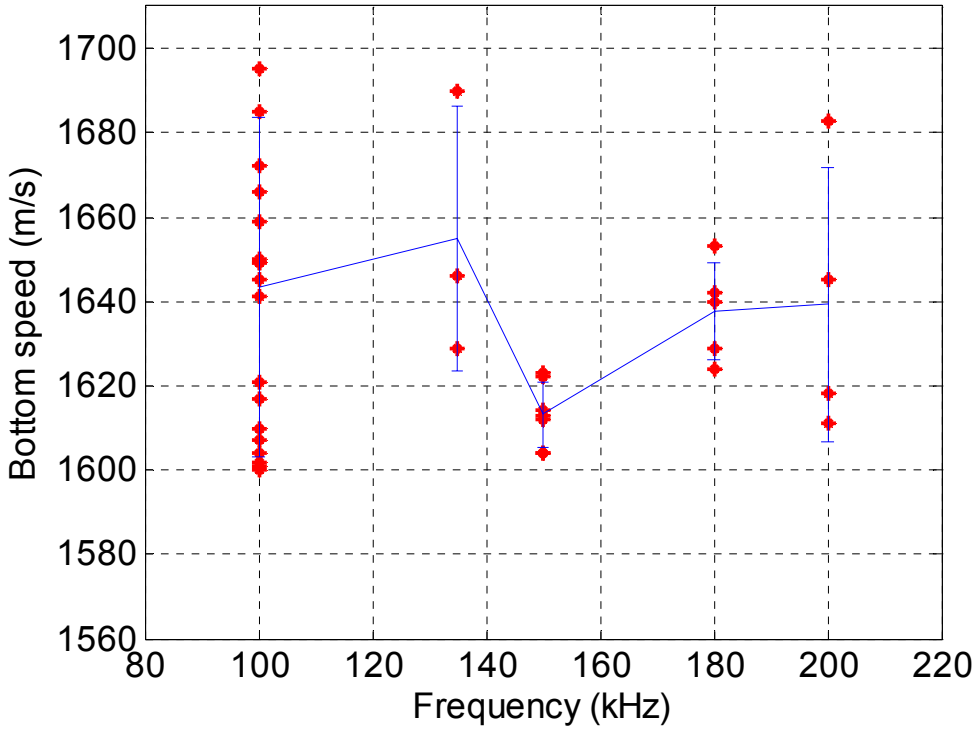

Figure 8.24 Inverted bottom sound speeds at different frequencies.

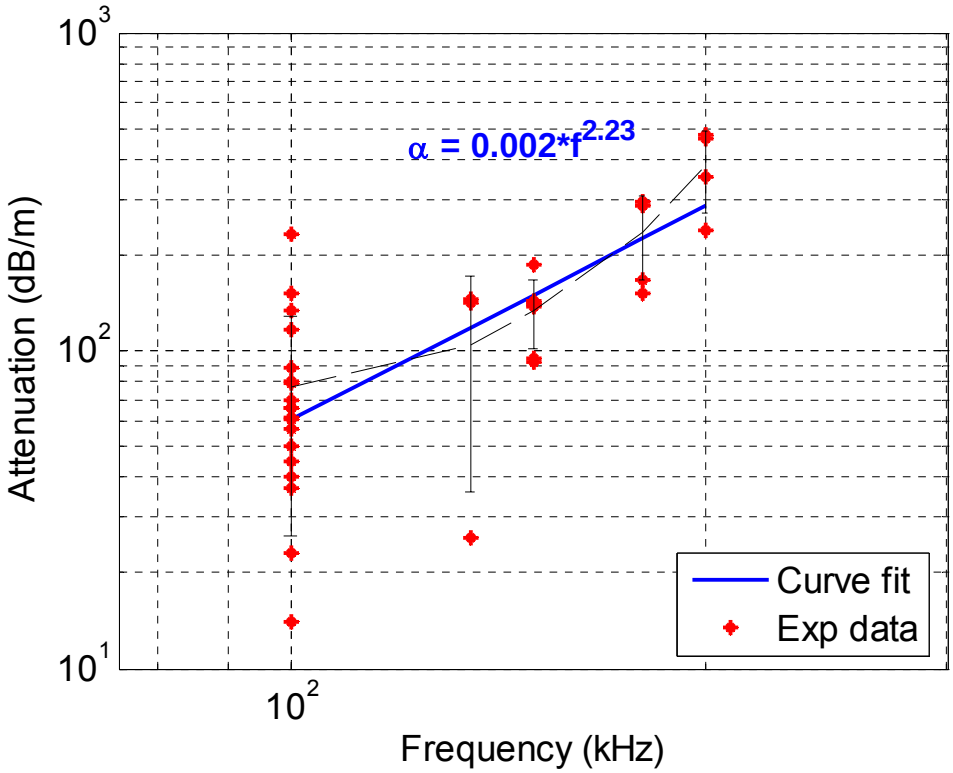

Figure 8.25 Inverted bottom attenuations at different frequencies.

CHAPTER 9

CONCLUSIONS AND FUTURE DIRECTIONS

The challenge of sound propagation in a shallow water region primarily comes from the complexity of the environment. Therefore, it is important to study characteristics of the environmental parameters and how they affect sound propagation.

The ASIAEX experiment conducted in the ECS provided a unique data set for this research. In this thesis, the *in-situ* acoustic data were analyzed to show the characteristics of vertical coherence in a shallow water waveguide. Combined with simultaneous oceanographic data, the vertical coherence was used as an inversion parameter to extract geoacoustic information of the sediment.

One of the environmental factors examined is the internal waves. The 63-hour temperature history from the GT 17-element thermistor array was investigated to show the characteristics of internal wave spectrum in shallow water. Strong internal tidal waves and non-linear high frequency wave packets were observed. Two acoustic models were used to explain the abnormal change in vertical coherence data on the path of the internal waves. The first is to model the sound speed variations induced by the internal waves as a random process. The variations were calculated from the internal wave spectrum. This model failed to explain the acoustic data. The second model involved propagating the 63-hour temperature series into a spatial distribution. The modeling results that the long-period internal tides, causing the thermocline to move between 35~65m, are responsible for the change in coherence data.

Another environmental descriptor studied is the wind-generated surface waves. The characteristics of the wind-generated surface waves were presented using the 9-day record of wind velocity and directional surface wave spectrum. The comparison between two data sets showed an increase in coherence at a higher sea state, i.e. higher wind speed. Acoustic model was built to include surface waveheights, generated from the surface wave spectrum as a random process, as the top boundary of the waveguide. The model shows good prediction of vertical coherence.

Finally, a tank experiment was carried out to study sound propagation in a homogeneous waveguide. A sheet of rubber was chosen as the bottom. Using the pulse compression technique, the acoustic field recorded showed strong interference pattern. The vertical coherence and interference pattern were used as inversion parameters to find the rubber sound speed and attenuation. The inverted results of the rubber were compared with measurements carried out in the lab. It was believed that the discrepancies were due to the anisotropic properties of the rubber.

9.1 Contributions

The major contributions of this dissertation are summarized below:

- A systematic presentation of the characteristics of vertical coherence for long range sound propagation in a shallow water waveguide.
- A study of environmental phenomena particularly internal waves and wind-generated surface waves: their statistical characterization, and the spatial and temporal variations which they induce on the acoustic field.
- A method and results for obtaining sediment geoacoustic properties by inversion of *in situ* vertical coherence data.

- Development of a range dependent acoustic model which simulates environmental effects from internal waves and surface waves. The model was validated by comparing with at-sea coherence data which exhibited effects attributable to the influence of internal waves and surface waves.
- Development of a 1/1000 scale experiment model for sound propagation in a simulated Pekeris waveguide. The modal interference pattern and vertical coherence were used as inversion parameters for determining bottom speed and attenuation.

9.2 Future directions

Although we have presented the characteristics and some of the environmental effects on vertical coherence of sound propagation, there are still many more research issues to be investigated. Specifically, some of the future research topics are listed as follows:

- **Relative importance of environmental parameters on sound propagation.** In this dissertation, various environmental effects are examined separately while they should be studied together. Thus, it would be helpful to determine the relative importance of the various environmental parameters to predictions of propagation and reverberation for different frequency bands and geometries.
- **Cotinuation of the tank experiment.** The tank experiment here, though showing excellent agreement with the theory, is a simple Pekeris waveguide problem. One future direction is to improve the tank experiment by including the surface roughness and the internal waves. Therefore, their separate and coupled acoustic effects can be studied at a greater detail compared with at-sea experiment.

The ASIAEX data are limited in both acoustic and oceanographic aspects. The following future research topics would rely on the data from a recent sea experiment (Shallow Water 06) conducted in New Jersey Bay.

- **Geoacoustic properties of the sediments.** Due to the difficulty of direct measurement, considerable effort has been put into developing inversion techniques. As discussed earlier, the coupling between sediment sound speed and attenuation remains an issue. One future research goal is to use localized sediment ground truth measurements to calibrate chirp sonars inversion results and then use the chirp sonar measurements to infer geoacoustic information for the sediment.
- **The 3-dimensional internal wave field and its acoustical effects.** In this thesis, we proposed a rather simplified model for the internal wave field by propagating the temperature time series. However, the internal wave field may change direction and strength. Therefore, another interesting future work would be to study the generation and evolution of the 3-dimensional internal wave field and determine the anisotropic acoustic effects.

REFERENCES

Allender, J. H., J. Albrecht, and G. Hamilton, "Observations of directional relaxation of wind sea spectra," J. Phys. Oceanogr., 13, 1519-1525, 1983.

Apel, John R., Mohsen Badiey, C-S Chiu, Steven Finette, Robert Headrick, John Kemp, James F. Lynch, Arthur Newhall, Marshall H. Orr, Bruce H. Pasewark, Dirk Tielbuerger, Altan Turgut, Keith von der Heydt, and Stephen Wolf, "An overview of the 1995 SWARM Shallow-Water Internal Wave Acoustic Scattering Experiment," IEEE J. Oceanic Eng., V 22(3), 465-500, 1997.

Apel, John R., *Principles of Ocean Physics*, Academic Press, 1987.

Bachmann, W., "A theoretical model for the backscattering strength of a composite roughness sea," Acoust. Soc. Am., V54, 712-716, 1973.

Baines, P. G., "The generation of internal tides by flat-bump topography," Deep Sea Res., 20, 179-205, 1973.

Baines, P. G., "The generation of internal tides over steep continental slopes," Philos. Trans. R. Soc. London, Ser. A, 277, 27-58, 1974.

Beckmann, P. and A. Spizzichino, *The Scattering of Electromagnetic Waves from Rough Surfaces*, Macmillan, New York, 1963.

Biot, M. A., "Theory of Propagation of Elastic Waves in a Fluid-Saturated Porous Solid. I. Low-Frequency Range," J. Acoust. Soc. Am., V28, 168-178, 1956.

Biot, M. A., "Theory of Propagation of Elastic Waves in a Fluid-Saturated Porous Solid. II. High-Frequency Range," J. Acoust. Soc. Am., V28, 178-191, 1956.

Biot, M. A., "Generalized Theory of Acoustic Propagation Porous Media," J. Acoust. Soc. Am., V34, 1254-1264, 1962.

Boyd, M. L., and R. L. Deavenport, "Forward and specular scattering from a rough surface: theory and experiment,"J. Acoust. Soc. Am., V53, 791-801, 1973.

Brekhovshikh, L. M. and Yu P. Lysanov, *Fundamentals of Ocean Acoustics*, Springer-Verlag, NY, 2003.

Broek, H. W., and C. Tom, "Spatial Coherence of Multipath Underwater Acoustic Transmission: An Experiment at two frequencies concurrently," J. Acoust. Soc. Am., V75, 395-405, 1984.

Buckingham, M. J., "A Theoretical Model of Ambient Noise in a Low-Loss Shallow Water Channel," J. Acoust. Soc. Am., V67, 1186-1192, 1980.

Buckingham, M. J., "Spatial Coherence of Wind-Generated Noise in a Shallow Ocean Channel," J. Acoust. Soc. Am., V70, 1412-1420, 1981.

Buckingham, Michael J., John R. Potter, and G. B. Deane, "Spatial Coherence of High Frequency (67KHz) Acoustic Fluctuations in Fully Developed Turbulence," J. Acoust. Soc. Am., V96, 3287, 1994.

Cairns, J. L., "Asymmetry of internal tidal waves in shallow coastal waters," J. Geophys. Res., 72(14), 3563-3565, 1967.

Caruthers, Jerald W., and Michael F. Werby, "Forward Scatter and Signal Coherence in Shallow Water," J. Acoust. Soc. Am., V93, 2270, 1993.

Chapman, D. M. F., and D. D. Ellis, "The group velocity of normal modes," J. Acoust. Soc. Am., V74, 973-979, 1983.

Clay, C. S., "Effect of a slightly irregular boundary on the coherence of waveguide propagation," J. Acoust. Soc. Am., V36, 833-837, 1964.

Clay, C. S., H. Medwin, and W. M. Wright, "Specularly scattered sound and the probability density function of a rough surface," J. Acoust. Soc. Am., V53, 1677-1682, 1973.

Clay, C. S. and Kung Huang, "Single mode transmission and acoustic backscattering measurements in a laboratory waveguide," J. Acoust. Soc. Am., V67, 792-794, 1980.

Clay, C. S., Y-Y. Wang, and E.-C. Shang, "Sound field fluctuations in a shallow water waveguide," J. Acoust. Soc. Am., V77, 424-428, 1985.

Collins, M. D., "A split-step Padé solution for the parabolic equation method," J. Acoust. Soc. Am., V93, 1736-1742, 1993.

Collins, M. D., R. J. Cederberg, D. B. King, and S. A. Chin-Bing, "Comparison of algorithms for solving parabolic wave equations," J. Acoust. Soc. Am., V100, 178-182, 1996.

Colosi, J. A., R. C. Beardsley, J. F. Lynch et al, "Observations of nonlinear internal waves on the outer new England continental shelf during the summer Shelfbreak Primer study," J. of Geophys. Res., 106(C5), 9587-9601, 2001.

Collins, M. D., "A split-step Padé solution for parabolic equation method," J. Acoust. Soc. Am. 93, 1736-1742, 1993.

Dahl[1], Peter H., R. Zhang, J. H. Miller, L. R. Bartek, Z. Peng, S. R. Ramp, J-X Zhou, C-S Chiu, and J. F. Lynch, "Overview of Results From the Asian Seas International Acoustics Experiment in the East China Sea," IEEE J. Oceanic Eng., V29, No.4, 920-928, 2004.

Dahl[2], Peter H., "Forward scattering from the sea surface and the van Cittert–Zernike theorem," J. Acoust. Soc. Am. V115, 589-599, 2004.

Dewitt, L. M., M. D. Levine, C. A. Paulson, and W. V. Burt, "Semidiurnal internal tide in JASIN: observations and simulation," J. of Geophys. Res., 91(C2), 2581-2592, 1986.

Dozier, L. B., "PERUSE: A numerical treatment of rough surface scattering for the parabolic wave equation," J. Acoust. Soc. Am., V75, 1415-1432, 1984.

Eckart, Carl, "The scattering of sound from sea surface," J. Acoust. Soc. Am., V25, 566-570, 1953.

Ellis, D. D., "A shallow-water normal-mode reverberation model," J. Acoust. Soc. Am., V97, 2804-2814, 1995.

Lo En-Cen, Ji-Xun Zhou, Er-Chang Shang, "Normal mode filtering in shallow water," J. Acoust. Soc. Am., V74, 1833-1836, 1983.

Duda, Timothy and James C. Preisig, "A modeling study of acoustic propagation through moving shallow water solitary wave packets," IEEE J. Oceanic Eng., V24, 16-26, 1999.

Finette, Steven, Marshall H. Orr, Altan Turgut, John R. Apel, Mohsen Badiey, Ching-sang Chiu, Robert H. Headrick, John N. Kemp, James F. Lynch, Arthur E. Newhall, Bruce Pasewark, Stephen N. Wolf, and Dirk Tielbürger, "Acoustic Field Variability Induced by Time Evolving Internal Wave Fields," J. Acoust. Soc. Am., V108, 957-972, 2000.

Fitelson, M. M., "Coherence Function for Cylindrically Spreading Waves in a Random Medium," J. Acoust. Soc. Am., V56, 53-57, 1974.

Flatté, S. M., R. Dashen, W. H. Munk, K. M. Watson, and F. Zachariasen, *Sound Transmission Through a Fluctuating Ocean*, Cambridge U.P., Cambridge, 1979.

Flatté, S. M., and G. Rovner, "Calculations of internal-wave-induced fluctuations in ocean-Acoustic propagation," J. Acoust. Soc. Am., V108, 526-534, 2000.

Fortuin, Leonard, "Survey of literature on reflection and scattering of sound waves at the sea surface," J. Acoust. Soc. Am., V47, 1209-1228, 1970.

Funk, D. E., and K. L. Williams, "A physically motivated simulation technique for high-frequency forward scattering derived using specular point theory," J. Acoust. Soc. Am., V91, 2606-2614, 1992.

Galybin, N. N., "Backscattering of sound by a disturbed sea surface," Sov. Phys. Acoust., V22, 193-197, 1976.

Garret, Christopher, and Walter Munk, "Space-time scales of internal waves," Geophys. Fluid Dyn., V2, 225-264, 1972.

Garret, Christopher, and Walter Munk, "Space-time Scales of Internal Waves: A Progress Report," J. Geophys. Res., 80(3), 291-299, 1975.

Gazanhes[1], C., J. P. Sessarego and J. L. Garnier, "Identification of modes in some conditions of sound propagation in shallow water," J. Sound Vib., V56(2), 251-259, 1978.

Gazanhes[2], C., J. Leandre, and J. P. Lefebvre, "Spectral structure of an ultrasound wave scattered by a random surface: Application to the scattering of sound from the sea surface," J. Acoust. Soc. Am., V63, 1347-1352, 1978.

Gazanhes, C., and J. L. Garnier, "Experiments on Single Mode Excitation in Shallow Water Propagation," J. Acoust. Soc. Am., V69, 963-969, 1981.

Gazanhes, C., J. L. Garnier, and J. P. Sessarego, "Computer simulation of Spatial Filtering of Modes by Vertical Array Steering and Double Symmetrical Angles of Sight in Shallow Water Propagation," J. Sound Vib., V94(2), 205-216, 1984.

Halpern, D., "Semidiurnal internal tides in Massachusetts Bay," J. Geophys. Res., 76(27), 6573-6584, 1971.

Hamilton, E. L., "Geoacoustic models of the sea floor," In *Physics of Sound in Marine Sediments*, edited by L. Hampton. Plenum, NY, 181-221, 1974.

Hamilton, E. L., "Sound attenuation as a function of depth in the sea floor," J. Acoust. Soc. Am., V59, 528-535, 1976.

Hamilton, E. L., "Geoacoustic modeling of the sea floor," J. Acoust. Soc. Am., V68, 1313-1339, 1980.

Hardin, R. H., and F. D. Tappert, "Applications of the split-step Fourier method to the numerical solution of nonlinear and variable coefficient wave equations," SIAM Rev., 15, 423, 1973.

Hasselmann, K., D. B. Ross, P. Muller, and W. Sell, "A parametric wave prediction model," J. Phys. Oceanogr., 6, 200-228, 1976.

Hasselmann, D. E., M. Dunckel, and J. A. Ewing, "Directional wave spectra observed during JONSWAP 1973," J. Phys. Oceanogr., 10, 1264-1280, 1980.

Headrick, R. H. and James F. Lynch, "Acoustic normal mode fluctuation statistics in the 1995 SWARM internal wave scattering experiment," J. Acoust. Soc. Am., V107, 01-220, 2000.

Heitsenrether , R. M., and M. Badiey, "Modeling acoustic signal fluctuations induced by sea surface roughness," AIP Conference Proceedings, V 728, Issue 1, 214-221, 2004.

Holloway, P., "A comparison of semidiurnal internal tides from different bathymetric locations on the Australian North West Shelf," J. of Phys. Oceanog., 15, 240-251, 1984.

Hsu, M.-K., A. K. Liu, and C. Liu, "A study of internal waves in the China Seas and Yellow Sea using SAR," Cont. Shelf Res., 20, 389-410, 2000.

Ingenito, Frank, "Measurements of Mode Attenuation Coefficients in Shallow Water," J. Acoust. Soc. Am., V53, 858-863, 1973.

Ivakin, A. N., and Yu P. Lysanov, "Backscattering of sound from an inhomogeneous bottom at small grazing angles," Sov. Phys. Acoust., V31, 236-237, 1985.

Jensen, Finn B., William A. Kuperman, Michael B. Porter, Henrik Schmidt, *Computational Ocean Acoustics*, Springer-Verlag, NY, 2000.

Jobst, W. and X. Zabalgogeazcoa, "Coherence Estimates for Signals Propagated Through Acoustic Channels with Multiple Paths," J. Acoust. Soc. Am., V65, 622-630, 1979.

Kang, S. K., M. G. Foreman, H.-J. Lie, J. H. Lee, J. Cherniawsky, and K.-D. Yum, "Two layer tidal modeling of the Yellow and East China Seas with application to seasonal variability of the M_2 tide," J. Geophys. Res, 107, 3020, 2002.

Katsnelson, Boris G. and Valery G. Petnikov, *Shallow-Water Acoustics*, Springer-Verlag, NY, 2001.

Katsnelson, Boris G., S. A. Pereselkov, V. G. Petnikov, K. D. Sabinin, and A. N. Serebryanyi, "Acoustic Effects Caused by High-Intensity Internal Waves in a Shelf Zone," Acoust. Phys., V 47(4), 424-429, 2001.

Kinney, W. A., and C. S. Clay, "The Spatial Coherence of Sound Scattered from a Wind-Driven Surface: Comparison Between Experiment, Eckart Theory, and the Facet-Ensemble Method," J. Acoust. Soc. Am., V75, 145-148, 1984.

Koch, R. A., C. Penland, P. J. Vidmar, and K. E. Hawker, "On the calculation of normal mode group velocity and attenuation," J. Acoust. Soc. Am., V73, 820-825, 1983.

Kuperman, W. A., and F. Ingenito, "Attenuation of the Coherent Component of Sound Propagating in Shallow Water with Rough Boundaries," J. Acoust. Soc. Am., V61, 1178-1187, 1977.

Kuperman, William A., Finn B. Jensen, Editors of *Bottom-Interacting Ocean Acoustics*, NATO SACLANT ASW, Plenum Press, NY, 1980.

Kuperman, William A. and James F. Lynch, "Shallow-Water Acoustics," Physics Today, V57(10), 55-61, 2004.

Kur'yanov, B. F., "The scattering of sound at a rough surface with two types of irregularity," Sov. Phys. Acoust., V8, 252-257, 1963.

Lynch, J. R., G. Jin, R. Pawlowicz, D. Ray, C.-S. Chiu, J. H. Miller, R. H. Bourke, A. R. Parsons, J. Plueddemann, and R. Muench, "Acoustic travel time perturbations due to shallow water internal waves and internal tides in the Barents Sea Polar Front: Theory and experiment," J. Acoust. Soc. Am., vol. 99, 803-821, 1996.

Marsh, H. W., "Sound reflection and scattering from the sea surface," J. Acoust. Soc. Am., V35, 240-244, 1963.

Martin, J. J., "Sea-surface roughness and acoustic reverberation- an operational model," J. Acoust. Soc. Am., V40, 697-710, 1966.

Martin, J. S., W. R. Scott Jr., G. D. Larson, P. H. Rogers, and G. S. McCall II, "Probing signal Design for seismic landmine detection," Proc. of SPIE, V5415, pp.133-144, 2004.

Masson, D., "Observations of the response of sea wavs to veering winds," J. Phys. Oceanogr., 20, 1876-1885, 1990.

McDaniel, Suzanne T., "Mode conversion in shallow water propagation," J. Acoust. Soc. Am., V62, 320-325, 1977.

McDaniel, Suzanne T., "Mode coupling due to interaction with the seabed," J. Acoust. Soc. Am., V72, 916-923, 1982.

McDaniel, Suzanne T. and A. D. Gorman, "Acoustic and radar sea-surface backscatter," J. Geophys. Res., V87, 4127-4136, 1982.

McDaniel, Suzanne T. and A. D. Gorman, "An examination of the composite-roughness scattering model," J. Acoust. Soc. Am., V73, 1476-1486, 1983.

Meecham, W. C., "On the use of the Kirchhoff approximation for the solution of reflection problems," J. Rational Mech. Anal. V5, 323-333, 1956.

Miller, James H., Louis R. Bartek, Gopu R. Potty, Dajun Tang, Jungyul Na, and Yiquan Qi, "Sediments in the East China Sea," IEEE J. Oceanic Eng., V29, No.4, 940-951, 2004.

Mitsuyasu, H., F. Tasai, T. Suhara, S. Mizuno, M. Onkusu, T. Honda, and K. Rukiski, "Observations of the power spectrum of waves using a cloverleaf buoy," J. Phys. Oceanogr., 10, 286, 296, 1980.

Norton, G. V., J. C. Novarini, and R. S. Keiffer, "Coupling scattering from the sea surface to a one-way marching propagation model via conformal mapping: validation," J. Acoust. Soc. Am., V97, 2173-2180, 1995.

Norton, Guy V., Jorge C. Novarini, "The effect of sea-surface roughness on shallow water waveguide propagation: A coherent approach," J. Acoust. Soc. Am., V99, 2013-2021, 1996.

Oba, Roger and Steven Finette, "Acoustic Propagation Through Anisotropic Internal Wave Fields: Transmission Loss, Cross-Range Coherence, and Horizontal Refraction," J. Acoust. Soc. Am., V111, 769-784, 2002.

Ostashev, V. E., G. Goedecke, John M. Noble, "Effects of Wind Velocity Fluctuations on the Statistical Moments of Plane and Spherical Sound Waves in the Turbulent Atmosphere with the Gaussian Correlation Function of Wind Velocity Functions," J. Acoust. Soc. Am., V99, 2488, 1996.

Pekeris, C. L., "Theory of Propagation of Explosive Sound in Shallow Water," Geol., Soc. Am. Mem. 27, 1948.

Perrone, Anthony J., "Ambient-noise-spectrum levels as a function of water depth," J. Acoust. Soc. Am., V48, 362-370, 1970.

Pierson, W. J., and L. Moskowitz, "A proposed spectral form for fully developed wind seas based on the similarity theory of S. A. Kitaigorodskii," J. Geophys. Res., 69, 5181-5190, 1964.

Phillips, O. M., "The equilibrium range in the spectrum of wind-generated waves," J. Fluid Mech., 4, 426-434, 1958.

Prinsenberg, S. J., W. L. Wilmot, and M. Rattray, Jr., "Generation and dissipation of coastal internal tides," Deep Sea Res., 21,263-281, 1974.

Rattray, M., Jr., J. Dworski, and P.Kovala, "Generation of long internal waves at the continental slope," Deep Sea Res., 16, 179-195, 1969.

Rosenberg, A. P., "A new rough surface parabolic equation program for computing low-frequency acoustic forward scattering from the coean surface," J. Acoust. Soc. Am., V105, 144-153, 1999.

Rouseff, D., and T. E. Ewart, "Effect of random sea surface and bottom roughness on propagation in shallow water," J. Acoust. Soc. Am., V98, 3397-3404, 1995.

Rouseff, D., A. Turgut, S. N. Wolf, S. Finette, M. H. Orr, B. H. Pasewark, J. R. Apel, M. Badiey, C.-S. Chiu, R. H. Headrick, J. F. Lynch, J. N. Kemp, A. E. Newhall, and D. Tielbürger, "Coherence of Acoustic Modes propagating Through Shallow Water Internal Waves," J. Acoust. Soc. Am., V111, 1655-1666, 2002.

Rubenstein, D., "Observations of cnoidal internal waves and their effect on acoustic propagation in shallow water," IEEE J. Oceanic Eng., 24(3), 346-357, 1999.

Sazontov, Alexander. G., Alexander L. Matveyev, and Nadezhdak Vdovicheva, "Acoustic Coherence in Shallow Water: Theory and Observation," IEEE, Journal of Oceanic Engineering, V27, 653-663, 2002.

Selfridge, A. R., "Approximate material properties in isotropic materials," IEEE Trans. Sonics and Ultrasonics, V SU-32, 381-394, 1985.

Smith, S. D., R. J. Anderson, W. A. Oost, C. Kraan, N. Maat, J. DeCosmo, K. B. Katsaros, K. L. Davidson, K. Bumke, L. Hasse, and H. M. Chadwick, "Sea surface wind stress and drag coefficients: The HEXOS results," Boundary-Layer Meteool., 60, 109-142, 1992.

Smith, P. W. Jr., "The Averaged Impulse Response of a Shallow-Water Channel," J. Acoust. Soc. Am., V50, 332-336, 1971.

Smith, P. W. Jr., "Spatial Coherence in Multipath or Multimodal Channels," J. Acoust. Soc. Am., V60, 1976, 305-310.

Stoll, Robert D., and G. M. Bryan, "Wave Attenuation in Saturated Sediments," J. Acoust. Soc. Am., V47, 1440-1447, 1970.

Stoll, Robert D., "Expreimental Studies of Attenuation in Sediments," J. Acoust. Soc. Am., V66, 1152-1160, 1979.

Stoll, Robert D., "Theoretical Aspects of Sound Transmission in Sediments," J. Acoust. Soc. Am., V68, 1341-1350, 1980.

Stoll, Robert D., "Marine Sediment Acoustics," J. Acoust. Soc. Am., V77, 1789-1799, 1985.

Stoll, Robert D., George M. Bryan, and Edgar O. Bautista, "Measuring Lateral Variability of Sediment Geoacoustic Properties," J. Acoust. Soc. Am., V96, 427-438, 1994.

Tang, X., and F. D. Tappert, "Effects of internal waves on sound pulse propagation in the Straits of Florida," IEEE J. Oceanic Eng., V22, 245-255, 1997.

Tappert, F. D., "The parabolic approximation method" in *Wave Propagation in Underwater Acoustics*, edited by J. B. Keller and J. S. Papadakis, Springer-Verlag, NewYork, 1977.

Thorpe, S. A., "The Excitation, Dissipation, and Interaction of Internal Waves in the Deep Ocean," J. Geoph. Res., V80(3), 328-338, 1975.

Tielbürger, Dirk, Steven Finette, and Stephen Wolf, "Acoustic Propagation Through an Internal Wave Field in a Shallow Water Waveguide," J. Acoust. Soc. Am., V101, 789-808, 1997.

Tindle, C. T., H. Hobaek, and T. G. Muir, "Measurements of the Frequency Dependence of Normal Mode," J. Acoust. Soc. Am., V64, 1178-1185, 1978.

Tindle, C. T., H. Hobaek, and T. G. Muir, "Downslope Propagation of Normal Modes in a Shallow Water Wedge," J. Acoust. Soc. Am., V81, 275-286, 1987.

Tindle, C. T., H. Hobaek, and T. G. Muir, "Normal Mode Filtering for Downslope Propagation in a Shallow Water Wedge," J. Acoust. Soc. Am., V81, 286-294, 1987.

Thorsos, E. I., "Acoustic scattering from a "Pierson-Moskowitz" sea surface," J. Acoust. Soc. Am., V88, 335-349, 1990.

Toba, Y., "Local balance in the air-sea boundary process," J. Oceanogr. Soc. Japan, 29, 209-220, 1973.

Tolstoy, I., and C. S. Clay, *Ocean Acoustics*, McGraw_Hill, NY, 1966.

Traykovski, Peter, "Travel-time perturbations due to internal waves: equivalence of modal and ray solutions," J. Acoust. Soc. Am., V99, 822-830, 1996.

Urick, Robert J., *Principles of Underwater Sound for Engineers*, McGraw-Hill, NY, 1967.

Urick, Robert J., G. R. Lund. "Vertical Coherence of Shall-Water Reverberation," J. Acoust. Soc. Am., V47, 342-349, 1970.

Urick, Robert J., "Measurements of the Vertical Coherence of the Sound from a Near-Surface Source in the Sea and the Effect on the Gain of an Additive Vertical Array," J. Acoust. Soc. Am., V54, 115-120, 1973.

Vdovicheva, N. K., A. L. Matveev, and A. G. Sazontov, "Experimental and theoretical Study of the Vertical Coherence of the Sound Field in a Shallow Water," Acoustical Physics, V48, 263-267, 2002.

Wang, Qin, and Renhe Zhang, "Sound Spatial Correlations in Shallow Water," J. Acoust. Soc. Am., V92, 932-938, 1992.

Wang, Yun-yu, Jixun Zhou, H. Li, Z. Zhang, S. Jiang, and S. E. Chang, "Model Experimental Studies on Spatial Filtering of Normal Modes," Chin. Phys., Vol.2, 515-528, 1982.

Weston, David E. and Pamela A. Ching, "Wind effects in shallow-water acoustic transmission," J. Acoust. Soc. Am., V86, 1530-1545, 1989.

Wille, P., and R. Thiele, "Transverse Horizontal Coherence of Explosive Signals in Shallow Water," J. Acoust. Soc. Am., V50, 348-353, 1971.

Yamamoto, Tokuo and Altan Turgut, "Acoustic Wave Propagation Through Porous Media with Arbitrary Pore Size Distributions," J. Acoust. Soc. Am., V83, 1744-1751, 1988.

Yang, Jie, Ji-Xun Zhou, and Peter H. Rogers, "Effect of wind-generated surface waves on vertical coherence of sound propagation in the East China Sea," J. Acoust. Soc. Am. 119, 3346, 2006.

Yang, Jie, Ji-Xun Zhou, and Peter H. Rogers, "Data-model comparisons for sea surface waves from the ASIAEX East China Sea Experiment," submitted.

Yang, Jie[1], Xue-Zhen Zhang, Ji-Xun Zhou, and Peter H. Rogers, "Vertical coherence of sound propagation and seabed geoacoustic inversion," J. Acoust. Soc. Am. 115, 2408, 2004.

Yang, Jie[2], Shihong Zhou, Ji-Xun Zhou, and James F. Lynch, "Internal Wave Characteristics at the ASIAEX Site in the East China Sea," IEEE J. Oceanic Eng., V29, No.4, 1054-1060, 2004.

Yang, Jie and Peter H. Rogers, "Influence of internal waves on vertical coherence of sound propagation in the East China Sea," J. Acoust. Soc. Am. V117, 2548, 2005.

Yang, T. C., and Kwang Yoo, "Internal Wave Spectrum in Shallow Water: Measurement and Comparison with the Garret-Munk Model," IEEE J. Oceanic Eng., V24(3), 333-345,1999.

Young, I. R., S. Hasselmann, and K. Hasselmann, "Computations of the response of a wave spectrum to a sudden change in the wind direction," J. Phys. Oceanogr., 17, 1317-1338, 1987.

Young, I. R., *Wind Generated Ocean Waves*, Elsevier Ocean Engineering Book Series, Vol. 2, 1999.

Zhang, R. H. and G. L. Jin, "Normal-mode theory of the average reverberation intensity in shallow water," J. Sound Vib., V119, 215-223, 1987.

Zhou, Ji-Xun, "Vertical Coherence of the Sound Field and Boundary Losses in Shallow Water," Cinese Physics, 494-504, 1981.

Zhou, Ji-Xun, "Normal mode measurements and remote sensing of sea-bottom sound velocity and attenuation in shallow water," J. Acoust. Soc. Am., V78, 1003-1009, 1985.

Zhou, Ji-Xun, Xue-Zhen Zhang, and Peter H. Rogers, "Effect of Frequency Dependence of Sea-Bottom Attenuation on the Optimum Frequency for Acoustic Propagation in Shallow Water," J. Acoust. Soc. Am., V82, 1987, 287-292.

Zhou, Ji-Xun, Xue-Zhen Zhang, Peter H. Rogers, and Jacek Jarzynski, "Geoacoustic parameters in a stratified sea bottom from shallow-water acoustic propagation," J. Acoust. Soc. Am., V82, 2068-2074, 1987.

Zhou, Ji-Xun, Xue-Zhen Zhang, and Peter H. Rogers, "Resonant interaction of sound wave with internal solitons in the coastal zone," J. Acoust. Soc. Am., V90, 2042-2054, 1991.

Zhou, Ji-Xun, Xue-Zhen Zhang, Peter H. Dahl, and Jeffrey A. Simmen, "Sea surface effects on reverberation vertical coherence and inverted bottom acoustic parameters in the East China Sea," J. Acoust. Soc. Am., V115, 2550, 2004.

J.-X. Zhou, X.-Z. Zhang, P. H. Rogers, J. A. Simmen, P. H. Dahl, G. Jin, and Z. Peng, "Reverberation vertical coherence and sea-bottom geoacoustic inversion in shallow water," IEEE J. Oceanic Eng., V29, 988-999, 2004.

Zhou, Ji-Xun and Xue-Zhen Zhang "Nonlinear frequency dependence of the effective seabottom acoustic attenuation from low-frequency field measurements in shallow water," J. Acoust. Soc. Am., V117, 2494, 2005.

J.-X. Zhou, X.-Z. Zhang, Z. Peng, and J. S. Martin, "Sea surface effect on shallow-water reverberation," IEEE J. Oceanic Eng., V121, 98-107, 2007.

VITA

JIE YANG

Jie Yang was born in Nanjing, China. She received a B.S. in Physics from Ocean University of China, Qingdao, China in 1999. She then started graduate studies in Physics at Texas A&M University, College Station, Texas in the same year before transferring to Georgia Tech to pursue a doctorate degree in Mechanical Engineering in spring, 2001. Her current research interests include ocean acoustics and acoustical oceanography, particularly sound propagation in shallow-water waveguide influenced by environmental parameters, acoustic modeling, and signal processing.